SYNTHESIS, CHARACTERIZATION AND CO_2 ADSORPTION PERFORMANCE ANALYSIS OF MgO FUNCTIONALIZED ACTIVATED CARBON FROM PALM KERNEL SHELL

JAYAPRINA GOPALAN

FACULTY OF ENGINEERING
UNIVERSITI MALAYA
KUALA LUMPUR

2024

SYNTHESIS, CHARACTERIZATION AND CO_2 ADSORPTION PERFORMANCE ANALYSIS OF MgO FUNCTIONALIZED ACTIVATED CARBON FROM PALM KERNEL SHELL

JAYAPRINA GOPALAN

THESIS SUBMITTED IN FULFILMENT OF THE REQUIREMENTS FOR THE DEGREE OF MASTER OF ENGINEERING SCIENCE

FACULTY OF ENGINEERING
UNIVERSITI MALAYA
KUALA LUMPUR

2024

UNIVERSITI MALAYA

ORIGINAL LITERARY WORK DECLARATION

Name of Candidate: **Jayaprina Gopalan**

Matric No: **S2005490**

Name of Degree**: Master of Engineering Science**

Title of Project Paper/Research Report/Dissertation/Thesis ("this Work"):

Synthesis, Characterization and CO_2 Adsorption Performance Analysis of MgO Functionalized Activated Carbon from Palm Kernel Shell.

Field of Study: **Advanced Materials & Technology (NEC 524: Chemical Process)**

I do solemnly and sincerely declare that:

(1) I am the sole author/writer of this Work;
(2) This Work is original;
(3) Any use of any work in which copyright exists was done by way of fair dealing and for permitted purposes and any excerpt or extract from, or reference to or reproduction of any copyright work has been disclosed expressly and sufficiently and the title of the Work and its authorship have been acknowledged in this Work;
(4) I do not have any actual knowledge nor do I ought reasonably to know that the making of this work constitutes an infringement of any copyright work;
(5) I hereby assign all and every rights in the copyright to this Work to the Universiti Malaya ("UM"), who henceforth shall be owner of the copyright in this Work and that any reproduction or use in any form or by any means whatsoever is prohibited without the written consent of UM having been first had and obtained;
(6) I am fully aware that if in the course of making this Work I have infringed any copyright whether intentionally or otherwise, I may be subject to legal action or any other action as may be determined by UM.

Candidate's Signature Date: 8/4/2024

Subscribed and solemnly declared before,

Witness's Signature Date: 8/4/2024

Name:

Designation:

SYNTHESIS, CHARACTERIZATION AND CO_2 ADSORPTION PERFORMANCE ANALYSIS OF MgO FUNCTIONALIZED ACTIVATED CARBON FROM PALM KERNEL SHELL

ABSTRACT

In recent years, there has been a growing interest in solid adsorbents derived from biomass for CO_2 adsorption due to their carbonaceous properties which allow for modifications to enhance selectivity towards CO_2 in flue gas. Therefore, this study aimed to use innovative and sustainable approach to develop activated carbon (AC) for CO_2 adsorption using palm kernel shells (PKS) as the precursor. The PKS were subjected to pyrolysis, and then activated with potassium hydroxide to enhance the porosity and surface area of the material. The properties of raw PKS adsorbents were further modified using magnesium oxide (MgO) to enhance the adsorption capacity, selectivity, and the potential for regeneration. The physicochemical analysis shows that the chemical activation has increased the surface area of the AC where the PKS-AC had a surface area of 1086 m^2/g which was significantly higher compared to PKS-Char (435 m^2/g) and PKS-AC-MgO (418 m^2/g). Although the binding of MgO in PKS-AC-MgO led to a decrease in the surface area affected by pore blockages, this material demonstrated the most significant micropore volume (0.29 cm^2/g) and pore diameter (2.8 nm) compared to raw PKS. The functional group analysis confirmed the impregnation of MgO in PKS-AC, as the transmittance band at 861 cm^{-1} and 617 cm^{-1} were assigned to metal oxygen bonding of Mg-O. Additionally, thermogravimetric analysis showed that all the PKS-adsorbent have a good thermal and mechanical stability at higher temperatures, up to 500°C.

The CO_2 adsorption performance analysis revealed that PKS-AC-MgO has highest adsorption capacity of 155.35 mg/g at the lowest temperature of 25°C and 5 bars, compared to PKS-AC (149.63 mg/g) and PKS-Char (138.19 mg/g). On the other hand,

PKS-AC-MgO also shows enhanced performance at 50°C with 117. 5 mg/g of adsorption capacity. Similarly, at a higher temperature of 75°C, the PKS-AC-MgO adsorbent also achieved 92.4 mg/g of adsorption capacity which is 48 % higher than the PKS-AC. This suggested the greater synergistic effect between the PKS-AC and MgO at elevated temperatures. Isotherm analysis indicated the presence of both physisorption and chemisorption of CO_2 for all the PKS- adsorbents developed in this study. Langmuir model was best fitted for PKS-AC-MgO with R^2 of 0.9916, which described the reaction due to restriction to monolayer formation. Thermodynamic studies showed a negative value of Gibbs free energy, enthalpy, and entropy indicating that the adsorption process of PKS-AC-MgO was spontaneous and favorable at 25°C. The economic analysis showed also shows that PKS-AC-MgO had a specific cost of $1,977 per tonne, which was 20% less than commercial AC.

In summary, this study reveals the effectiveness of a novel approach in CO_2 adsorption by utilizing AC impregnated with magnesium oxide developed from palm kernel shells.

Keywords: Carbon Dioxide, Adsorption, Biomass, Palm Kernel Shell, Metal Oxide.

SINTESIS, PENCIRIAN DAN ANALISIS PRESTASI PENJERAPAN CO_2 BAGI KARBON AKTIF YANG DIUBAHSUAI DENGAN MgO DAN KULIT BIJI KELAPA SAWIT

ABSTRAK

Sejak kebelakangan in, terdapat minat yang semakin meningkat terhadap penjerap pepejal yang diperbuat daripada biojisim untuk penjerapan CO_2 disebabkan oleh sifar karbonaceous yang membolehkan pengubahsuaian untuk meningkatkan selektiviti terhadap CO_2 dalam gas bahan api. Oleh itu, kajian ini bertujuan untuk menggunakan pendekatan inovatif dan lestari untuk membangunkan carbon teraktif untuk penjerapan CO_2 dengan menggunakan kulit biji kelapa sawit sebagai bahan asas. Kulit biji kelapa sawit telah mengalami piroliisis, dan kemudian diaktifkan dengan hidroksida kalium untuk meningkatkan porositi dan luas permukaan bahan. Sifat-sifat penjerap berasaskan kulit biji kelapa sawit telah diubah suai lebih lanjut dengan menggunakan magnesium oksida (MgO) untuk meningkatkan kapasiti penjerapan, kebolehpilihan, dan potensi untuk regenerasi. Analisis fizikokimia menunjukkan bahawa pengaktifan kimia telah meningkatkan porositi di mana kawasan permukaan untuk PKS-AC adalah 1086 m^2/g, yang jauh lebih tinggi berbanding PKS-Char (435 m^2/g) dan PKS-AC-MgO (418 m^2/g). Walaupun pengikatan MgO dalam PKS-AC-MgO menyebabkan pengurangan kawasan permukaan akibat sumbatan liang, bahan ini menunjukkan jumlah liang mikro yang paling signifikan (0.29 cm^2/g) dan diameter liang (2.8 nm), yang menguntungkan bagi penjerapan CO_2. Analisis kumpulan fungsional mengesahkan pengimpregnasian MgO dalam PKS-AC-MgO, di mana jalur transmitan pada 861 cm^{-1} dan 617 cm^{-1} diperuntukkan untuk pengikatan oksigen logam Mg-O. Analisis termogravimetrik bagi semua penjerap menunjukkan kestabilan termal dan mekanikal yang baik pada suhu yang lebih tinggi, sehingga 500°C.

Analisis prestasi penjerapan CO_2 mendedahkan bahawa PKS-AC-MgO mempunyai kapasiti penjerapan tertinggi sebanyak 155.35 mg/g pada suhu terendah 25°C dan 5 bar, berbanding PKS-AC (149.63 mg/g) dan PKS-Char (138.19 mg/g). Sebaliknya, PKS-AC-MgO juga menunjukkan prestasi yang ditingkatkan pada 50°C dengan kapasiti penjerapan sebanyak 117.5 mg/g. Demikian juga, pada suhu yang lebih tinggi, iaitu 75°C, pengadsorben PKS-AC-MgO mencapai kapasiti penjerapan sebanyak 92.4 mg/g yang mana 48% lebih tinggi daripada PKS-AC. Ini menunjukkan kesan sinergistik yang lebih besar antara PKS-AC dan MgO pada suhu yang lebih tinggi. Analisis isoterm menunjukkan kehadiran kedua-dua penjerapan fisik dan penjerapan kimia CO_2 untuk semua pengadsor berdasarkan PKS yang dibangunkan dalam kajian ini. Model Langmuir paling sesuai untuk PKS-AC-MgO dengan R^2 sebanyak 0.9916, yang menjelaskan tindak balas disebabkan oleh sekatan pembentukan lapisan tunggal. Kajian termodinamik menunjukkan nilai negatif bagi tenaga bebas Gibbs, entalpi, dan entropi, menunjukkan bahawa proses penjerapan PKS-AC-MgO adalah spontan dan menguntungkan pada 25°C. Analisis ekonomi juga menunjukkan bahawa PKS-AC-MgO mempunyai kos spesifik sebanyak $1,977 setiap tan, yang merupakan 20% kurang daripada karbon teraktif komersial.

Ringkasnya, kajian ini mendedahkan keberkesanan pendekatan baru dalam penjerapan CO_2 dengan menggunakan karbon teraktif yang diimpregnasi dengan magnesium oksida yang dibangunkan daripada kulit biji kelapa sawit.

Kata Kunci: Karbon Dioksida, Penjerapan, Sisa Bio, Biji Kelapa Sawit, Oksida Logam.

ACKNOWLEDGEMENTS

I would like to express my deepest gratitude to my beloved husband Devamuthan, for his unwavering support and constant presence throughout this journey. Your love, encouragement, and understanding have been my guiding light, and I am truly blessed to have you by my side.

To my esteemed supervisors, Professor Ir. Dr. Abdul Aziz and ChM. Dr. Archina Buthiyappan, I am deeply grateful for your guidance, expertise, and resourcefulness. Your valuable insights, constructive feedback, and mentorship have shaped this thesis into its final form. I would like to also thank lecturers from University Teknologi Petronas Dr. Surianti and Dr. Adilla, for all the supports.

My sincere appreciation goes to the Fundamental Research Grant Scheme (FRGS) – FP141-2019A, for financially supporting this research work. I would like to acknowledge all the lab assistance from Department of Chemical Engineering for assisting me during my experiment in the laboratory. To my dear friends and family, thank you for being my pillars of strength and for providing the much-needed mental and emotional support throughout this journey. Lastly, I would like to express my deepest appreciation to all those who have played a role, no matter how big or small, in this journey. Your support has been invaluable, and I am forever grateful for your presence in my life.

TABLE OF CONTENTS

LIST OF FIGURES

LIST OF TABLES

LIST OF SYMBOLS AND ABBREVIATIONS

CCD	:	Central Composite Design
CCUS	:	Carbon Capture Utilization and Storage
CO_2	:	Carbon Dioxide
F-value	:	Fisher's Value
RSM	:	Response Surface Methodology
FTIR	:	Fourier Transform Infrared Spectroscopy
SEM	:	Scanning Electron Microscopy
EDX	:	Energy Dispersive X-Ray
XRD	:	X-Ray Diffraction
RSM	:	Response Surface Methodology
ANOVA	:	Analysis Of Variance
HPVA	:	High Pressure Volumetric Analyzer
AC	:	Activated Carbon
BAC	:	Biomass-based Activated Carbon
MBAC	:	Metal Impregnated BAC
PKS	:	Palm Kernel Shell
PKS-Char	:	Palm Kernel Shell Biochar
PKS-AC	:	Palm Kernel Shell KOH Activated Carbon
PKS-AC-MgO	:	Palm Kernel Shell KOH Activated Carbon MgO Impregnated

LIST OF APPENDICES

CHAPTER 1: INTRODUCTION

1.1 Background

The increasing level of CO_2 in the atmosphere due to various industrial activities causes adverse impacts on the terrestrial climate, shifts in global warming, rising sea levels, ocean acidification, ice melting which resulted severe droughts and several other significant health effects (Ahmed et al., 2019). With the existing industrial activities, the CO_2 emission is expected to rise up to 282-701 Giga tones between the year of 2010 and 2060 (Ahmed et al., 2019). Hence, in addition to implementing environmentally friendly practices in industries, it is essential to capture the CO_2 emissions, thereby mitigating their impact on the ecosystem. As a result, extensive research has been undertaken in the past years to explore CO_2 capture techniques, with the adsorption process emerging as a highly effective and efficient method. This preference is attributed to its various process advantages, including low investment costs, operational parameter flexibility, a broad selection of adsorbent options, reduced energy intensity, and the generation of harmless by-products(S. Liu et al., 2017).

Various solid adsorbents, including commercial AC, zeolite, silica, and graphene oxide, had been extensively utilized in CO_2 adsorption (Abuelnoor, AlHajaj, Khaleel, Vega, & Abu-Zahra, 2021). Despite their wide application, solid adsorbents encounter limitations beyond cost considerations such as reduced adsorption capacity, diminished surface area, and porosity, reliance on energy-intensive production methods, and dependence on non-renewable resources (Creamer, Gao, & Wang, 2016). Consequently, the search for cost-effective and high-capacity CO_2 adsorbents has spurred research focus towards the development of biomass-based adsorbents derived from renewable resources.

Recently, biomass such as rice husk, coconut shell, rubber seeds, sludge and saw dusts have been used to synthesize adsorbent for CO_2 capture (C. Liu et al., 2023). However, raw biomass adsorbent has some limitations such as low thermal stability, slow adsorption and desorption kinetics, low surface area and macro porous structure (Al Mesfer, 2020). Therefore, raw biomass adsorbent can be subjected to chemical activation at high temperature to promote the formation of meso-micropores and increases the specific surface area which could enhances the CO_2 adsorption (Goel, Mohan, & Dinesha, 2021). Modification of biomass-based adsorbent with basic (alkaline) functional group such as earth metal oxides is proven to further enhance its affinity for acidic CO_2 molecules via Lewis's base and acidic interaction (Creamer, Gao, Zimmerman, & Harris, 2018). The combination of chemically activated biomass-based adsorbent with basic functional group has a lot of potential for acidic CO_2 adsorption, however studies related to are largely lacking in the literature and mainly focused on its applicability in other application such as pollutant removal from waste water. There are very less studies related to the formation of different structure and morphologies after chemical activation and earth metal oxide functionalization, and the adsorbent interaction mechanism in CO_2 adsorption.

Therefore, in this study palm kernel shell (PKS) which is known as one of the Southeast Asia's prominent renewable biomass energy sources has been used as a feedstock for the development of adsorbent (Sabri, Rani, Mohamad, Mohd Muhsen, & Md Zaini, 2023). PKS offers numerous benefits, including a high calorific value, low sulphur and ash content and excellent availability throughout the year (Promraksa & Rakmak, 2020). To further enhance the adsorption capabilities of PKS, potassium hydroxide (KOH) has been used as a chemical activating agent as it can results in adsorbent with high surface area, promotes the development of micro-meso pores, yield high percentage of biochar and it is also a cost-effective activating agent (Asadi-

Sangachini, Galangash, Younesi, & Nowrouzi, 2019). Additionally, magnesium oxide (MgO), an earth metal oxide was used to functionalized with PKS-adsorbent due to their effective CO_2 adsorption properties, offering Mg^{+2} and O^{-2} active sites for both physical and chemical CO_2 adsorption (Chammingkwan, Mai, Ikeda, & Mohan, 2021). It should be noted, for the first time, MgO functionalized, KOH activated PKS-adsorbent is synthesized to analyze the physicochemical properties and the CO_2 adsorption capacity at the practical industrial CO_2 emission condition.

Hence, this study aimed to utilized PKS to synthesize three types of PKS-AC via slow pyrolysis and a two-step synthesis using alkaline activation and magnesium oxide (MgO) impregnation. A comprehensive evaluation has been conducted on the physiochemical characterization and the CO_2 adsorption capacity was evaluated using a High-Pressure Volumetric Analyzer (HPVA). Adsorption isotherm and thermodynamics analysis were conducted to gain insights into the adsorption phenomena and efficiency of the adsorbent (Andirova, Lei, Zhao, & Choi, 2015). This research lays the foundation for developing biomass-based solid adsorbent for CO_2 capture in fossil fuel-fired power plants, with implications for a more sustainable and environmentally friendly approach to mitigate CO_2 emissions.

1.2 Problem Statement

Biomass-based materials have gained attention as potential alternatives to commercial solid adsorbents for CO_2 capture due to several advantages such as renewable resources, abundant feedstocks, low environmental impacts, potential for valorization and bio-degradability. While biomass-based activated carbon (BAC) has many advantages, it also faces certain limitations that need to be addressed to make it more effective and practical. Research and development efforts are ongoing to address these limitations by modifying the surface chemistry and combining alkali earth metal oxide that can offer synergistic

benefits such as enhance stability, selectivity, and adsorption kinetics. This study aimed to enhance biomass's applicability as AC while addressing the global CO_2 challenge through functionalization to achieve optimized CO_2 adsorption, paving the way for future CO_2 adsorption technologies with valuable products.

1.3 Research Question

The following research questions are specifically sought to be addressed:

1. How does the surface area and porosity of AC derived from palm kernel shells change with different modification techniques?
2. How does alkaline activation and magnesium oxide impregnation affect CO_2 adsorption?
3. How does the modified AC 's CO_2 adsorption performance impact the isotherm and thermodynamic aspects of CO_2 adsorption onto the palm kernel shell-based AC?
4. How does the PKS-adsorbent improve the techno-economic and environmental feasibility compared to commercial AC?

1.4 Aim and Objective of the Study

The aim of this study is to develop PKS-adsorbent for enhanced CO_2 adsorption. The specific objectives of the study are to:

1. Synthesize and characterize the AC derived from palm kernel shells, which is subsequently activated with potassium hydroxide (KOH) and impregnated with magnesium oxide (MgO)
2. Identify the CO_2 adsorption performance of the PKS-adsorbents (PKS-Char, PKS-AC and PKS-AC-MgO) at different operational parameters.
3. Determine the mechanism and thermodynamic properties of CO_2 adsorption onto palm kernel shells (PKS) based adsorbents.

4. Evaluate the techno-economic and environment feasibility of the PKS-adsorbents

1.5 Scope of the Study

The scope of the study is to synthesize three types of PKS-adsorbent via slow pyrolysis, KOH alkaline activation and MgO earth metal oxide impregnation for enhanced CO_2 adsorption under varying temperature (25℃, 50℃ and 75℃) and pressure (1 bar to 5 bar) using a high-pressure volumetric analyzer (HPVA). Comprehensive characterization analysis has been carried out to study the physicochemical properties of the adsorbents. The CO_2 adsorption study was optimized using Central Composite Design by varying the temperature and pressure. Moreover, the fundamental mechanisms of CO_2 adsorption isotherms and thermodynamics contributed to the development of sustainable and effective novel adsorbent for mitigating CO_2 emissions has been evaluated. The CO_2 desorption and regeneration study were conducted. Techno-economic and environmental feasibility assessment has been carried out.

1.6 Significance and Novelty of the Study

The functionalization of biomass-based AC for CO_2 adsorption offers a sustainable approach to capture CO_2. With rising concerns about climate change and increasing levels of CO_2 in the atmosphere, this study can contribute to mitigate the effects of greenhouse gas emissions and combat global warming. Moreover, biomass is a renewable resource, and its utilization as AC presents an eco-friendly alternative to commercial AC derived from fossil fuels or other non-renewable sources. This helps to reduce the reliance on non-sustainable resources and contributes to a greener and more sustainable future. The study can explore the potential use of biomass waste materials, such as agricultural residues as a precursor for AC. This practice promotes waste valorization and reduces the burden on landfills, simultaneously addressing waste management challenges and contributing to circular economy principles.

Additionally, functionalization techniques can enhance the adsorption properties of AC. By modifying the surface properties, such as introducing specific functional groups or nanostructures, the ability to adsorb CO_2 can be optimized. Finally, as the world continues to face the challenges of climate change, effective CO_2 capture technologies become crucial in meeting emission reduction targets. This study aligns with global efforts to combat climate change and contributes to a sustainable and low-carbon future. In summary, the study on the functionalization of earth metal oxide on biomass AC opens avenues for further research and innovation in the field of carbon capture and adsorption technologies. It encourages scientists and engineers to explore new techniques and materials, leading to continuous improvements in the field.

1.7 Thesis Outline

In this study, PKS was utilized to synthesize adsorbents using KOH activation and MgO modification. The experimental methodology and result obtained are presented comprehensively and significantly. This dissertation is divided into 5 Chapters.

Chapter 1: Introduction:

Chapter 1 offers a comprehensive introduction to the topic, encompassing an overview of CO_2 capture and its significance in mitigating climate change. It also provides an overview of adsorption as a promising technique for CO_2 capture. The chapter discusses the drawbacks of the adsorption process and emphasizes the importance of developing a sustainable, highly stable, and cost-effective adsorbent for CO_2 adsorption from the agricultural sectors in Malaysia. The justification for choosing the adsorption process and palm kernel shells with alkaline activation and MgO impregnation, based on the literature study, is also briefly discussed. Furthermore, the chapter defines the problem statement, research questions, aims, objectives, scope, and significance of the study. The thesis outline is also included within this chapter.

Chapter 2: Literature Review:

This chapter establishes the literature review, extensively covering topics such as CO_2 emissions, their environmental impacts, the CO_2 adsorption process, commercially available solid adsorbents, agricultural waste, biomass-based adsorbents for CO_2 capture, diverse methods for synthesizing PKS-adsorbent, activation and functionalization techniques, and the CO_2 adsorption mechanism. Furthermore, this section also delves into critical factors affecting CO_2 adsorption, including textural properties, surface chemistry, and the stability of the adsorbent. The justification for selecting the specific adsorbent is also provided in this section. Lastly, the chapter discusses the influence of operational parameters on the adsorption process.

Chapter 3: Methodology:

This chapter provides an overview of the research methodology employed in the study. It outlines the characteristics of the newly developed PKS-adsorbent and presents the CO_2 adsorption experimental procedures using High Pressure Volumetric Analyzer. Additionally, the chapter offers comprehensive information on the adsorption isotherms, thermodynamics, and the implementation of response surface methodology, a statistical approach utilized in this study, which is also briefly explained.

Chapter 4: Result and Discussion:

Chapter 4 contains the results and discussion on the analysis of characterization of PKS-adsorbent. Hence, the results and discussion on the CO_2 adsorption efficiency on the PKS-adsorbent and the effects of the operating parameters were also described. The adsorption isotherm, thermodynamic studies and the regenerability of adsorbent was also presented in this chapter. In addition, the comparison between developed PKS-adsorbent with

various biomass and commercial adsorbent also presented in this chapter. Additionally, the chapter presents an economic analysis and addresses the environmental implications.

Chapter 5: Conclusion:

In this chapter, the conclusion based on the findings and future recommendation are also presented for future study in the field.

CHAPTER 2: LITERATURE REVIEW

2.1 Introduction

This section consists of detail explanation on topics related to the study beginning with the current issue with CO_2 emission and available capture technologies. The limitation of these technologies was further discussed followed by the advantages of adsorption over these technologies. The biomass based adsorbent development, synthesis procedures with activation technique are also discussed in this chapter.

2.2 Carbon Dioxide Emission and Capture Technologies

CO_2 is a naturally occurring acidic gas in the air at 0.04 ppm where it is a greenhouse gas that traps heat in the atmosphere to keeps the earth warm (Rattanaphan, Rungrotmongkol, & Kongsune, 2020). Aside from that, CO_2 is essential for the carbon cycle, photosynthesis and respiration. Although CO_2 is essential, the anthropogenic activities have increased CO_2 levels above the safe limit of 350 ppm, causing negative effects on the planet (Rouzitalab, Maklavany, Jafarinejad, & Rashidi, 2020). In the year of December 2021, the level of CO_2 has touched 416.71 ppm and studies showed that from 2010 to 2020, nearly 80% of CO_2 emissions are a result from human activities towards globalization such as open burning, fossil fuel burning, energy generating industries and so on (Ahmed et al., 2019). The inability of the carbon cycle to balance the huge amount of CO_2 resulted in a variety of serious environmental and health consequences such as global warming, ocean acidification and respiratory diseases in human (Maciá-Agulló, Moore, Cazorla-Amorós, & Linares-Solano, 2004). In order to mitigate the severe effects of CO_2, researchers are actively working to develop advanced technologies focused on CO_2 separation from large-scale industries, which are the primary source of CO_2 emissions.

Many new policies have been implemented to promote cleaner production in the process industries such as (1) finding a replacement (renewable energy) for fossil fuel consumption in energy generation; (2) implementing strategies, regulations, and policies to reduce CO_2 emissions through industries; and also (3) carbon capture, utilization and storage (CCUS). Carbon Capture technologies consist of three main processes such as pre-combustion, post-combustion, and oxy-fuel combustion (Al Mesfer, 2020). Pre-combustion is performed on the fuel, often coal or natural gas before it is burned which into syngas (Bisinella, Hulgaard, Riber, Damgaard, & Christensen, 2021). Pre-combustion also contributes to impurities in the gas stream, and this process has a lower affinity towards adsorbents by producing gaseous such as carbon monoxide (CO) and methane (CH_4) (Younas et al., 2020). On the other hand, this gas contributes to the greenhouse effect, requires a higher operational temperature, high investment and maintenance costs which make it a difficult choice (Al-Rowaili et al., 2021). Furthermore, in oxyfuel combustion, fossil fuels are burned in pure oxygen, resulting in a concentrated CO_2 stream that could be captured more easily (Danish, Parthasarthy, & Al Mesfer, 2021). But the requirement for a significant amount of electric power to separate oxygen from air results in a high capital cost requirement. Whereas in the post-combustion capture, CO_2 is separated from flue gases after burning fossil fuels, often using solvents or solid adsorbents and this makes the post-combustion technologies optimal to be upgraded in the existing power plant facilities (Luo et al., 2022).

Table 2.1 discusses the advantages and limitations of CO_2 capturing techniques. Post-combustion CO_2 capture is the simplest method among others, and it could be easily adapted to the current CCS infrastructure (K. Ho, Jin, Zhong, Vu, & Lee, 2017). On the other hand, this process is also remains the only solution capable of significantly reducing emissions from current significant stationary sources, such as power plants and other

major industrial plants such as cement, mining, textiles, quarrying and wood industries (Raganati, Miccio, & Ammendola, 2021). Additionally, it is also one of the most cost-effective which does not require to shut down the plant for maintenance, and it is readily managed or regulated and environmentally favorable.

Multiple separation technologies such as membranes separation, cryogenics separation, absorption and adsorption are available for CO_2 post-combustion capture as stated in Table 2.2 (Ji et al., 2020). The advantages and limitations of these technologies in capturing CO_2 are summarized in the Table 2.2. Membrane separation uses polymer or ceramic-based material membranes to filter out CO_2 gas at elevated pressure, allowing successful CO_2 permeation for CO_2/H_2 and CO_2/N_2 selectivity in the flue gas (Alfe, Policicchio, Lisi, & Gargiulo, 2021). Membrane separation is suitable for separating CO_2 from gas mixtures with low to moderate CO_2 concentration and this process is environmentally friendly, with minimal or no chemical usage. However, this process is limited by the membrane selectivity and permeability, which could affect separation efficiency (Gan et al., 2021). This process also requires multiple stages or complex configurations for high-purity CO_2 capture which is prone to fouling and degradation over time, affecting performance (Ji et al., 2020).

Cryogenic CO_2 separation, on the other hand, is based on the assumption that each gas in the flue gas has a liquid state temperature and pressure gradient (Ahmed et al., 2019). In his technique CO_2 can be separated from gas mixtures by cooling them to very low temperatures, causing CO_2 to condense into a liquid while other gases remain gaseous. Although this process is highly efficient for large-scale CO_2 capture and high-purity applications, there are still challenges such as high energy-intensive due to the need for very low temperatures, requires significant capital investment for cryogenic equipment and it can be complex to operate and maintain (Chao Chen, Kim, Yang, &

Ahn, 2011). On the other hand, absorption process is a process where amine-based chemicals are often utilized to capture CO_2 from a gas stream. The solvent reacts with CO_2 to form a solution, which can then be processed to release the captured CO_2 which appears to be the most common method for treating massive amounts of CO_2 emissions from burning (Grande, Kvamsdal, Mondino, & Blom, 2017). Though absorption is a common approach, it has a number of limitations, including a significant amount of energy required for solvent regeneration, use of hot absorbents involve safety and environmental concerns, materials erosion, high corrosion and high energy intensity (Lee et al., 2020).

Adsorption on the other hand, is a promising alternative for CO_2 separation processes due to high selectivity, requiring lower energy input compared to methods like cryogenic separation, often simpler to operate and require less complex equipment, easy to scaled up or down to accommodate different flow rates and capacities, environmentally friendly, using natural or benign adsorbents without the need for harmful chemicals, flexible and generate minimal emissions and pollutants, contributing to cleaner and more environmentally conscious operations (H. Liu, Liang, Wang, Ma, & Chen, 2021). Adsorbents are materials used to capture and hold specific substances from gas or liquid mixtures through the process of adsorption. There are two type of solid adsorbent present which are carbonaceous and non-carbonaceous adsorbent (Figure 2.1) such as AC, zeolites, molecular sieves, and more. Among the solid adsorbent materials, AC is highly porous carbonaceous materials with a large surface area. They are versatile and widely used in applications such as CO_2 capture, environmental remediation, catalysis, energy storage and conversion. Biomass-derived porous carbonaceous AC are found to be quite attractive to be used for CO_2 capture largely due to their enhanced textural properties, relatively simple and facile synthesis methods, high CO_2 adsorption capacities and most

importantly, the inexpensive and renewable nature of biomass that could reduce the overall cost of the CO_2 capture process which is also help to manage the waste and mitigate environmental issues wisely (Q. Liu et al., 2013).

Table 2.1: Comparison of CO_2 capture technologies (Q. Wang, Luo, Zhong, & Borgna, 2011; Y. Zhao et al., 2021)

Capture Technologies	Area of Application	Advantages	Disadvantages
Pre-Combustion	Coal-gasification plants	• High CO_2 concentration increases sorption efficiency • Technology is completely developed and commercially deployed at the needed scale in some industrial sectors • Retrofitting of existing plants is possible.	• Temperature-related heat transfer difficulty • efficiency degradation difficulties linked with the usage of hydrogen-rich gas turbine fuel • Elevated parasitic power demand for adsorbent regeneration. • Insufficient experience owing to only limited number of gasification facilities already in operation • Expensive capital and operational expenses for existing adsorption systems.
Post-Combustion	Coal-fired and gas-fired plants	• The technology is more developed than other techniques. • Can be simply integrated into existing facilities.	• Low CO_2 concentration negatively impacts capture efficiency
Oxy-Fuel Combustion	Coal-gasification plants	• Very high CO_2 content, which improves absorption efficiency	• High decline in efficiency and energy penalty • Manufacture of cryogenic CO_2 is expensive

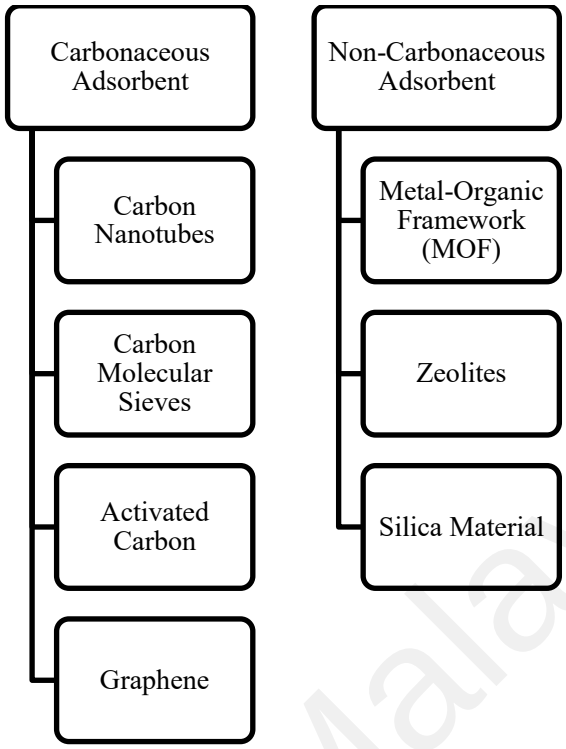

Figure 2.1: Physical Solid Adsorbents (Carbonaceous/ Non-Carbonaceous Adsorbents) for CO_2 Adsorption.

2.3 Biomass Based Activated Carbon for CO_2 Adsorption

Table 2.3 shows the comparison of the conventional solid adsorbents such as zeolite, metal-organic framework (MOF), silica and AC. Zeolites are microporous crystalline minerals comprised of silicon, aluminium, and oxygen. Zeolite has great stability and surface area but in context of CO_2 adsorption, zeolite has poor selectivity towards CO_2 and required high pressure (> 10 bar) and temperature (> 400℃) for the regeneration purposes. Similarly, although MOF is greatly being used in adsorption process, the cost of MOF is one of the major limitations which make it less desirable for CO_2 adsorption process. Silica gel is also great adsorbent which can be ideal for waste water treatment but for CO_2 adsorption, it has limitation at regeneration process where it requires greater temperature and pressure for regeneration. Although the limitation associated with the

solid adsorbents can be solved using different approaches, researchers are actively finding alternative for solid adsorbent which can be beneficial for both environmentally and economically (Y. Wu et al., 2020).

Biomass-based AC, utilizes renewable sources like agricultural waste, reducing dependence on fossil fuels and waste generation. Its production often has a lower carbon footprint and aligns with circular economy principles by repurposing biomass waste (Abuelnoor et al., 2021). Percentage of carbon content such as cellulose, hemicellulose and lignin are the important criterion to select the biomass for any pollutant removal process as these are the main component in the BAC which will contribute to the porous structure (Gayathiri, Pulingam, Lee, & Sudesh, 2022). As seen in Table 2.4, most of the studies have chosen wood type biomass as it contains almost 50 % carbon (Yargicoglu, Sadasivam, Reddy, & Spokas, 2015). Similarly, the BAC produced from wood biomass exhibited greater yield of BAC with higher surface area and porosity (Ahmed et al., 2019; Nowrouzi, Younesi, & Bahramifar, 2017). Furthermore, the by-products of fruits processing industry such as seed, branches, peel which contain large amounts of carbon can be used for the production of BAC. For an instance, fruit peel from pineapple, durian, grape and banana had been used in the production of CO_2 adsorbent (Y. L. Tan, Hameed, & Abdullah, 2020) (Otieno et al., 2021) (G.-g. Huang, Liu, Wu, & Cai, 2019).

Cellulose is the most abundant lignocellulosic component in biomass, followed by hemicelluloses and lignin. Cellulose comprises 40–50% by weight of dry biomass meanwhile, hemicellulose comprises in between 25-35% by weight. Lignin is placed between the outer layers of fibers, giving structural rigidity to the biomass (Mishra, kumar, Kumar, & Mohanty, 2022).

Table 2.2: Advantages and limitations of CO_2 separation technologies (González, Plaza, Rubiera, & Pevida, 2013)

Separation technology	Advantages	Limitations
Membrane	• Regeneration process is not required • Energy efficient during separation • Low-cost operation • This process has been used for the separation of other gaseous	• Fouling of membrane • Low selectivity of materials for membrane • Limited to certain operating parameter
Absorption	• Suitable for retrofitting existing power plants • Provide high absorption efficiency more than 90%. • Sorbents can be regenerated	• Poor gas-liquid contact surface • CO_2 loading is poor • Solvent escape • Corrosivity rate is high • High energy/cost for regeneration • Absorption efficiency depends on CO_2 concentration
Cryogenic	• Chemicals are not required • Matured technology • Has been used in CO_2 recovery for many years	• High investment • Need for the removal of trace components to prevent the clogging • Only adaptable for high concentration of CO_2 >90% • High energy intensive • Process carried out at low temperature.
Adsorption	• Solid adsorbent • High adsorption efficiency more than 85% • Wide range of adsorbents can be used in this process • Low temperature and pressure for regeneration • User friendly • Process is reversible	• Low CO_2 selectivity • Require high temperature adsorbent • High energy required for desorption • High number of cycles for TSA process. • Unstable pressure occurrence in PSA/VSA

According to the literature, the maize stover has 51.2% cellulose, 30.7% hemicellulose, and 14.4% lignin, for a total carbon value of 49.3% (Zong et al., 2021). Similarly, the carbon content of Jatropha wood is 42.2%, with 48% cellulose, 25% hemicellulose, and 25% of lignin (Abuelnoor et al., 2021). Typically, cellulose and hemicellulose are the first volatiles to be removed during carbonization and activation (200 ℃) while lignin at higher temperature of 800 ℃ (Cho, Cho, Song, & Kwon, 2015). Several lignocellulosic biomasses have special features that make them appropriate for manufacturing BAC in easy and cost-effective ways. The energy required for activation, on the other hand, is completely determined by the features of the biomass waste, such as its structure and chemical behavior of all of its constituents (Kantarli & Yanik, 2010). It is critical to select the appropriate biomass waste for the production of BAC while also converting agricultural waste into value-added goods (Sevilla & Fuertes, 2011).

Agricultural biomass sources in Malaysia can exceed 70 million tons per year, with palm oil accounting for 94% of the biomass resulting it to be an excellent source of ACs (Singh et al., 2019). Oil palm kernel shell is a by-product of fruit bunches processing that is commonly referred to as palm kernel shell (PKS) which has a complex pore structure and fiber matrix (Nasri, Hamza, Ismail, Ahmed, & Mohsin, 2014). These are Southeast Asia's most appealing renewable energy sources and the abundance of these biomass resources is increasing as Malaysia, Indonesia, and Thailand develop their palm oil industries. Due to Malaysia's position as the world's second largest producer of crude palm oil, the palm oil industry is the 4th biggest contributor to the country's gross national income (GNI), accounting for approximately 8% of GDP and nearly RM 50 billion in GNI (Shabbani, Khairunnisa Shamsudin, Dezaini, Abd, & Othman, 2022). As a result, this produces the most biomass, estimated at 80 million dry tons per year, with substantial commercial viability. PKS have low moisture content between 11% and 13% in

comparison to other biomass residues (Maciá-Agulló et al., 2004; Nasri et al., 2014). Moreover, in comparison to other industrial residues, it is a high-quality biomass fuel with a consistent size distribution, easy handling, and low biological activity.

Table 2.3: Advantages and limitations of conventional solid adsorbents used for CO_2 adsorption (Abuelnoor et al., 2021; Karimi, Shirzad, Silva, & Rodrigues, 2022)

Adsorbent type	Advantages	Limitations
Zeolite	• Good stability (mechanical/thermal/ cyclic regeneration) • Greater surface area	• Low selectivity towards CO_2 • Not ideal for adsorption • High temperature or pressure required for regeneration • Expensive
MOFs	• Greater surface area • Good stability (physiochemical properties can be adjusted)	• Low selectivity towards CO_2 • Not ideal for adsorption • High temperature or pressure required for regeneration • Expensive • Difficult regeneration process
Silica	• Greater surface area • Good stability (physiochemical properties can be adjusted)(Yan et al., 2018)	• High temperature or pressure required for regeneration
AC	• Low-cost • Wide availability • High stability	• Performance is hindered high pressure gas • Low sensitive to vapour and impurities

Table 2.4: Summary of surface area and pore size of biomass based activated carbons from published works

Biomass	Surface Area (m^2 / g)	Pore Size (cm^3 / g)	Ref
Pine Wood	982	0.53	(Ahmed et al., 2019)
Rice straw	413	0.61	(P. H. Ho, Lofty, Basta, & Trens, 2021)
Rice Husks	317	0.50	
Bagasse	655	0.25	
Local date fruits seed	422	0.15	(Ogungbenro, Quang, Al-Ali, Vega, & Abu-Zahra, 2020)
Slash pine (scientific name Pinus elliottii) wood	1,081	0.37	(Ahmed et al., 2019)
Sunflowers stem.	3,072	0.46	(Sun, Yang, & Li, 2019)
Cork dust waste	2,380	0.70	(X. Zhang, Elsayed, Song, Shmulsky, & Hassan, 2020)
Pomegranate peels	585–1,593	0.20 to 0.54	(Serafin, Narkiewicz, Morawski, Wróbel, & Michalkiewicz, 2017)
Woody biomass	1,081	0.37	(Ahmed et al., 2019)
Brazilian nutshell and Cascara Capuassau	1630	<0.7	(Serafin, Ouzzine, Cruz Junior, & Sreńscek-Nazzal, 2021)
Pineapple peels	11	0.00	(Otieno et al., 2021)
Durian Shell	8	0.01	(Y. L. Tan et al., 2020)
Grape Waste	6	0.01	(Sayğılı, Güzel, & Önal, 2015)
Pecan Shell	331	0.17	(Aguayo-Villarreal, Bonilla-Petriciolet, & Muñiz-Valencia, 2017)
Douglas fir sawdust pellets	-	-	(Yadavalli et al., 2017)
Horse manure bio waste	698	0.30	(Mong et al., 2020)
Raw Rice Husk	190	-	(Shukla, Sahoo, & Remya, 2019)
Mushroom Roots	1,024	0.89	(Cheng et al., 2016)
Walnut Shell	418	0.35	(Duan, Zhang, Srinivasakannan, & Wang, 2017)
Persian Ironwood biomass	1,935	-	(Nowrouzi et al., 2017)
Garlic peel	262	0.70	(G.-g. Huang et al., 2019)
Waste Entada Rheedii shell (ERS)	488	0.19	(Mallesh et al., 2020)
Taihu blue algae biomass	1,018	0.46	(H. Wang, Wang, Liu, & Yan, 2021)

Table 2.5: Composition of biomass wastes used for production of activated carbon

Biomass	Proximate analysis				Ultimate analysis				Lignocellulose composition			Ref
	Moisture	Volatile	Ash	Fixed Carbon	Carbon	Hydrogen	Oxygen	Nitrogen	Cellulose	Hemicellulose	Lignin	
Jackfruit Leaves	-	63.2	19.3	18.5	37.5	4.9	37.8	0.7	34.7	4.7	19.7	(Nayak, Bhushan, Gupta, & Kotnala, 2021)
Tamarind Seed	4.1	68.2	1.7	26.5	46.6	5.6	42.8	2.9	20.9	15.7	28.7	(Sruthi, Ashok, Monica Nissy, Koteshwara rao, & Vangalapati, 2019)
Mango Leaves	-	67.2	10.1	23.1	44.7	5.7	38.8	0.6	40.6	11.5	28.5	(Lin & Zheng, 2021)
Avacado Seed	35.1	72.4	0.9	26	42.7	5.6	43.4	0.5	40.9	3.3	15.8	(Zong et al., 2021)
Pineapple Skin	9.13	84.8	3.9	2.0	44.7	6.8	47.2	0.7	20.4	9.4	41.2	(Otieno et al., 2021)
Banana Peel	11.5	88.0	9.2	2.7	35.6	6.1	45.9	1.9	9.9	41.2	8.9	(Selimin et al., 2021)
Corn Cob	9.7	80.6	2.8	18.2	43.6	5.8	48.6	0.7	40.3	28.7	35.1	(Zong et al., 2021)
Maize	11.1	78.9	2.1	19.0	40.9	6.9	50.7	1.1	-	-	-	(Hu et al., 2021)
Palm Kernel Shell	12.6	75.1	2.8	22.0	51.5	6.3	41.3	0.7	33.0	23.8	45.5	(Nasri et al., 2014)
Wheat Straw	5.5	68.2	17.0	14.7	37.2	5.5	37.3	1.1	57.0	16.1	19.1	(Hu et al., 2021)

2.4 Activated Carbon Synthesis Methods

Other than selecting the optimum raw material for BAC, equal importance has to be given to the production method for the synthesis of BAC. Therefore, in this section we will discuss on the type of carbonization method available for the production of biochar from biomass and the activation techniques.

2.4.1 Carbonization of Biomass

There are two types of biomass carbonization techniques commonly used for CO_2 adsorption application; hydrothermal carbonization (HTC) and direct carbonization (calcination and pyrolysis). HTC is a thermochemical treatment that involves hydrolysis, dehydration, decarboxylation, condensation, and aromatization processes (Goel et al., 2021). Biochar that is produced from the HTC method is known as hydrochar, using a HTC reactor heated at an elevated temperature (F. Huang et al., 2021).

Direct carbonization consists of two type of process: calcination and pyrolysis. Calcination is the process of heating a feedstock to a high temperature in the presence of oxygen in order to remove volatile material from biomass and transform it into biochar (Fodah, Ghosal, & Behera, 2021). Meanwhile, pyrolysis is one of the most prevalent, straightforward, and well-liked methods for converting biomass residue into biochar adsorbent using the direct heat method, where the source of heat comes from the heating element embedded in the furnace. Pyrolysis takes place in inert conditions with the absence of oxygen (Ghodake et al., 2021). During this process, the main components of biomass, which are cellulose, hemicellulose, and lignin, will undergo breakdown at different ranges of temperature where cellulose at 200-400 ℃ and lignin at high temperature of 800 ℃ (A. H. Ruhaimi, Aziz, & Jalil, 2021). The by-product of this process usually yields AC, bio-oil, and syngas (J. Liu et al., 2020). According to studies,

cellulose undergo breakdown at 240 ºC to 350 ºC, hemicellulose will degrade at 200 ºC to 260 ºC and lignin degradation usually occurs at temperature range 280 ºC to 500 ºC due to a multiplex structure (Zheng, Lee, Lin, & Samannan, 2020). Oxygen is removed during the carbonization process by holding the process at an inert condition to avoid oxidation and the formation of light gases such as oxygen and water which might turn the biomass into ash (Mong et al., 2020). According to Jjagwe (2012) there are four stages involved in the thermal degradation of biomass where the (1) is to extract the moisture from the biomass at temperatures less than 200 °C; (2) degradation of biomass through the elimination of volatile components at temperatures of 170 °C to 270 °C; (3) Decomposition is continued at temperatures varying from 270 °C to 350 °C towards the AC; and finally (4) elimination of volatile components and formation of carbonaceous material at temperatures greater than 350 °C (Jjagwe, Olupot, Menya, & Kalibbala, 2021).

Table 2.6 compares the various carbonization methods for biochar from biomass. Carbonization can greatly impact the yield and quality of biochar. The most notable distinction between pyrolysis and HTC is that oxygen is absent during pyrolysis, where it is replaced by inert gases such as nitrogen to prevent the formation of ash during the carbonization and open up pores of the BAC resulting in greater active sites (Jagodzińska, Zaini, Svanberg, Yang, & Jönsson, 2021). Parameters such as temperature, contact time, and pressure are varied among these two processes, resulting in different dominant products of biochar, bio-oil, and biogas or syngas for each process (Mong et al., 2020). The study of Qin and Wang (2020) found that the longer the contact time, the lower the biochar output (Qin et al., 2020). Similarly, the study of Promraksa (2021) was conducted over a narrower range of contact time, identified the heating rate had an impact on the surface area and properties of the biochar (Promraksa & Rakmak, 2020). Carbonization

typically used to reduce the water and volatile component content of biomass while enhancing their calorific value, resulting in higher-quality BAC. In the study of Handayani (2019) briquettes were subjected to a carbonization duration of 30, 60, 90, 120, and 150 minutes and determined that 150 minutes was the optimal carbonization period for biomass used in the production of bio-coal briquettes with the moisture content of 10.2%, an ash content of 12.9%, a volatile substance content of 31.9%, a fixed carbon content of 45.0%, and a calorific value of 5,897 Cal/g (Handayani, Ningsih, & Meriansyah, 2019). These results were in line with the hypothesis that the longer the carbonization period, the lower the moisture content, by allowing more pores to open up and permit the moisture and volatile components to escape from biomass (Fodah et al., 2021).

There are two types of pyrolysis, which are slow and fast pyrolysis. They differ in terms of heating rate and contact time, as stated in Table 2.6. The slow pyrolysis process is carried out at a lower temperature of carbonization and longer contact time (Kwak et al., 2019). Slow pyrolysis produces promising biochar yields for biomass with higher lignin content, higher ash content, and larger particle size (Fodah et al., 2021). In contrast, the fast pyrolysis is carried out at a high temperature with a short contact time. As both these processes come with some drawbacks, vacuum pyrolysis and microwave pyrolysis have been developed and widely used (Su et al., 2020). These newly developed processes have been proven to have no substantial impact on the biochar yield and was more viable compared to furnace heating (Chunxiang Chen et al., 2021). Microwave assisted pyrolysis (MAP) has advantages over slow and fast pyrolysis as it uses internal heating with less energy loss and the processing time (Zheng et al., 2020). Additionally, the biochar produced via MAP has more uniform chemical structure. This method has been employed to produce biochar from P. juliflora biomass, which demonstrated that the

biochar had greater surface area and pore volume than the raw biomass at 357 m^2/g (Qin et al., 2020). This result shows that compared to the fast and slow pyrolysis methods, MAP is more efficient and produces quality biochar with greater surface area and pore volume.

Slow pyrolysis is often preferred over HTC, fast pyrolysis, and microwave-assisted pyrolysis due to several advantages such as producing a relatively higher yield of solid biochar with well-developed pore structures and surface areas, making it more suitable for adsorption applications. Slow pyrolysis allows for better control over the thermal decomposition process, leading to more controlled and consistent product properties (Q. Gao et al., 2022). Moreover, the prolonged pyrolysis time in slow pyrolysis minimizes the degradation of biochar, leading to more stable and durable adsorbent (Cho et al., 2015; Duran-Jimenez et al., 2021; Fodah et al., 2021; L. Gao et al., 2021). Slow pyrolysis typically requires less energy compared to rapid processes like fast pyrolysis or microwave-assisted pyrolysis and it produces less bio-oil, which can be advantageous to obtain solid biochar for adsorption rather than liquid products (Ghodake et al., 2021).

Table 2.6: Comparison of operating condition of carbonization process

Aspects	Hydrothermal Carbonization	Direct Carbonization			
		Calcination	Pyrolysis		
			Slow-Pyrolysis	Fast-Pyrolysis	MAP
Heating rate	• 180°C -260°C	• Involve air with presence of oxygen	• 0.02°C /s to 1 °C /s	• 2°C /s or above	• Internal heating • (0.915 to 24.124 GHz)
Operating temperature	• 300°C - 1200°C depends on desired products	• Above 500°C	• 300°C -700°C	• 300°C - 1000°C	• No specific/ difficult to control
Residence time	• 1-16 hr	• No specific	• Few hours to days	• Short, below 10s, 0.5-20s	• Short
Consumption of time	• High	• No specific	• High	• Short	• Short
energy efficiency	• Less energy input	• Release toxic elements	• Low	• High temperature	• High heat transfer efficiency
Application /Advantages	• High energy density of biochar	• Combustion of biomass sources	• Vacuum pyrolysis, microwave	• For bio-oil production	• Uniform chemical

2.4.2 Functionalization of Biomass-based Activated Carbon

Biomass-based adsorbent undergoes chemical or physical activation, in order to develop its textural properties to enhance the adsorption capacity. Activation is important to eliminate substances that block the pores, to yield more elementary carbon crystals of AC, as well as to oxidize the carbon particles (Ahmed et al., 2019). The commonly used methods can be classified into two main groups: physical and chemical modifications. These two methods are often influenced by the type of chemical activator used during the production, impregnation time, carbonization temperature and duration, chemical composition of the raw material and various other factors (G.-g. Huang et al., 2019).

There are a few types of physical activation, such as CO_2 activation and steam activation, where the steam acts as an oxidizing agent (Machado et al., 2020). CO_2 is often chosen for physical activation due to the stability of the gas (Pallarés, González-Cencerrado, & Arauzo, 2018). Numerous investigations have established that CO_2 activated BA promotes the development of microspores (Dissanayake et al., 2020). CO_2 combines with the carbon in BA to make carbon monoxide, and this process can be called hot corrosion, which results in a more microporous structure. (W.-H. Huang, Lee, & Huang, 2021). According to studies, the CO_2 adsorption capacity in CO_2-modified AC was much greater compared to unmodified BAC (Yin et al., 2021) and steam modified BA (Ma, Ying, Cao, Wang, & Ai, 2020). Compared to CO_2 activation, steam activation yields a lower amount of BA as the process elevates temperatures and the water molecules degrade rapidly (Bazan-Wozniak, Nowicki, & Pietrzak, 2021). Steam activation is preferable for materials such as shells, which have a high density, whereas CO_2 activation is preferable for materials with a fiber structure and a low density, such as straws and husks (Pallarés et al., 2018). Physical activation, on the contrary, produces BAs with a specific surface area of lower than 2000 m^2/g (Kim, Seo, Kwak, Cho, & Im, 2021).

According to the study of Zhang (2013) corncob activated with steam generated AC had a greater surface area and improved pore formation than corncob activated with CO_2. Different biomass wastes require different activating agents to produce high-quality AC for use as an adsorbent (C. Zhang et al., 2013), In summary, physical activation is preferable on an industrial scale because it enables greater control over micro porosity growth, which enables more precise pyrolysis stage optimization (Januszewicz, Kazimierski, Klein, Kardas, & Luczak, 2020). Additionally, BA generated through physical activation, does not necessitate chemical neutralization, which is critical for many applications as it reduces both process costs and pollution (Zabaniotou, Stavropoulos, & Skoulou, 2008). Physical activation has several advantages, including a cheap cost of manufacturing of BAs and it is able to sustain the shape and texture of the raw material, allowing for the manufacturing of BA from fabrics and cloths (Yek et al., 2020).

Chemical activating agent can be classified into two groups which are acid or alkali base reagent. The common acid activating agents including sulphuric acid (H_2SO_4), phosphoric acid (H_3PO_4), hydrochloric acid (HCl), zinc chloride ($ZnCl_2$), calcium chloride ($CaCl_2$), hydrogen fluoride (HF) while the alkaline activating agents are sodium hydroxide (NaOH) and potassium hydroxide (KOH) (Ogungbenro et al., 2020). The chemical activation onto AC can be performed using wet or dry method. The chemical compound is combined directly with the AC and followed by carbonization in dry activation, while in wet activation the chemical reagent is mixed with water and combined with AC with followed with stirring and heating. Additionally, the dry mixing of AC results in great adsorption effectiveness (Rehman et al., 2018) as it is not only simple to execute but also requires less energy and results in AC with larger surface areas (Bazan-Wozniak et al., 2021). Two type of chemical mixing (dry and wet) was performed on AC

and discovered the dry mixing enhanced surface area of BAC from 796 m^2/g to 932 m^2/g (Minani, Foppen, & Lens, 2014).

The excessive use of activating agent have possibility to reduce the specific surface area of AC due to the chemical reaction that degrades the pores as the excess activator expands the pores, causing more carbon to be burned off, which affects the CO_2 adsorption capability (Y. Gao, Yue, Gao, & Li, 2020). Generally, when biomass undergo carbonization, there will be a formation of pores and hydroxyl group, which will further undergo activation. During this activation process, the chemicals will diffuse into the biochar's internal structure, and expand the existing pore size resulting to a greater surface area of AC (Nowrouzi et al., 2017). Chemical activation also causes formation of other compound onto AC due to the various reaction that takes place depending on the operating parameter of the activation process such as temperature and pH. The study of Jjahwe (2021) found a reduction in surface area after undergoing acid activation, due to the formation of phosphate esters which lead to the blockage of active sides in AC (Jjagwe et al., 2021). A study conducted by Hidayu and Muda (2020), investigated similar $ZnCl_2$ ratio of 1:1 to activate coconut shells and palm kernel shells for 1 hour at an activation temperature of 550℃. The surface area of palm kernel AC was 1223 m^2/g, which was substantially greater than the surface area of coconut shell, which was 953 m^2/g (Hidayu & Muda, 2016). Similarly, Sun (2017) found comparable results when they investigated the effect of H_3PO_4 activation on Arundo Donax and Pomelo Peel under the identical settings. They discovered that Pomelo Peels produced AC with a high surface area of 1252 m^2/g, as contrast to Arundo, which only produced AC with a surface area of 675 m^2/g (Singh, Kim, Lakhi, Joseph, et al., 2017)

Chemical activation of adsorbents is preferred over physical activation due to its ability to create a wider range of pore sizes and tailored surface chemistry. Chemical

activation involves introducing activating agents during the activation process, which leads to the development of a diverse pore structure and enhanced surface area. This method allows for greater control over pore size distribution, resulting in improved adsorption capacity, selectivity, and efficiency. Additionally, chemical activation enables the introduction of specific functional groups on the adsorbent surface, enhancing its affinity for target substances. These advantages make chemical activation a more versatile and effective approach for optimizing adsorbent properties to suit a wide range of adsorption applications. BAC employed in CO_2 capture applications have shown promising results, thus much more study is being conducted in this field.

Table 2.7 shows the surface area and pore size of BAC prepared using various carbonization and activation and Table 2.8 summarizes BAC application in capturing CO_2. Potassium hydroxide is one of several activators, which also include H_3PO_4, $ZnCl_2$, H_2O, and others. KOH is particularly promising because of its low activation temperature, improved biochar yields, and highly developed microporous structure with an incredibly high specific surface area (reaching 3000 m^2/g). Serafin (2021) investigated KOH activation using three different biomass types (pomegranate peels, carrot peels, and fern leaves), while keeping other activation settings constant, the BAC prepared from fern leaves produced the best surface area, 1593 m^2/g, compared to 585 m^2/g for those prepared from pomegranate peels (Otieno et al., 2021). Similarly, activated corncob using $ZnCl_2$ for 0.5–4 hours, and the maximum surface area was 960 m^2/g (Yang et al., 2018). As a result, even if the same chemical activator was employed, parameters such as the impregnation ratio, type of raw material, and processing conditions during the carbonization stage, such as temperature and time, impact the surface area of the synthesized AC.

Table 2.7: Properties of biomass based activated carbon derived from biomass wastes.

Biomass	Synthesizing Method	Activation Method	Surface Area (m^2 / g)	Pore Size (cm^3 / g)	Ref.
Pine wood	Direct carbonization	KOH activation	982	0.53	(Ahmed et al., 2019)
Rice straw		HNO_3 activation	413	0.61	(P. H. Ho et al., 2021)
Rice husks		KOH activation	317	0.51	(Y. Wang, Jia, Chen, Fang, & Du, 2020)
Bagasse		Alkaline activation	655	0.26	(Machado et al., 2020)
Local date fruits seed		HNO_3 activation	422	0.16	(Ogungbenro et al., 2020)
Slash pine (scientific name Pinus elliottii) wood		Alkaline activation	1,081	0.37	(Ahmed et al., 2019)
Sunflowers stem.		Alkaline activation	3072	0.46	(Sun et al., 2019)
Cork dust waste		Acid activation	2380	0.70	(X. Zhang et al., 2020)
Pomegranate peels		KOH activation	585–1593	0.20 to 0.54	(Serafin et al., 2017)
Woody biomass		CO_2 activation	1,081	0.37	(Ahmed et al., 2019)
Brazilian nutshell and Cascara Capuassau		Alkaline activation	1630	<0.7	(Serafin et al., 2021)
Pineapple peels		Acid activation	11	0.01	(Otieno et al., 2021)
Durian shell		KOH activation	8	0.01	(Y. L. Tan et al., 2020)
Pecan shell		Alkaline activation	331	0.17	(Aguayo-Villarreal et al., 2017)
Douglas fir sawdust pellets		Acid activation	-	-	(Yadavalli et al., 2017)
Horse manure bio waste		Acid activation	698	0.30	(Mong et al., 2020)

Table 2.7 continued

Biomass	Synthesizing Method	Activation Method	Surface Area (m^2 / g)	Pore Size (cm^3 / g)	Ref.
Raw rice Husk	HTC	KOH activation	190	-	(Shukla et al., 2019)
Mushroom roots		Acid activation	1024	0.89	(Cheng et al., 2016)
Walnut shell		HNO_3 activation	418	0.35	(Duan et al., 2017)
Persian ironwood biomass		KOH activation	1935	-	(Nowrouzi et al., 2017)
Garlic peel		KOH activation	262	0.70	(G.-g. Huang et al., 2019)
Waste Entada Rheedii shell (ERS)		KOH activation	488	0.20	(Mallesh et al., 2020)
Taihu blue algae biomass		Alkaline activation	1018	0.46	(H. Wang et al., 2021)
Water chestnut shell		Acid activation	1517	0.61	(Q. Li et al., 2020)
Tobacco stalk		KOH activation	1313	<1	(F. Huang et al., 2021)
Garlic peel		HNO_3 activation	1 262	0.70	
Pine dust		CO_2 activation	2	0.02	(W. Li et al., 2021)
Tea stalk	HTC	KOH activation	666	0.36	(Başakçılardan Kabakcı & Baran, 2019)

Table 2.8: CO_2 Adsorption Capacity of Biomass Derived Activated Carbon

Biomass	Surface Area (m^2/g)	CO_2 Adsorption (mmol/g)	Ref
Pine cone	2110	4.7	(B. Zhu, Shang, & Guo, 2016)
Arundo donax	1122	3.6	(Singh, Kim, Lakhi, Srivastava, et al., 2017)
Coconut shell	1535	4.8	(Z. Zhao, Nie, & Zhou, 2019)
Coconut shell	1327	3.9	(Ello, de Souza, Trokourey, & Jaroniec, 2013a)
Black locust	2511	5.1	(Nelson et al., 2016)
Chestnut	747	2.3	(Parshetti, Chowdhury, & Balasubramanian, 2015)
Empty fruit bunch	2510	5.2	(D. Li, Tian, Li, Li, & Zhang, 2015)
Peanut shell	1713	7.3	(D. Li, Ma, Zhang, Tian, & Qiao, 2015)
Rice husk	2695	6.2	(D. Li, Ma, et al., 2015)
Crab shell	1196	4.3	(González et al., 2013)
Olive stones	1113	3.2	(González et al., 2013)
African palm shell	1890	6.3	(Ello, de Souza, Trokourey, & Jaroniec, 2013b)
Bamboo	1846	7.3	(Wei et al., 2012)
Celtuce leaves	3404	6.1	(Rutao Wang et al., 2012)
Cellulose	2370	5.8	(Sevilla & Fuertes, 2011)
Arundo donax	3298	2.2	(Singh, Kim, Lakhi, Joseph, et al., 2017; Singh, Lakhi, et al., 2017)
Arundo	1863	2.1	(Singh, Kim, Lakhi, Joseph, et al., 2017)
donax þ Chitosan	982	2.2	(M. G. Singh et al., 2018)
Arundo donax þ Urea	2232	3.2	(M. G. Singh et al., 2018) (G. Singh et al., 2018)
Arundo donax			(G. Singh et al., 2018)

2.5 Metal Impregnated Activated Carbon

Biomass-based activated carbon (BAC) offer numerous advantages, but they also come with certain limitations such as variability in biomass feedstock can vary in composition and properties, leading to inconsistent adsorption performance (W.-H. Huang et al., 2021). Since CO_2 is an acidic gas, other than physical and chemical activation some research has sought to add basic sites, especially basic metal oxide which has been proven to be an effective CO_2 adsorbent. Due to acid-base and redox properties, metal oxide is frequently employed as an independent adsorbent for the adsorption of CO_2 in the industrial applications but the usage of metal oxide alone for the adsorption of CO_2 has some limitation such as low surface area and stability (Abuelnoor et al., 2021). Therefore, impregnating metal oxide onto BAC able to increase the oxygen groups on the surface of BAC to serve as metal oxide loading sites by changing the basic characteristics of BAC for CO_2 adsorption (Adani et al., 2011). Metal oxide impregnated biomass-based activated carbon (MBAC) possesses great mechanical characteristic due to the size quantization effect especially towards CO_2 (J. Liu et al., 2020). As a result, impregnation on metal oxide onto BAC can result in a greater number of active sites for CO_2 adsorption, leading to more efficient application of metal oxides (Jung et al., 2021). Metal oxide also has the ability to physiosorbed and chemisorb CO_2 over a wide temperature range (473K-673K), and it required low energy for CO_2 regeneration (Ghosh, Sarathi, & Ramaprabhu, 2019).

Table 2.9, has summarized the BACs modification using metal oxide such as magnesium, aluminium, copper, iron, sodium and nickel. In the study of Guo (2015), investigated impregnation of different metal oxide onto Persian Ironwood based BAC and the trend of adsorption at 30°C was observed as, BAC-Cu (21.52 mmol/g)> BAC-Ni

(20.67 20 mmol/g)> BAC-CuNi (20.51 mmol/g)> BAC-Al/Mg (19.35 mmol/g)> BAC-Al (18.87 mmol/g)> BAC-Mg (18.85 mmol/g)>BAC (7mmol/g) (Y. Guo, Zhao, Chen, & Li, 2015). From this study it can be said that copper ion has high adsorption capacity compared to other BAC and Persian Ironwood without any metal impregnation possess the lowest CO_2 adsorption (Y. Guo et al., 2015). It can be noticed that impregnation of two type of metal oxide onto BAC, can further increase the CO_2 adsorption. For instance, the CaO/MgO-based BAC prepared using sol–gel method, presenting around 200 mg of CO_2/g of adsorbent.

Similarly, Mg based BAC for CO_2 adsorption with $Mg(NO_3)_2$ salt yielded 3.1 mmol/g CO_2 adsorption, and Mg-sugarcane based BAC used $MgCl_2$ salt achieved a CO_2 adsorption of 227-235 mg/g (Creamer et al., 2016). All this experiment has proven that addition of metal oxide onto BAC surely enhanced the CO_2 adsorption capacity compared to the raw or BAC. The presence of metal oxides such as Mg, Al, Cu, and Fe can potentially impact the BAC's capacity to adsorb CO_2 as it leads in the formation of more active sites which can attract the CO_2 molecules (Hongbo, Deng, Kommalapati, & Amarasekara, 2020). Even though the nature of BAC can be varied to be acidic, basic, or neutral it can undergo chemical transformation to become functionalized BAC. Metal oxide's addition to the surface of BAC increases the number of basic functional groups, hence enhancing the acidic CO_2 selectivity. Ca-based BAC generated at 700 ℃ exhibited the greatest CO_2 adsorption of 4.7 mmol/g at ambient condition compared to the raw AC (B. Zhu et al., 2016). The same study observed that BAC with no metal impregnation had lower CO2 adsorption compared to BAC with impregnation of Ca and Mg(B. Zhu et al., 2016). The excellent performance of these metal oxides materials in the oxygen reduction reaction (ORR) suggested that the BAC could be utilized in a variety of applications related to CO_2 capture processes (Al-Rowaili et al., 2021).

Literature shows that there are various metal modification methods can be adapted to impregnate the metal oxide on the surface of BAC and specifically, magnesium oxide (MgO) is a potential metal oxide choice for CO_2 capture applications due to its unique properties, such as possessing the appropriate surface basicity, which causes the formation of oxygen vacancies that impact CO_2 adsorption ability. In comparison to BAC based on Li and Ca, MgO has a significant advantage over other metal oxide adsorbents in that it requires a low regeneration temperature (773 K). Furthermore, MgO has a high theoretical adsorption of 24.8 mmol CO_2/g adsorbent, making it a promising adsorbent for CO_2 capture in the temperature range of 473-673 K. In essence, the adsorption process occurs when the adsorbent's basic O^{2-} - Mg^{2+} sites react with the acidic CO_2 gas to produce carbonate species such as bicarbonate, unidentate carbonate, and bidentate carbonate. As a result, MgO has a considerable potential to adsorb CO_2.

Table 2.9: Metal Impregnated Biomass Activated Carbon (MBAC)

Biomass	**Metal**	**Metal Modification Method**	**Ref.**
Tomato waste	Magnesium	Carbonize the biomass and metal particle together.	(Y. Yao et al., 2013)
Hickory chips (HC)	Iron		(Xiaoyun Xu et al., 2020)
BAC	Copper		
Cottonwood (CW) trees	Aluminium Magnesium		(Creamer et al., 2016)
	Iron oxide		
Graphene oxide	Titanium oxide/		(Chiang & Juang, 2017)
Rice husk	Lanthanum Cerium		(Y. Wang et al., 2020)
Coconut	Copper Cerium		(F. Li et al., 2010)
Fly ash	Alkali Metals	Wet impregnation using metal salt before carbonization	(Y. Guo et al., 2015)

Table 2.9 continued

Biomass	Metal	Metal Modification Method	Ref.
Walnut shell	Magnesium Aluminium Iron Nickel Calcium Sodium		(Lahijani, Mohammadi, & Mohamed, 2018)
MBAC	Copper		(Abdedayem, Guiza, & Ouederni, 2015)
MBAC	Chromium Iron		(Somy, Mehrnia, Amrei, Ghanizadeh, & Safari, 2009)
MBAC	Copper		(Hosseini et al., 2015)
MBAC	Nickel		
MBAC	Magnesium		
MBAC hickory chips (HC)	Iron		(Xiaoyun Xu et al., 2020)
Marine Microalgae	Magnesium		(Hou et al., 2021)
Corn stalk	Iron		(Zong et al., 2021)
Cow dung	Magnesium		(Q. Yao et al., 2021)
Wheat straw	Bismuth		(Hu et al., 2021)
Corn stalk	Iron		(B. Wang, Li, & Wang, 2019)
Pineapple waste	Lanthanum		(Liao et al., 2018)
Rice hull	Iron	Doping metal particles on BAC after carbonization	(S. Chen, Qi, Ma, & Zhao, 2020)
Bamboo Feedstock	Magnesium Aluminium		(R.-Z. Wang et al., 2020)

2.6 Critical Factors Influencing the Performance of Activated Carbon in CO_2 Adsorption

The performance of AC is impacted by operational factors including temperature, surface chemistry, textural properties, thermal, chemical and mechanical stability.

2.6.1 Temperature

2.6.1.1 Pyrolysis and Activation Temperature of Activated Carbon

Determining the appropriate temperature for carbonization is critical in determining the BAC's efficacy. A research of iron-impregnated maize stalk and cob at temperatures of 300 °C and 600 °C by Pai (2019) revealed that BAC generated at 650℃ had a larger surface area compared to Hu (2021) (Hu et al., 2021; Peng et al., 2019). This is due to vaporization of the volatiles component present in the feedstock when it is subjected to high carbonization temperature, resulting in more open pores to generate (L. Gao et al., 2021). However, raising the pyrolysis temperature further than optimum value may possibly reduce the number of functional groups and reduces the adsorption capacity (Duan et al., 2017) which can be related to the BAC's surface texture and pores deteriorating (Jung et al., 2021). Table 2.10 summarized the ideal temperature range to synthesize higher yield by varying the heating rate and carbonization temperature. It shows that slow pyrolysis is ideal to produce higher yield of BAC.

The pyrolysis process is divided into four phases where the first step includes total moisture removal at temperatures up to 100°C, whereas the second stage is associated with hemicellulose degradation at temperatures between 100 to 350°C. The third and fourth phases include cellulose degradation between 350 to 400℃ and lignin decomposition over 400℃, respectively (Al-Amrani, Lim, Seng, & Ngah, 2012). As different carbonization temperature result in different properties of BAC, selecting

optimum temperature is important. Low temperatures at the range of 300–800 °C accompanied with a slow heating rate of 5-7 °C/min^{-1} used for higher yield of AC but had a smaller surface area (Bridgwater, 2012).

Table 2.10: Pyrolysis temperature and the product yield (W.-J. Liu, Jiang, & Yu, 2015)

Pyrolysis	Heating Rate (ºC / min)	Process Temperature (ºC)	Main Product	AC Yield (wt %)
Slow Pyrolysis	5-7	300-800	AC	30-50
Fast Pyrolysis	300-800	400-600	Bio-Fuel	10-30
Flash Pyrolysis	>1000	400-1000	Bio-Gas	10-20

Activation temperature is also crucial to determine the yield and overall performance of BAC. The activation temperature of BAC from apricot shell activated at 400 ºC and, BAC from paulownia wood activated at 300ºC has been compared where the BAC yield were 26.2% and 42% (Y. Guo et al., 2015). This reduction on the yield might be due to the condensation of volatile products of the hydro aromatic structure of produced BAC, where the composition of volatile components was varied in all the biomass (Ekanayake et al., 2021). This study also has proven that higher yield did not promise a higher surface area or adsorption rate, where the paulownia wood had lower surface area compared to apricot shell despite the higher yield of BAC. The type and quantity of activating agent employed during the carbonization process, as well as the carbonization temperature, determine the final characteristics of activated porous carbons. Carbonization and activation temperature are important in influencing the functional groups, crystallinity, and specific surface area of BAC (Goel et al., 2021).

2.6.1.2 Carbon Dioxide Adsorption Temperature

The steady decline in CO_2 adsorption capability observed as the adsorption temperature increase was due to the exothermic nature of the CO_2 adsorption process (Abd, Naji,

Hashim, & Othman, 2020). According to Ho (2017), high temperature had a detrimental effect on the CO_2 uptake performance of MgO-based BAC, where the greatest uptake was observed at 303 K and reduced when the temperature was raised to 623 K (K. Ho et al., 2017). Similarly, in the study of Tuan (2018) (Tuan & Lee, 2018), have reported a MgO-based BAC prepared using precipitation method and Gao (W. Gao, Zhou, & Wang, 2018) who have prepared leaf-like MgO-based BAC using urea hydrolysis method with magnesium nitrate hexahydrate experienced greater CO_2 adsorption when the temperature raised more than 400K. It could be inferred that the morphological structure, particularly sheet, leaf, and flake shaped structures, can be an advantageous factor for the adsorbent adsorption effectiveness in terms of boosting the thermal stability at moderate adsorption temperatures. In the study of Wang (2021) an Al-Mg-based BAC was used and the adsorption temperature was varied as 25, 50, 75, 100 ◦C.

The CO_2 uptake of the BAC was 4.50, 4.30, 3.62, 3.47 mmol/g, respectively and it could be said that higher adsorption temperature was not conducive to the CO_2 capture. In the study of Dai (2016) has stated that, when the adsorption temperature reached 25°C, CO_2 adsorption process with MgO-based BAC reached its equilibrium (Dai, Noble, Gin, Zhang, & Deng, 2016). However, when the process temperature was raised to 140°C, nearly 97% of the adsorbed CO_2 was desorbed (Jagodzińska et al., 2021). As CO_2 uptake capacity increased, the relationship between the isosteric heat and the amount adsorbed exhibited exponentially decreasing correlation (at a low adsorption temperature). A low isosteric heat value indicated that the regeneration of BAC based adsorbents would require less energy (K. Chen et al., 2022). The CO_2 adsorption on the adsorbent occurs in two stages, the first is physical adsorption at the adsorbent's surface, and the second is internal diffusion of CO_2 through the adsorbent's pores (Gosu et al., 2018). As a result, the lower process temperature facilitates the physical adsorption, while the higher process

temperature facilitates the chemical adsorption. Although the chemical adsorption is facilitated by the molecules' kinetics as a consequence of the rise in temperature, the overall adsorption efficiency is crippled due to the CO_2 weak interaction with the pores. As the evidence for this finding, the study of Creamer (2012) mentioned that as the temperature increased from 273 to 333 K, MgO-based BAC nanoparticle adsorbed more CO_2. This may possibly be explained by the terminal hydroxyl (-OH) groups, which contributed to the increased CO_2 adsorption and production of hydrogen carbonate species. In addition, the magnesium species (Mg^{2+}-O^{2-}), which formed bidentate carbonate complexes, also caused an increase in CO_2 adsorption at high temperatures (Creamer et al., 2018).

2.6.2 Textural Properties

The carbonization of BAC influences the pore size at the initial stage as the release of volatile components from the feedstock. In the study of Serafin (2021) mentioned that compared to BAC produced at 450 ºC, the BAC at 500 ºC had ten times greater surface area. The surface area increases as the temperature and duration of pyrolysis increased, possibly due to the release of volatile matter (Serafin et al., 2021). On the other hand, in the study of Yang (2018) the surface area of corn stalk BAC impregnated with Fe at 600 °C resulted in mesopores and microspores structure where primary pore size distribution was less than 2nm, and the surface area was 603.24 m^2 / g (Yang et al., 2018). Similarly, Cu ion modified BAC possessed a greater surface area as high as 1316 m^2 / g (Hosseini et al., 2015) . The surface area of BAC is related to the type of biomass used. For example, the surface area of peanut shell BAC is less than rice straw BAC, which may be contributed to the feedstock's varying levels of cellulose and hemicellulose. For instance, the surface area of pine is greater than the surface area of nut shell (Ormsby, Kastner, & Miller, 2012). Similarly, at the same process condition, the BAC produced from rice husk

was 8.5 times greater in CO_2 adsorption than BAC produced from sludge waste (Cha et al., 2010).

Based on the N_2 adsorption-desorption isotherms and pore size distribution diagrams from previous studies, most of the BAC fall under a mixed isotherm of Type I and Type IV, and the hysteresis loop of type H4. It is clear that the mesoporous material caused by the N_2 capillary's condensation. In the study of Pu (2021)(Pu et al., 2021), the bi-metal impregnation on MgO-Al/BAC experienced composite which included a large number of micropores and mesopores (0-50 nm) after the acid activation (R.-Z. Wang et al., 2020). BAC without metal oxide had a higher N_2 adsorption capacity due to the large number of empty pores while the specific surface area and total pore volume of bi-metal impregnated adsorbent had been reduced. Similarly, the study of Wang (2014) found that the surface area of adsorbent decreased from 1176.58 to 880.65 m^2/g as the amount of metal impregnated is increased which is also similar to few other study and this is due to the blockage of pores in BAC by metal especially at the meso-pore and macro-pore region but the CO_2 uptake increased significantly (Z. Wang, Shi, Li, & Zheng, 2014). Another study also exhibited the similar situation where in MgO-based bamboo shell BAC had the third-highest surface area of 419 m^2/g of all samples prepared but this adsorbent has the maximum adsorption of CO_2 (Ismail, Rashidi, & Yusup, 2022). Based on the result obtained from these studies it could be suggested that CO_2 adsorption capacity is not proportional to the surface area and the CO_2 adsorption process not only dependent on physical adsorption (Wei et al., 2012).

Pore size plays a crucial role in determining the capacity of adsorption of CO_2. According to the "pore size" classification of the IUPAC, pores that are 50 nm or greater are macro-sized, and those that are between 2 nm and 50 nm are meso-sized (Ghosh et al., 2019). The pore size of BAC should be ideal for the adsorption of CO_2 where it should

not be smaller than the molecular size of CO_2, which is 0.33 nm and falls under the micro pore category (Asadi-Sangachini et al., 2019). The study of Dissanayake (2020) found the pores with a diameter of 0.5 nm performed CO_2 adsorption at lower capacity, meanwhile those with a diameter of 0.8 nm had found a higher CO_2 adsorption at 1 bar (Dissanayake et al., 2020). More pores are produced when more organic matter is released from the feedstock during carbonization, allowing for more CO_2 interaction (Lin & Zheng, 2021). As the carbonization temperature risen from 400 to 500 ºC, micro pores also increased but there was no increase in the macro pores at 500 ºC (Dissanayake et al., 2020). This might be possibly due to when the temperature exceeded 500°C, neighboring pores could become fully fluidized while reducing the pore volume (F. Li et al., 2010). BAC made from pine wood was characterized as micro porous and the findings also showed that the two step carbonization approached creates BAC with greater pore structure (Ahmed et al., 2019). Activation of BAC is a major contributor to the pore size. For instance, due to the high proportion of small microspores in the framework, KOH activation of garlic peel BAC resulted in an excellent CO_2 capture performance (G.-g. Huang et al., 2019). However, excessive activating agent and activation temperature would severely damage existing micro pores and small meso-pores, resulting in a reduction in micro porosity (Yargicoglu et al., 2015).

2.6.3 Surface Chemistry

The surface chemistry of BAC is depending on the CHNOS element present on the feedstock of BAC. This element determines the surface chemistry of BAC which is acid, base or neutral. The presence of carboxylic acids, anhydrides, lactones, lactols, and phenols indicates an acidic adsorbent of BAC, while the presence of quinone, chromene, pyrone and nitrogen groups indicate basic BAC and lastly, the carbonyl and ether groups showcase a neutral BAC (Jeguirim, Belhachemi, Limousy, & Bennici, 2018). Similarly,

the presence of O-H symmetric stretching of hydroxyl and C–H vibrations in methylene functional groups Al-based BAC was found in the study of Hosseini (2015) and Ismail (2022) (F. Wang et al., 2021) (Hosseini et al., 2015). The olefin C=C skeletal and C–O stretching vibration on Fe/Mg-based BAC was found and the author have predicted the presence of polycyclic aromatic skeleton (Lahijani et al., 2018). It was also noticed that, as the carbonization temperature of BAC increased, a less spikes was observed in the FTIR spectrum. This showed that carbonization at high temperature eliminated the surface functional group of BAC and this was observed in the study of (Lahijani et al., 2018) when walnut shell based BAC generated at 900℃ resembled a peak-free FTIR spectrum.

However, a sharp peak was found after the loading of metal oxide indicating the presence of metal on the BAC. Similar to the previous study, Wang (2021) (Shang et al., 2016), also encountered similar peaks were ascribed to iron oxide (III) crystalline phases and iron oxide (II) crystalline phases. X-ray diffraction analysis (XRD) used to study the crystallinity of BAC and the study of (Lahijani et al., 2018), showed the presence of graphitic carbons, crystalline structure of aliphatic side chains and amorphous carbon on the BAC structure. The study of Olajire (2010) [39], showed the successful impregnation of metal by finding the changes in weight of initial BAC and final BAC. The rise in the weight of BAC showed the presence of metal (iron, magnesium, and aluminium). Scanning electron microscope (SEM) can be used to evaluate the structure and arrangement of pores on the structure of BAC. The study of Jeguirin (2010) (Yang et al., 2019), the SEM analysis of the iron-manganese-sulphur modified BAC revealed a thread structure that was uniformly placed on the BAC. This thread structure was comprised of a mixture of iron, manganese, and sulphur that was efficiently absorbed by the BAC. In overall, the surface characterization of BAC will help to provide additional information

on functional group presented on the BAC and it is also another way of ensuring the impregnation of metal ion on the BAC.

2.6.4 Thermal, Mechanical and Chemical Stability.

BAC is frequently applied in severe environments, making its stability a crucial issue to consider. It is essential to choose BAC with superior chemical, mechanical, and thermal stability. Typically, the industrial gas stream is composed of 73–77 % N_2, 15–16 % CO_2, 5–7 % water vapor, 3–4 % O_2, traces of SO_x, NO_x, and hydrochloric acid, and these gaseous contaminants can damage the entire CO_2 separation system, including the structure of BAC (Leus et al., 2016). In terms of chemical stability, BAC's capacity to withstand and function in varying pH levels of acid and alkali is being evaluated. In the investigation of Shang (2019) (Leus et al., 2016), Zn-based BAC was characterized under XRD, and found that there was no modification on the structure of BAC after being soaked in acid and alkaline solution for several hours. This study indicated that produced BAC was chemically stable between pH 1 and 13. When a BAC is not chemically stable, various pH levels might destabilize its surface, resulting in poor CO_2 adsorption. As indicated previously, a chemically stable BAC will undergo minimal or no structural changes when exposed to varying pH without altering CO_2 adsorption effectiveness. This situation relies heavily on the inter- and intramolecular interactions of BAC (Kang, Khan, Haque, & Jhung, 2011). It is also essential to discuss the nature of the metal ions immobilized on BAC. BAC degrades often as a result of chemical reactions between central metal ions and environmental components. To synthesize a chemically stable BAC, it is optimal to impregnate with a more inert central metal ion (Kang et al., 2011). BAC chemical stability was explored in the by synthesizing Chromium-based BAC (more inert) and Vanadium-based BAC (less inert) (Kandiah et al., 2010). This study discovered that the structure of Chromium-based BAC remained unchanged, whereas the structure

of Vanadium-based BAC disintegrated, with the chemical stability sequence being Cr>Al>V. The figure derived from the analysis of Li (2016) explained that the core metal ion of Cr and Rh was more chemically stable when synthesized via BAC (Jhung, Khan, & Hasan, 2012). In contrast, thermal stability was referring to the bond between metal atoms and the BAC structure of biomass.

Thermal stability is one of the most essential stability factors to consider in comparison to others. TGA is used to research the thermal stability of BAC, and it was discovered that Pt-based BAC was more thermally stable than Zr-based BAC when employed in nanosized and could tolerate temperatures beyond 600K (J. C. Tan & Cheetham, 2011). This study it was found that although there were many metal salt abundantly available in sea water, sodium chloride, potassium chloride and calcium chloride salts as not suitable to under pyrolysis or hydrolyzation due to their stability (W.-J. Liu, Jiang, Tian, Ding, & Yu, 2013). The study of Kandiah (2010) showed the adsorption capacity of sodium modified AC is only 67 mg / g, which is lesser compared to other metals due to the sodium's stability, which began to decompose at temperatures greater than 550 °C (Kandiah et al., 2010). As previously stated, the degradation of metal salts, in this case sodium nitrate, began with the breakdown of sodium nitrite and continued with the breakdown of sodium oxide as in Eq (2.1)

$$NaNO_3 \rightarrow NaNO_2 \rightarrow Na_2O \quad (2.1)$$

As a result, the sodium oxide is less likely to form at the low temperature used in the study (500 °C). Sodium nitrate is unlikely to degrade into sodium oxide. Mechanical stability is also crucial for BAC especially when they are exposed to chemicals and washing/filtration (H. Wu, Yildirim, & Zhou, 2013). Ideally mechanically stable BAC should have great physical properties such as compressibility and rigidity. As the primary objective of BAC synthesis is to produce a highly porous adsorbent, this highly porous

BAC has poor mechanical stability, which can result in the disintegration of BAC structure (Van de Voorde et al., 2015). Highly porous BAC are unstable, therefore using support such as AC, zeolite or MOF's to be incorporated to produce a structurally stable and highly porous hybrid adsorbent for the adsorption of CO_2 (Luo et al., 2022). This incorporation can result in a high mechanically stable BAC.

2.7 Adsorption Mechanism of Carbon Dioxide Capture

The CO_2 adsorption mechanism in porous BAC can be explained into five sequential phases. The five steps include (a) Bulk diffusion where CO_2 diffuse from the concentrated state to the surface of BAC, (b) Film diffusion where the CO_2 molecule diffuse via the gas film, (c) Interparticle diffusion where the CO_2 molecule adsorbed into the pore of BAC and (d) Intraparticle diffusion where the CO_2 molecule adsorbed onto the crystalline grains of BAC and lastly (e) Surface adsorption where the CO_2 molecule react/interact with the surface/functional group of BAC (Ammendola, Raganati, & Chirone, 2017). In general, the fifth step is very quick, and the resistance correlated found to be minimal (Q. An, Miao, Zhao, Li, & Zhu, 2020). The adsorption mechanism occurs in basis of either one of this adsorption sequence or sometimes a combined sequences of adsorption mechanism can occur.

2.7.1 Physisorption

In physisorption, the CO_2 molecules was adsorbed on the surface of the BAC by van der Waals forces and have a low heat of adsorption which is just slightly more than the heat of sublimation of the BAC. CO_2 adsorption heat ranges from -25 to -40 kJ/mole on BAC, which is comparable to sublimation heat (Alfe et al., 2021). The energy required to desorb a given amount of CO_2 is reduced due to the low heat of adsorption. CO_2, on the other hand, is less likely to adsorb onto the porous substrate. Physisorption is typically known

as an exothermic reaction with low enthalpy values due to weak van der Waals attraction forces, but it can also be linked to an adsorption energy. Tan (2020), he investigated the surface appearance, porous structure, and physisorption capabilities of BAC with various biomass carbon nano-porous structures (B. Tan, Cheng, Zhu, & Yang, 2020). Porous substances are typically suitable adsorbents for physisorption because of the relationship between porosity and increased surface area (D. Li, Tian, et al., 2015). The amount of molecule adsorbed, according to their findings, was connected to the topological dimension of carbon pores and the pore volume of BAC, but inversely proportionate to the number of pores filled within the metal oxide (Goel et al., 2021). Furthermore, they discovered that the rate of physical adsorption increased with the number of folds and surface area, and that physiosorbed desorption temperatures were low due to their weak connections.

Addition of metal oxide onto biomass-based AC alters the structure by forming crystal edges with a high degree of basicity therefore, the acidic CO_2 attracts more metal oxide to this site (Daub, Patey, Jack, & Sallabi, 2006). Also, in the study of Creamer (2016) aluminum modified AC was found to have a greater capacity for adsorption than magnesium and iron. This was because aluminum impregnated AC had a greater surface area and an excessive of active sites, which aided in physical adsorption (Creamer et al., 2016). Metal modified walnut based AC had a lower total surface area and pore size than unmodified walnut based AC (Creamer et al., 2016). Given that surface area is a critical factor in CO_2 adsorption, this will undoubtedly reduce the adsorption capacity. In the study of Alfe (2021) the CO_2 adsorption isotherms demonstrated the presence of considerable interactions in Cu- and Al-based BAC, whereas physisorption occurred in Fe-based BAC (Alfe et al., 2021). Although BAC has a promising textural quality, the adsorption properties also limited by changes in the physicochemical/chemistry of the

pores (Asadi-Sangachini et al., 2019). This could be due higher surface area of Fe compared to Cu and Mg. Therefore Fe-BAC favored physisorption than chemisorption. As summary, the addition of an optimal amount of metal oxide enhances CO_2 adsorption based on the previously published work.

2.7.2 Chemisorption

The chemisorption of CO_2 onto BAC can be evaluated using characterization of BAC after adsorption and also by identifying the heat of adsorption. The CO_2 gas undergoes a covalent chemical reaction to connect to specific active sites on the BAC in chemisorption, with a substantially higher heat of adsorption, which is almost equal to the heat of reaction (Alfe et al., 2021). Chemisorption has a higher heat of adsorption compared to physisorption due to their strong chemical bond. During the adsorption, CO_2 is adsorbed on the surface of BAC and chemically bonded to form carbonates as shown in Table 2.11. Therefore, the heat of adsorption for chemisorption is ranging from 40-400 kJ/mol (Barber et al., 2013). The CO_2 TPD profile reveals the carbonate formation such as bicarbonate, bidentate carbonate, and monodentate carbonate which correspond to weak, medium, and strong adsorption basic sites as summarized in Table 2.12. The desorption temperature of BAC is also varied according to the type of bond formed during chemisorption. The synthesis of bicarbonate is due to the interaction of hydroxyl groups, whereas the synthesis of bidentate and monodentate carbonates is due to the bonding between CO_2 and Mg^{2+} and/or O^{2-}. (Goel et al., 2021). In addition, it can be determined that the strength of the basic sites is dependent on the amount of coordinated electronegative metal ions, that could be increased by employing BAC with a large surface area which facilitates an abundance of O^{2-} sites. Since flue gas from coal-fired power plants comprises water vapor, the presence of H_2O also affects the interaction between metal ion and CO_2.

Table 2.11: Desorption temperature based on the type of active sites (Song et al., 2016a).

Carbonates	Type of Active Sites	Desorption Temperature (K)
Bicarbonate	Weak	<473
Bidentate Carbonate	Medium	473 to 573
Monodentate Carbonate	Strong Basic Sites	>573

This is one of the practical applications challenges faced by the industries. During the carbonation process, both the MgO-based BAC and $Mg(OH)_2$ -based BAC are capable of generating $MgCO_3$ in the presence of H_2O (Song et al., 2016a). The carbonation process is dominated as in Eq (2.2) and Eq (2.3)

$$MgO + H_2O \rightarrow Mg(OH_2) \quad (2.2)$$

$$MgO(OH_2) + CO_2 \rightarrow MgCO_3 + H_2O \quad (2.3)$$

The production of CO_3^{2-} and H^+ ions take place when water surrounds MgO (Song et al., 2016a). Free Mg^{2+} ions combine with CO_3^{2-} to produce $MgCO_3$. This showed that water vapor serves as a channel for enhanced chemisorption interactions between magnesium oxide and CO_2 on BAC. Similarly, the relative humidity increases from 30 % to 70 %, the CO_2 adsorption of MgO increases from 0.82 to 3.42 mol/kg (Danish et al., 2021). Nonetheless, a high-water content in the adsorbent system will necessitate a large amount of energy due to sensible heat. Similarly, MgO impregnated coconut-based BAC also demonstrated the formation of bicarbonate via the hydroxyl group interaction, as well as the forming of bidentate and monodentate carbonates via the adhesion between CO_2 and magnesium ion (Mg^{2+}) and oxygen ion (O^{2-}) (Y. Li et al., 2013). Moreover, the strength of basic sites is proportional to the amount of linked electronegative metal ions. This aspect can be boosted by using BAC with a high surface area, which provides more space for O^{2-} sites (Q. Wang et al., 2011). Other than the formation of carbonates, the

metal salt used in pyrolysis process is also playing a huge role for the adsorption of CO_2. On the other hand, the magnesium chloride hexahydrate applied to the biomass successfully decomposed and hydrolyzed, resulting in increased pore volume and surface area (W.-J. Liu et al., 2013). Metal chloride salts have a high dehydration capacity for carbon polymers including cellulose, hemicellulose, and lignin, which prevents the production of hefty tars on the surface of BAC, which might potentially plug the open pores (Rufford, Hulicova-Jurcakova, Zhu, & Lu, 2010).

Table 2.12: Type of carbonate formation during CO_2 adsorption according to the type of active sites (Song et al., 2016b)

Type of Active Sites	Type of Carbonate	Structure
Weak	Bicarbonate	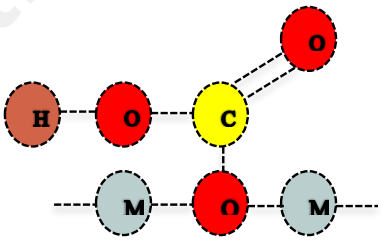
Medium	Bidentate Carbonate	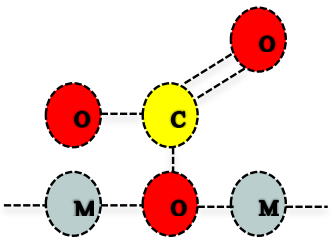
Strong Basic Sites	Monodentate Carbonate	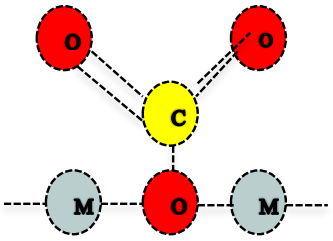

The study of (Lahijani et al., 2018) stated, when magnesium nitrate salt was combined with AC, an endothermic reaction occurred in which the magnesium nitrate

decomposed into magnesium oxide, enhancing CO_2 adsorption. The reaction equation is as follows in Eq 2.4, 2.5 and 2.6

$$Mg\ (NO_3)_2.6H_2O \rightarrow Mg\ (NO_3)_2 + 6\ H_2O \uparrow \quad (2.4)$$

$$Mg\ (NO_3)_2 \rightarrow MgO + 2\ NO_2 \uparrow + 1/2\ O_2 \uparrow \quad (2.5)$$

$$Mg{-}O + CO_2 \rightarrow Mg{-}O \ldots CO_2\ (ad) \quad (2.6)$$

Excoecaria cochinchinensis leaves based BAC was impregnated with iron oxide and demonstrated a monolayer chemisorption with q_{max} of 84.8 mg/g (Dhiman & Sharma, 2019). This was due to the excellent functionality of BAC at optimum pH, with great electrostatic attraction and chemisorption between active sites of iron oxide with functional groups of the CO_2. Additionally, the modification of metal oxide could raise the number of pores, which would facilitate the adsorption of CO_2 where the impregnation of metal oxide onto BAC led to the hydrophobic, electrostatic, van der Waals, p-p interactions and hydrogen bonding of BAC resulted in a high adsorption capacity. It was determined that adsorption was endothermic and the kinetic of adsorption showed that diffusion of CO_2 was the rate limiting factor where the impregnation of iron and copper onto BAC resulted in the removal of 1.64 mmol/g of CO_2 which involved the interaction of electrostatic attraction, hydrogen bonds formation, p-p stacking, hydrophobic interaction, and surface complexion (Fallah et al., 2021). Moreover, high operating temperatures, could destroy the weak bonds and diminish the adsorption efficiency (Xing et al., 2012). But, Fe-based BAC have a large capacity for CO_2 adsorption at elevated temperatures (Galinsky, Huang, Shafiefarhood, & Li, 2013) Similarly, magnesium oxide also can be extremely effective at capturing CO_2 at elevated temperatures (200 ºC to 315 ºC) and pressures. This is because, these metals and highly stable and have great CO_2 adsorption capacity at elevated temperatures. Abanades (2005) studied the resistance created by the first sequence of bulk diffusion, the effect of varying purge gas flow rates

on the adsorption rate was examined (Abanades, Anthony, Wang, & Oakey, 2005). The study has noticed that at a lower flow rate of 20×10^6 l/min, the CO_2 adsorption was low compared to slightly higher flowrate of 40×10^6 l/min using Mg-based BAC. As the flowrate exceeded 60×10^6 l/min, there was no discernible difference in the adsorption curves, indicating that the external diffusion resistance could be disregarded (Chamas et al., 2019). This demonstrated that metal oxides were indeed critical for CO_2 chemisorption.

2.8 Isotherm Analysis

The isotherm analysis is crucial to the study of gas adsorption as the results provide accurate information on the interaction between the adsorbate and AC. It can be used to predict and compare adsorption performance, acquire insight into the mechanism process, and calculate equilibrium adsorption capacity.

The Langmuir isotherm Eq (2.7) is a widely used model to describe the adsorption of gases on solid surfaces, including the adsorption of CO_2. It assumes that adsorption occurs on a homogeneous surface where molecules do not interact with each other once adsorbed. The Langmuir isotherm is particularly suited for monolayer adsorption on a surface with a limited number of adsorption sites. The Freundlich isotherm is a model Eq (2.8) used to describe the adsorption of gases onto solid surfaces, including the adsorption of CO_2. It is particularly suited for heterogeneous surfaces and situations where adsorption occurs on multiple layers or in regions with varying affinities. The Freundlich isotherm is often used for non-ideal adsorption processes.

The Temkin isotherm Eq (2.9) assumes that the heat of adsorption of all the molecules decreases linearly with coverage due to adsorbent–adsorbate interactions. The adsorption is characterized by a uniform distribution of the binding energies, up to some

maximum binding energy. The Dubinin-Radushkevich (DR) isotherm Eq (2.10) is used to describe the adsorption behavior of gases on porous materials like AC. It is suitable for describing physical adsorption at relatively low pressures. The DR isotherm considers the interaction between gas molecules and the adsorbent's surface and incorporates the adsorbent's micropore structure.

The Harkin-Jura (HJ) isotherm Eq (2.11) is a model used to describe the adsorption behavior of gases on solid surfaces, particularly in cases where the interaction between adsorbate molecules (such as CO_2) plays a significant role. The HJ isotherm considers the lateral interactions between adsorbed molecules, which can affect the adsorption process. The Halsey isotherm Eq (2.12) is a model used to describe the adsorption of gases onto porous materials like AC. It considers multilayer adsorption, where gas molecules form layers on the adsorbent's surface. The Halsey isotherm is an extension of the Langmuir isotherm and is particularly useful for understanding adsorption behavior at high pressures.

The Elovich isotherm Eq (2.13) is a model used to describe chemisorption processes, where gas molecules are strongly bound to the adsorbent surface. It is applicable when the adsorption process involves a chemical reaction between the adsorbate (such as CO_2) and the adsorbent. The Elovich isotherm is often used to describe adsorption on heterogeneous surfaces. Isotherm study was conducted by fitting the data into different isotherm models. The details of each isotherm are described in Table 2.13. In determining the isotherm constant, it is however easier to transform the isotherm equations into linear form and then applying the linear regression as shown in Table 2.13.

Table 2.13: Equilibrium isotherm models used for the CO_2 adsorption onto adsorbents (Zaini, Arshad, & Syed-Hassan, 2023)

Model	Non-Liner Model	Equation
Langmuir	$q_e = \frac{q_{max} K_L P_e}{1 + K_L C_e}$	(2.7)
Freundlich	$q_e = K_F P_e^{\frac{1}{n}}$	(2.8)
Temkin	$q_e = \frac{RT}{b_T} \, In \, A_T P_e$	(2.9)
Dubinin-Radushkevich	$q_e = (q_m) \exp(-B_D \varepsilon^2)$	(2.10)
Harkin-Jura	$q_e = \frac{A_{HJ}}{B_{HJ} - \log P_e}^{\frac{1}{2}}$	(2.11)
Hasley	$In \, q_e = \frac{1}{n_H} \, In \, K_H - \frac{1}{n_H} \, In \, P_e$	(2.12)
Elovich	$In \frac{q_e}{P_e} = InK_e q_m - \frac{q_e}{q_m}$	(2.13)

Where, q_e (mmol/g): experimental adsorption capacity of adsorbents at equilibrium, K_F ($mg^{1—1/n}$ $L^{1/n}$ $g^{—1}$): Freundlich isotherm constant related to the sorption capacity, P_e (bar): CO_2 adsorbate equilibrium pressure, n: a constant which gives an idea of the grade of heterogeneity, K_L (1/bar): Langmuir constant related to the affinity of the binding sites and the energy of adsorption, P_o (bar): highest initial pressure, R_L: dimensionless Langmuir equilibrium parameter, q_m (mmol/g): maximum monolayer adsorption capacity of the adsorbent, R (8.314 J/mol.K): universal gas constant, T (°K): absolute temperature, b_T (J/mol): Temkin constant related to heat of adsorption, A_T (L/mg): equilibrium binding constant corresponding to the maximum binding energy, B_D (mol^2 /kJ^2): Dubinin-Radushkevich isotherm constant of adsorption energy, ε: Polanyi potential related to the equilibrium concentration, E (kJ/mol): mean free energy of adsorption, A_{HJ} and B_{HJ}: Harkin-Jurah adsorption constants; K_H and n_H: Halsey isotherm constant.

2.9 Thermodynamic Analysis

In adsorption process, thermodynamic analysis is significant to determine the process spontaneity and reversibility of adsorption process. Thermodynamic analyses of CO_2 adsorption onto the AC have been evaluated in terms of change in enthalpy (ΔH_o), change in entropy (ΔS_o), change in Gibbs free energy (ΔG_o), as well as activation energy (E_a) of adsorption process. This thermodynamic evaluation is indeed significant because it provides a detailed information on the intrinsic energy change that take place during the adsorption process.

To determine the spontaneity of adsorption process, the Gibbs free energy (ΔG_o) change needs to be determined, as it is an important criteria for process spontaneity ($\Delta G_o<0$). Accordingly, both thermodynamic parameters which are change in enthalpy (ΔH_o) and change in entropy (ΔS_o) need to be determined prior to estimation of the Gibbs free energy (ΔG_o) change. The magnitude of ΔH_o and ΔS_o is calculated from the slope and intercept of the Van's Hoff plot, as presented in Eq (2.14)

$$\ln kL = \Delta S_o / R \quad - \Delta H_o / RT \tag{2.14}$$

Referring to Eq. (2.14), R refers to the universal gas constant (8.314 J/mole·K), T is an absolute temperature in Kelvin, while kL is the Langmuir equilibrium constant (bar-1). The calculated value of ΔH_o and ΔS_o is used to estimate the ΔG_o value, based on Eq (2.15) With reference to ΔH_o, its negative/positive sign reflects the exothermic or endothermic of the adsorption process. Here, exothermic process ($-\Delta H_o$) is associated with the release of heat to surroundings, because the total energy absorbed in bond breaking is lesser compared to the total energy released in bond making between CO_2 molecules and surface of adsorbent. On the contrary, endothermic adsorption ($+\Delta H_o$)

involves heat absorption from surroundings. Regarding ΔS_o, the sign reflects the randomness of the adsorbate at the solid/gas interface upon the adsorption in Eq (2.15)

$$\Delta G_O = \Delta H_o - T\Delta S_o \quad (2.15)$$

2.10 Summary of Literature Review

The literature review reveals that CO_2 emissions pose severe environmental threats to our planet, prompting the need for effective CO_2 adsorption systems. These works demonstrate that modifying the functional groups of the adsorbent enhances CO_2 adsorption capacity. However, no prior research has explored the modification of PKS biomass using KOH activation and functionalizing the adsorbent with magnesium oxide impregnation. Moreover, the precise mechanism behind CO_2 removal using KOH-activated magnesium oxide impregnated AC remains unclear. While interest in developing biomass-based AC for CO_2 adsorption grows, further investigation, particularly concerning surface functionality, is warranted. This study aims to contribute to this ongoing research effort by developing PKS biomass AC activated with KOH and impregnated with magnesium oxide for CO_2 adsorption. By varying critical parameters and investigating the adsorption mechanism, the research seeks to address the research gap identified during the literature review.

CHAPTER 3: METHODOLOGY

3.1 Introduction

This chapter discusses the experiment's approach, which involves carbonization of biomass, activation of biomass, and magnesium oxide impregnation. The Figure 3.1 summarizes the overall methodology of the research

3.2 Chemicals and Materials

Palm kernel shell (PKS) was obtained from a local palm oil processing factory in Selangor. Chemical reagent such as KOH (37%) and powdered MgO (99%) used for activation and modification were obtained from Sigma-Aldrich. Industrial grade purified nitrogen gas (99.9 %) , helium (99.99 %) purity and compressed CO_2 (99.8 %) gas were purchased from Linde Gas Malaysia.

3.3 Synthesis of PKS-Activated Carbon

3.3.1 Pre-treatment of PKS

The PKS sample undergone a washing process using distilled water, followed by drying in a convection type universal oven (Memmert UF 110) at a temperature of 110°C for a duration of 24 hours. Subsequently, the dehydrated PKS underwent a grinding process to reduce their size and were subsequently subjected to sieving using a 150 μm sieve. Subsequently, the resultant powdered PKS were carefully preserved in a tightly sealed container.

3.3.2 Carbonization of PKS-Char

20 g of powdered PKS was loaded into a long crucible and inserted into a long quartz tube of a tube furnace (Carbolite CTF 12/65/550) which was connected to a nitrogen flow of 500 ml/min. The inert condition prevented the biomass-oxygen reactions from forming

ash. The suitability of temperatures for CO_2 adsorption is often evaluated within the range of 500°C to 700°C (Goel et al., 2021). Heating rates within the range of 1°C/min to 10°C/min are frequently employed in various applications (Alves et al., 2022). In the present investigation, the powdered palm kernel shells (PKS) were subjected to pyrolysis at a temperature of 700 °C, employing a gradual heating rate of 5 °C/min for a duration of 90 minutes. Elevated temperatures have the potential to induce enhanced carbonization and porosity, thereby improving the adsorption capacity of the biochar (Alves et al., 2022). Following the process of carbonization, the tube furnace was turned off and the crucible was permitted to undergo cooling within the quartz tube to impede any additional interaction with the ambient atmosphere. The PKS biochar was then washed with distilled water to remove the volatile substance and dried at 110 °C for 24 hours. The resulting PKS biochar was stored in an airtight sample container and labeled as PKS-Char.

3.3.3 Chemical Activation of PKS-AC

20 g of PKS-Char and 60 g of potassium hydroxide (KOH) solution at a ratio of (1:3) was stirred continuously at 80 ℃ for 2 hours and then dried at 110 ℃ for 24 hours. The dried mixture was placed in a crucible and underwent a two-step activation process at 850 ℃ for 2 hours in a muffle furnace (Thermo Scientific Thermolyne Large Muffle Furnaces F6010). Then, the crucible was cooled to room temperature of 28 to 31 ℃. PKS-Char-KOH mixture was washed several times to remove excess KOH, and the activated biochar was dried at 110 ℃ until completely dried (Januszewicz et al., 2020). The resulting activated biochar was labeled as PKS-AC and stored in an airtight container.

3.3.4 Magnesium Oxide Impregnation on PKS-AC-MgO

A CO_2 preliminary adsorption experiment was conducted using a ratio of 1:1 and 1:0.5 (PKS:MgO). From this preliminary study the ratio of 1:0.5. This is because the ratio of

1:0.5 had more open pores and highest CO_2 adsorption capacity compared to the ratio of 1:1 with blocked pores structure and less CO_2 adsorption capacity. Magnesium oxide (MgO) functionalization was carried out using the wet impregnation method. 20 g of PKS-AC was dissolved in a solution of 10 g of magnesium oxyhydroxide (MgOH) with a ratio of (1:0.5) at 80°C for 6 hours while being continuously stirred. After 6 hours, the mixture was dried in an oven at 110 °C for 24 hours. The resulting MgO-impregnated AC was then washed several times to eliminate any excess MgO and further dried in an oven. The final AC product was stored in an airtight sample container and labelled as PKS-AC-MgO for subsequent analysis.

3.4 Characterization of PKS-Activated Carbon

All the synthesized ACs were subjected to several characterization approaches in order to evaluate the thermal behavior, elemental composition, surface chemistry, surface morphology, as well as textural characteristics.

The decomposition behavior of synthesized ACs were carried out by using a thermogravimetric (TGA) analyzer (TGA-50, Shimadzu Corp., Kyoto, Japan). Throughout the analysis, the samples were exposed to a temperature program at constant heating rate, while a balance detected the samples' weight change. Decomposition of these samples (5-10 mg) were analyzed at fixed heating rate of 5 ℃/min under purified N_2 atmosphere at temperature range between 50-500 ℃ with fixed gas flow rate of 150 mL/min (Darabi, Ghiasvand, & Haddad, 2021).

Surface morphology of these ACs samples were evaluated by utilizing the Scanning Electron Microscope (SEM) (model ZEISS ULTRA 55 Gemini). The purpose of this analysis is to visualize the external structure of the sample; before and after the

CO_2 adsorption. Prior to analysis, a small portion of samples was mounted on an aluminum stub and coated with gold to prevent charging effects and afterwards, images of these samples were taken at different magnifications (Hongda Liu et al., 2022).

Chemical composition of raw material as well as ACs were investigated by using the Energy Dispersive X-Ray (EDX) analyzer, which is integrated to SEM instrument. This analysis is significant to support the findings of chemical compositions obtained from the CHNS analyzer.

Surface area and porosity analysis of the synthesized ACs were carried out by using an automated gas adsorption system instrument (Micromeritics) at 77 K under N_2 atmosphere. Prior to N_2 adsorption-desorption process, the AC samples were degassed at 150 °C under a vacuum condition in order to eliminate moistures and any adsorbed impurities. In N_2 adsorption-desorption process, volume of gas adsorbed at the equilibrium pressure was recorded and plotted. Depending on the isotherm shape, types of activated carbon were classified into three categories, including micropore, mesopores, and macropores (Gayathiri et al., 2022). The specific surface area (SBET) of the activated carbons was estimated by using the Brunauer-Emmett-Teller (BET) equation at relative pressure (P/P_o) of 0.0-0.3. Meanwhile, total pore volume (V_{total}) was estimated at P/P_o of about 0.99. Micropore volume (V_{micro}), micropore surface area (S_{micro}), and external surface area (S_{ext}) were calculated based on the t-plot method, while mesopore volume (V_{meso}) was obtained by deducting V_{micro} from $V_{total.}$

Perkin Elmer Spectrum One Fourier Transform Infrared (FTIR) Spectroscopy was used to study the functional groups that exist on ACs structure. The FTIR spectra is a graphical illustration of percent transmission versus infrared frequency in terms of wavenumber. The FTIR analysis was performed within spectrum range of 4000 to 400

cm^{-1}, which corresponds to mid-infrared that excites mainly the fundamental vibration (Pierre-Louis et al., 2013). This FTIR analysis involved mixing of 1% carbonaceous sample with potassium bromide in a mortar pestle, and the samples were pressed to 12,000 pounds by using a manual Carver® hydraulic laboratory pellet press (L. Zhao et al., 2010).

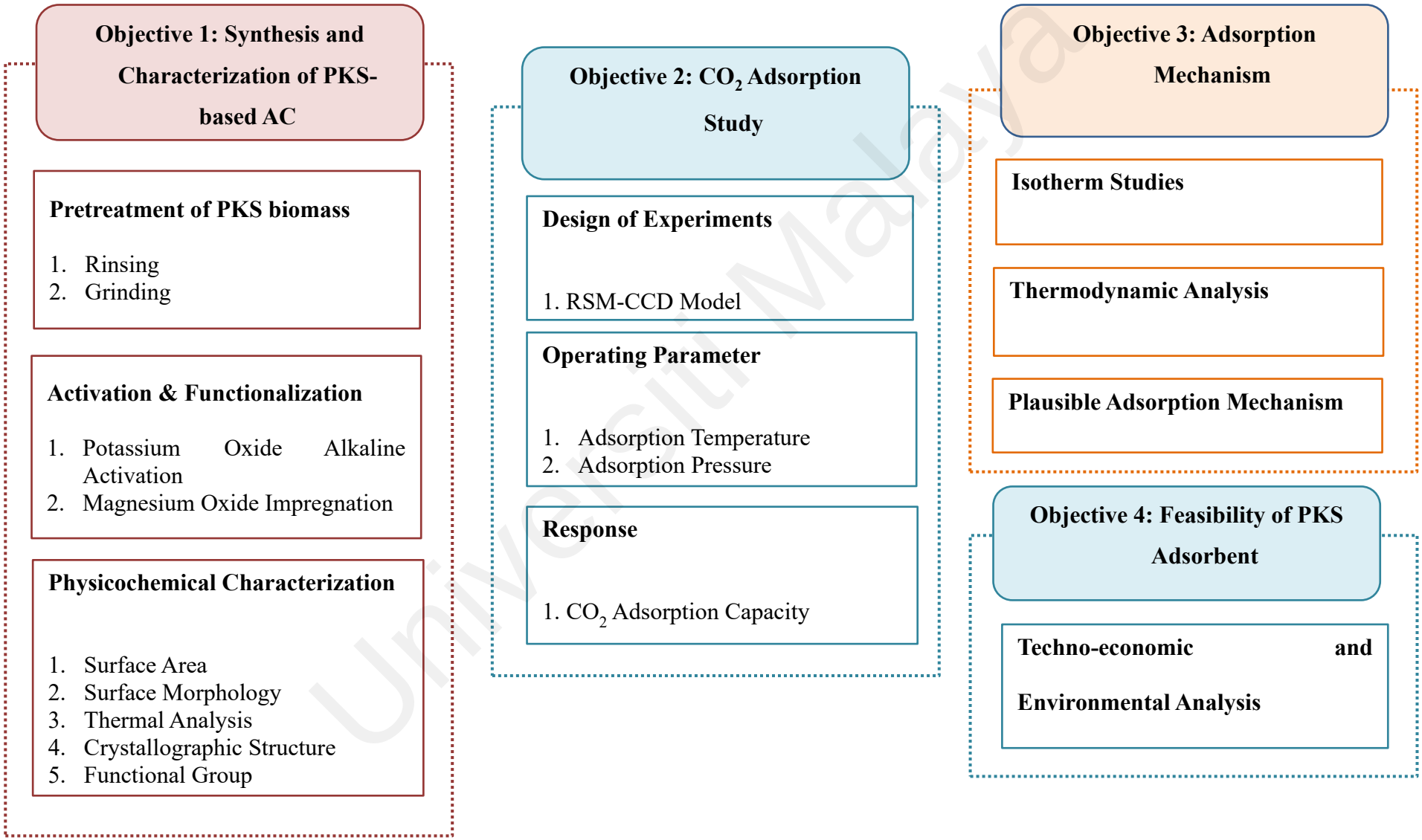

Figure 3.1: Summary of overall methodology based on objectives

3.5 Carbon Dioxide Adsorption Study

The CO_2 optimization experiment was conducted using a High-Pressure Volumetric Analyzer (HPVA) from the Particulate System at pressures ranging from 1 to 5 bar and temperatures ranging from 25 to 75℃ due to several reasons related to practicality, safety, and relevance to real-world applications. HPVA is a static volumetric adsorption device capable of operating at pressures up to 100 bar and temperatures up to 500℃. Experiments were conducted with all three of the designed adsorbents, namely PKS-Char PKS-KOH, and PKS-KOH-MgO.

At first, adsorbent used for CO_2 adsorption study was degassed at 150℃ for 4 hours under vacuum condition as shown in Figure 3.2. Roughly 0.3-0.4 g of adsorbent sample was inserted into the sample holder and covered with filter gasket to prevent the adsorbent from escaping during the process. After degassing for 4 hours, the system was let to cool down to room temperature for 2 hours. After the cooling down process, the adsorbent containing stainless-steel holder transferred to CO_2 adsorption analysis port which was filled with Julabo recirculating water bath. This water bath was used for all the experiment carried out below 75℃. It was crucial to ensure all the nuts and bolt is tighten perfectly to prevent any water to enter into the port and distract the experimental reading. Besides, this system was equipped with separate low- and high-pressure transducers to accurately measure the pressure changes during the adsorption process. Following the principle of volumetric method, firstly helium gas was dosed into the sample holder for free space measurement, assumed that helium was a non-adsorbing gas. Upon completion of free space measurement, the system was evacuated and test gas (adsorbate) was introduced into the sample holder. The adsorption was achieved when both temperature and pressure of the system was stabilized. Specifically, the isotherm equilibrium point was based on the following criteria: (i) pressure drop of <0.05 mbar in

3 min, or (ii) the maximum equilibrium time at each pressure interval was 30 min. The data acquisition was recorded in a comprehensive data analysis package via Microsoft Excel macro (v.22.0.6) software. Besides, gas compressibility factor was determined by using the NIST Reference Fluid Thermodynamic and Transport Properties incorporated into the software. Amount of CO_2 adsorbed would be reported as mmol CO_2 per gram AC (at STP, V=22414 cm^3 /mol).

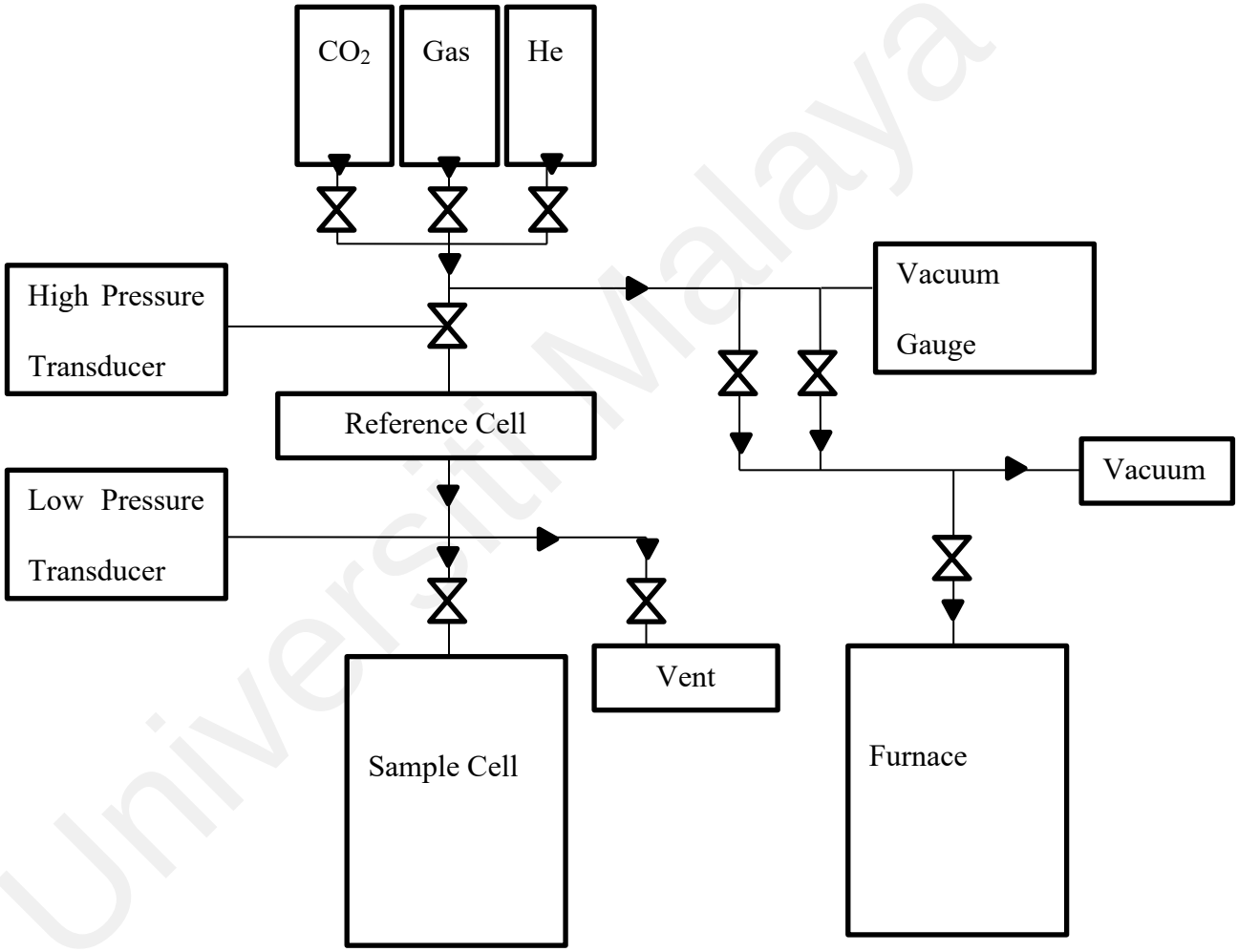

Figure 3.2: Schematic diagram of Micromeritics' High-Pressure Volumetric Analyzer for CO_2 adsorption

3.6 Design of Experiment

Fundamentally, it is inferred that alteration in operating parameter will influence the adsorption performance of synthesized ACs. To determine the optimum performance of the synthesized ACs, the CO_2 adsorption parameter should be systematically designed.

Traditional approach is expensive and time-consuming, making it unfavorable from economic perspective. Furthermore, this approach fails to describe the interaction of variables with chosen response. From engineering perspective, process optimization describes an outstanding performance of a system/process when combination of variables that contribute towards the optimum response has been implemented (N. A. Rashidi & Yusup, 2020). In effort to minimize total number of experimental runs, cost, processing time, as well as physical effort, a design of experiment which involves a multivariate approach has been established to solve the complex engineering problem (Araújo et al., 2018). Common software package to design the multivariate approach include the Design Expert (Stat-Ease Inc., USA).

Response Surface Methodology is the common multivariate technique used for the optimization process. The Response Surface Methodology is defined as a collection of mathematical and statistical technique used to define the relationship between response (dependent variable) and independent variables (Promraksa & Rakmak, 2020). Significance of the Response Surface Methodology lies in the area of design, development, and formulation of new product, and to improve existing product designs. There are several phases in the Response Surface Methodology, consisting of selection of the independent variables of the process through a preliminary screening analysis, selection of suitable experimental design and to carry out the experimental runs based on the developed design matrix, mathematical-statistical analysis of the obtained data

through fit of polynomial function, evaluation of model fitness, and determination of optimum values of the studied independent variables (N. A. Rashidi & Yusup, 2019).

The objectives of Response Surface Methodology is to predict the future responses through determination of appropriate function, and to determine the optimum operating conditions for the best response (V.R.Myneni, punugoti, Kala, N.R.Kanidarapu, & Vangalapati, 2019). Therefore, the first step in this technique is to determine the suitable approximation for true functional relationship between responses and independent variables. If the models are described by a linear function, the approximation function is termed as first-order model, and is described as Eq (3.1) (Jasri et al., 2023).

$$Y = \beta_0 + \beta_1 X_1 + \beta_2 X_2 + \cdots \quad + \beta_k X_k + \varepsilon \tag{3.1}$$

Where X_1, X_2, up to X_k are the independent variables, β_0 is the constant coefficient, β_k is the linear effects of k^{th} variables, and ε is the error observed in response Y. But, if there is a curvature found in models, a polynomial of high degree must be used, such as the second-order model, which is described in Eq (3.2) (Jasri et al., 2023).

$$Y = \beta_0 + \sum_{i=1}^{k} \beta_i X_i + \sum_{i=1}^{k} \beta_{ii} X_i^2 + \sum_{i<j} \beta_{ij} X_i X_j + \varepsilon \tag{3.2}$$

Referring to Eq. (3.2), β_{ii} is quadratic effect of i^{th} variable, whereas β_{ij} refers to cross product effect (interaction effect) between i^{th} and j^{th} variables.

There are several categories of the Response Surface Methodology which have been applied, inclusive of Central Composite design, Box-Behnken design, hybrid design, and three-level factorial design (Iberahim, Sethupathi, Bashir, Kanthasamy, & Ahmad,

2022). Based on literatures, the Central Composite design experimental design for activated carbon production has not been extensively studied. Therefore, application of Central Composite design for the CO_2 adsorption using ACs is highlighted in this research study.

Afterwards, an analysis of variance (ANOVA) is performed to estimate both individual and interaction effect between the operating variables. Significance of these variables are determined through p-value and F-value. Further, diagnostic analysis includes normal probability plot, actual versus predicted plot, etc. should be considered too for model adequacy checking, before moving to graphical analysis (N. A. Rashidi & Yusup, 2019). The graphical analysis of the predicted model is presented by response surface plot and contour plot, which demonstrates the relationship between responses and independent variable (Ranguin et al., 2020).

In this study a type of response surface with design type of central composite was used with a design model of quadratic with 9 suggested runs for each adsorbent varying pressure and temperature. Two type of factors were chosen, factor A (temperature) °C, factor B (pressure), Bar. One type of response was chosen as R1 (Adsorption Capacity) mmol/g. ANOVA analysis was used to evaluate the impact of each factor on the response variable (adsorption capacity). Based on the ANOVA results, optimum condition for CO_2 adsorption were identified. The range of these variables and complete experimental design were shown in Table 3.1 and Table 3.2 respectively.

Table 3.1: Variables and levels used in CO_2 adsorption experiment

Factor	Unit	Low (-1)	Medium (0)	High (+1)
Temperature	°C	25	50	75
Pressure	bar	1	3	5

Table 3.2: Experimental design matrix for CO_2 adsorption experiment

Run	Temperature (°C)	Pressure (Bar)
1	50.00	3.00
2	25.00	5.00
3	50.00	0.17
4	75.00	1.00
5	75.00	5.00
6	25.00	1.00
7	50.00	5.83
8	85.36	3.00
9	14.64	3.00

3.7 Desorption and Regeneration Study

Regeneration of the ACs were carried out by applying the pressure swing adsorption using the volumetric adsorption analyzer. CO_2 adsorption was measured within the pressure range of 0.1 bar to 5 bar at fixed adsorption temperature of 25 °C. Upon reaching equilibrium at 1 bar, desorption (regeneration) process was applied by stepwise pressure reduction to 0.1 bar.

3.8 Adsorption Isotherm

Adsorption isotherms of the purified CO_2 onto synthesized ACs were performed by fitting the experimental data that was obtained from HPVA II system into three types of isotherm models. The isotherm models that had been analyzed in this research study include the

Langmuir, Freundlich, and Temkin, which are represented by Eq. (2.9) to Eq. (2.15) respectively. The applicability of these isotherm models was solely based on the regression coefficient (R^2) value. The isotherm measurement was carried out at set pressure of 0 to 1 bar and temperature of 25 to 75 °C.

3.9 Adsorption Thermodynamics

The thermodynamic properties that were in terms of ΔH_o and ΔS_o were evaluated by using the van Hoff equation, as shown in Eq (2.16). The magnitude of ΔH_o and ΔS_o were calculated from the slope and y-intercept value obtained from linear plot of ln k_L (Langmuir equilibrium constant) against reciprocal of absolute temperature in Kelvin (1/T). In addition, value of ΔG_o was calculated based on Eq (2.17).

3.10 Techno-Economic Environmental Assessment

A Techno-Economic-Environmental Assessment (TEEA) is crucial when considering the introduction of any new types of adsorbent as an alternative for a commercially available adsorbent. Therefore, in this study a comprehensive analysis was done to evaluate the technical feasibility, economic viability, and environmental impact of the AC for providing valuable insights for decision-makers and stakeholders. A process flow diagram (PFD) of AC production is important in evaluating the cost of production as it provides a visual representation of the entire production process, from raw materials to the final product.

The complete investment (TCI) required for establishing a unit consists of the estimation of fixed capital expenditure (FCE) and the cost of working capital (WCC) based on Eq (3.3) (Yunus, Al-Gheethi, Othman, Hamdan, & Ruslan, 2020).

$$TCI = FCE + WCC \tag{3.3}$$

To determine the annual operating cost (AOC) of AC production, the costs of raw materials (C_{RM}), utilities (C_U), and additional expenses (C_E) must be considered. The AOC is calculated annually using Eq (3.4)

$$AOC = C_{RM} + (C_U + C_E) \quad (3.4)$$

The C_{RM} cost includes the local market price of PKS, and the chemicals required for the preparation process. The C_U cost was estimated based on the prevailing prices of water and electricity.

The specific cost of AC (tonne/USD), was calculated by dividing the annual costs of capital C_C, utility cost C_U, raw material cost C_{RM}, and extra cost C_E by the annual production (E_P) of PKS-AC-MgO using Eq (3.5) (Yunus et al., 2020).

$$\boldsymbol{C_{AC}} = \frac{(\boldsymbol{C_C + C_U + C_{RM} + C_E})}{\boldsymbol{E_P}} \quad (3.5)$$

The break-even point (BEP) in term of cost and revenue was calculated using the Eq (3.6)

$$X = \frac{FCE}{A_R + AOC} \quad (3.6)$$

To calculate the annual reduction in greenhouse gas (GHG) emissions Eq (3.7) was employed.

$$GHG\ credit\ from\ PKS - AC - MgO = PKS - AC - MgO \left(\frac{tonne}{year}\right) \times carbon\ content\ (\%) \times carbon\ stability \times \frac{44}{12} \quad (3.7)$$

The environmental evaluation based on the CO_2 emitted from the utilities system required for AC production is calculated using the ISO 14064 Eq (3.8) (Bastianoni, Marchi, Caro, Casprini, & Pulselli, 2014).

$$Utilities_{Electricity} = Input\ Value\ \left(\frac{kWh}{Year}\right) \times 0.85\ (electricity\ emission\ factor) = Output\ Value\ (kg\ of\ CO_2) \quad (3.8)$$

3.11 Safety Aspects

Appendix A summarize on the common hazards and safety measures for the material and apparatus. As a result, appropriate safeguards must be taken throughout the experimental procedure. In general, all chemicals were stored at a room temperature of no more than 30℃ with adequate ventilation. Apart from this, personal protective equipment such as gloves, lab coats, and goggles were worn throughout the experiment to avoid accidents.

CHAPTER 4: RESULTS AND DISCUSSION

4.1 Synthesis and Characterization of PKS-Activated Carbon

4.1.1 Thermal Analysis

4.1.1.1 PKS-Char

The initial weight loss is commonly within the temperature range of 0°C to 100°C, and is often attributed to the removal of moisture and volatile compounds (Alves et al., 2022). At this stage PKS-Char (Figure 4.1) undergone weight loss of 11.5% and the single endothermic peak formed for PKS-Char was also subjected at 50℃ showed that PKS-Char undergone only one major phase of weight loss at moisture evaporation. At the second phase of weight lost PKS-Char lost about 2.0% of weight which showed the devolatilization of hemicellulose, cellulose, and low molecular weight molecules (Hong, Jang, Dysart, Pol, & Lee, 2016). This showed that most of the hemicellulose, cellulose and other impurities present in PKS had been removed during the first stage of pyrolysis (Al-Amrani et al., 2012). At the third stage, PKS-Char lost about 1% weight leading to lignin decomposition indicated that the lignin properties of PKS had been successfully removed during the first step pyrolysis (Zamboni et al., 2016). In overall PKS-Char only lost about 15.4% of its initial weight where the significant portion was due to moisture loss. PKS-Char showed a high thermal stability behavior by yielding 84.6% after heating up to 500℃.

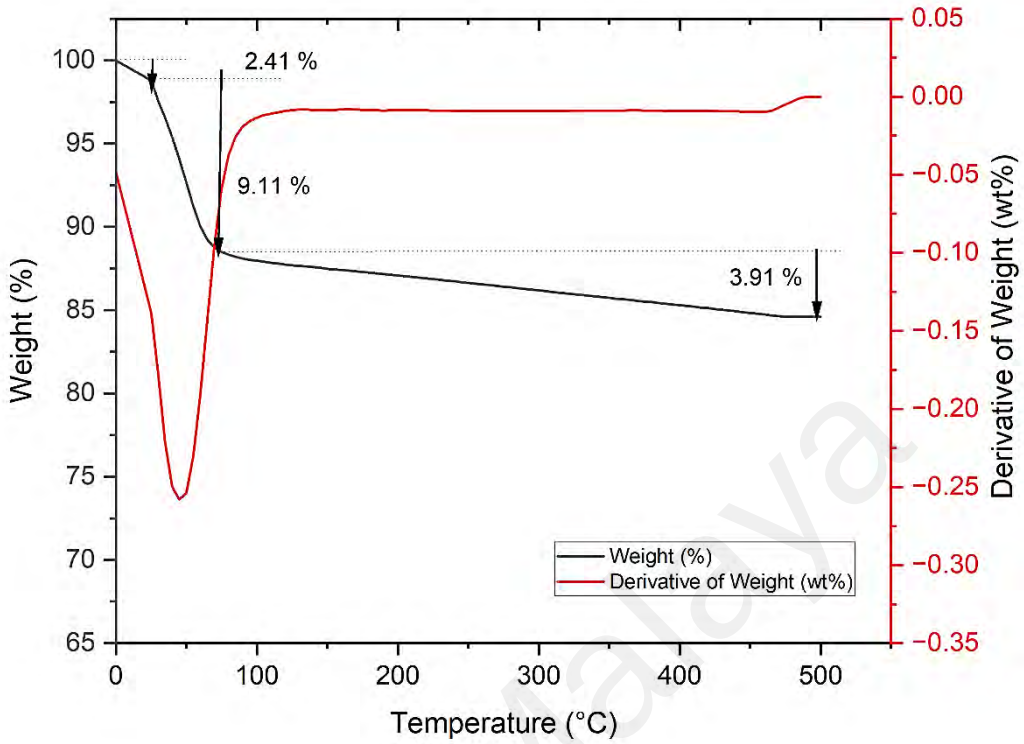

Figure 4.1: Thermogravimetric (TGA) Analysis, Weight Loss and Derivative of Weight Loss of PKS-Char

4.1.1.2 PKS-AC

PKS-AC (Figure 4.2) which have undergone KOH activation at t 850℃, showed initial weight loss of 8.2% the lowest compared to PKS-Char and PKS-AC-MgO. This could be due to double carbonization of PKS-AC contributed to the reduction of moisture content (X. Xu, Kan, Zhao, & Cao, 2016). By subjecting the PKS-AC to two step of carbonization, the moisture content was further minimized, resulting in a more reliable and consistent AC (Cai, Liu, Sun, Yang, & Li, 2022). Similar to PKS-Char, only one significant endothermic peak was observed for PKS-AC at 50°C, indicating a major weight loss due to moisture content at this temperature.

The temperature range between 100°C -400°C known as low temperature decomposition which is associated with the decomposition of certain organic components

or impurities present in the AC (Tuan & Lee, 2018). Despite multiple rinsing, some residual KOH substance remained on the surface, leading to interactions that generated volatile potassium-containing compounds like potassium carbonate or potassium oxide on the surface of PKS-AC, contributing to the weight loss observed at the second stage (C. Wu, Song, Jin, Wu, & Huang, 2013).

In the third stage, at temperatures above 400°C, PKS-AC experienced a slight weight loss of around 2.0%, indicating successful removal of lignin properties during the initial pyrolysis step (Zamboni et al., 2016). PKS-AC exhibited an overall weight loss of approximately 13.7%, demonstrating its thermal stability and potential use as a catalyst in applications at temperatures below 500°C. When compared to PKS-Char, PKS-AC showed a lower overall weight loss, indicating better moisture retention and higher thermal stability, making it a preferable candidate for various high-temperature applications.

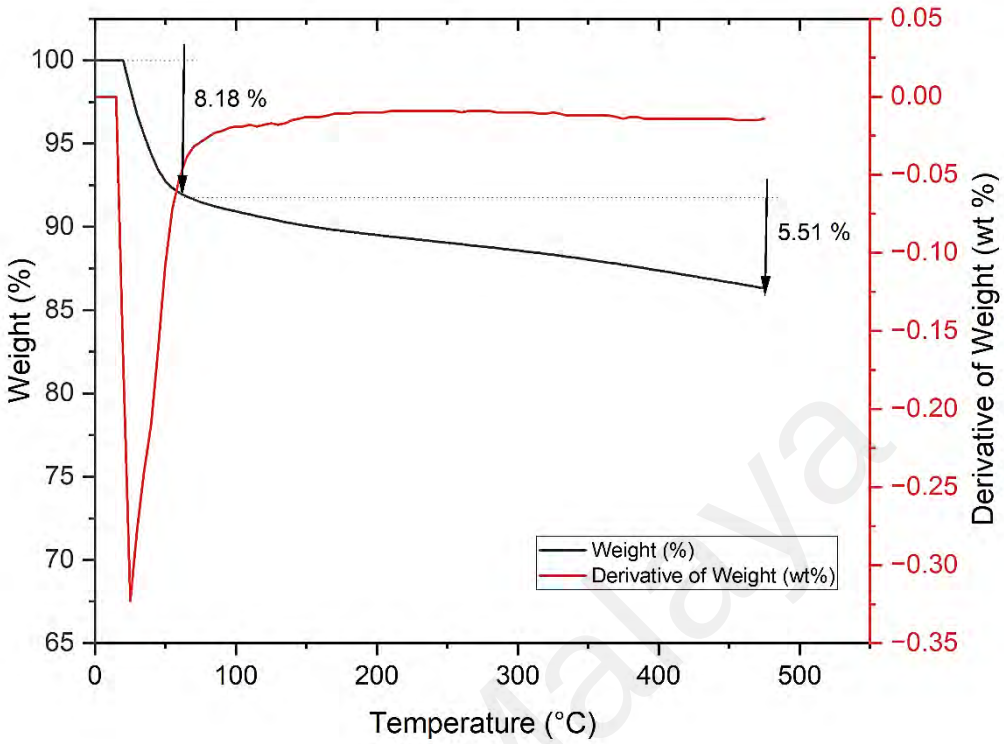

Figure 4.2: Thermogravimetric (TGA) Analysis, Weight Loss and Derivative of Weight Loss of PKS-AC

4.1.1.3 PKS-AC-MgO

PKS-AC-MgO (Figure 4.3) had weight loss of 10.6 % of its moisture weight slightly higher moisture content compared to PKS-AC because it had undergone wet impregnation of MgO after undergoing two step carbonization which led to retention of moisture. Moisture content is an important factor that can affect the performance and stability of AC in adsorption processes (Basheer, Hanafiah, Alsaadi, Al-Douri, & Al-Raad, 2021). The weight loss at this stage was further supported with the endothermic peak formed on DTA graph due to the energy required to break the bonds holding these molecules to the AC's surface led to a cooling effect. A sharp endothermic peak observed at 30℃ indicated the evaporation or desorption of volatile components, such as moisture, solvents, or other adsorbed gases (Duran-Jimenez et al., 2021).

At the second stage, PKS-AC-MgO lost 4.56 % of its initial weight due to the presence of H_2O, CO_2, and CO after the activation using KOH, which further reacted with the surrounding air and also the oxyhydroxide was formed from the mixing of MgO with H_2O (Ghosh et al., 2019). For the third stage, it could be only noticed that PKS-AC-MgO had a weight loss of 4.02 % from its initial weight during this stage, possibly due to the structure of AC with the magnesium oxide decomposing at this temperature. This is due to the formation of Mg nano metals and the reduction into its metallic form during the impregnation process (Song et al., 2016a). The absorption of more water during the wet impregnation process could be attributed to the high dielectric properties of PKS-based AC, especially in the frequency range of 0.2–10 GHz, which led to a high degree of polarization of water molecules when in contact with liquids. The dielectric properties of the adsorbents were proportional to their density, and the addition of MgO to PKS-AC increased the density of PKS-AC-MgO, resulting in increased dielectric properties with MgO impregnation. This finding was also supported with the second endothermic peak observed in DTA graph of PKS-AC-MgO around 380°C observed due to the transition phase of magnesium hydroxide to magnesium oxides, as well as the release of -OH groups from the brucite phase to provide the new phase MgO as in Equation 4.1 (Song et al., 2016a).

$$Mg(OH)_2 \rightarrow MgO + H_2O \quad (4.1)$$

Hence, the third weight loss of PKS-AC-MgO was due to the formation of stable magnesium oxides (MgO), which indicated the positive effect of magnesium impregnation. Similar result was obtained in the study conducted by (Siriwardane et al., 2017) where the thermogravimetric analysis of the synthesized $Mg(OH)_2$ suspension showed three weight loses around 150 °C, 375 °C and 450 °C.

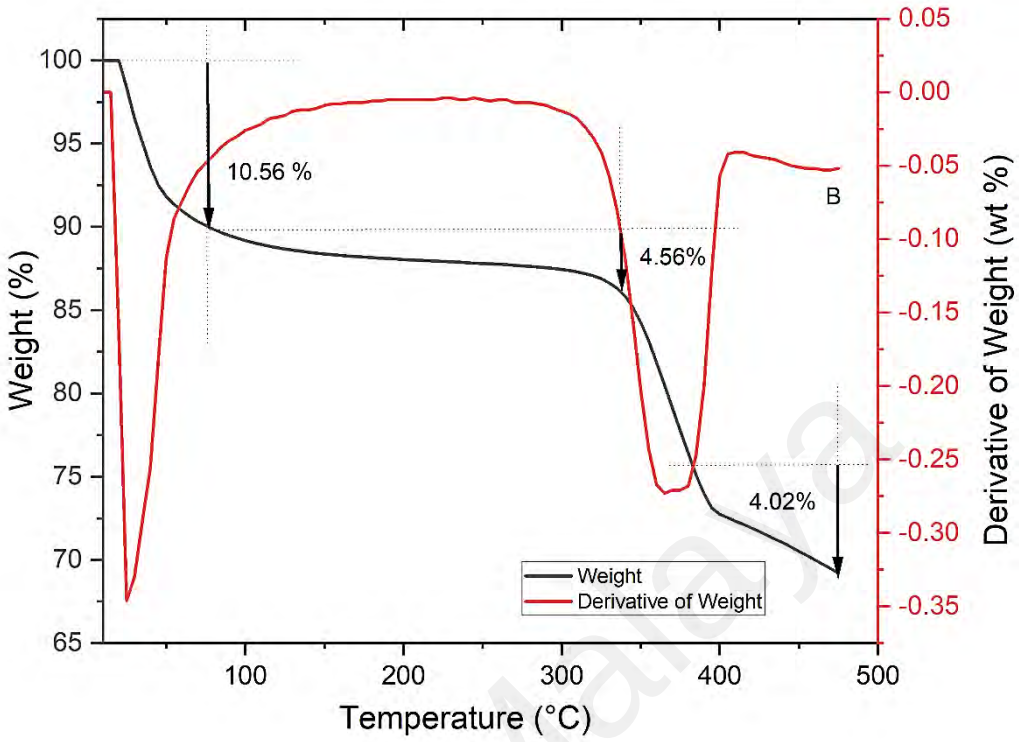

Figure 4.3: Thermogravimetric (TGA) Analysis, Weight Loss and Derivative of Weight Loss of PKS-AC-MgO

In summary, the result showed that PKS-AC had the lowest weight loss of 14.3 % followed by PKS-Char 15.4 % and PKS-AC-MgO 19.1 %. The moisture loss at the temperature below 150 ℃, was below 15%, which was in tally with reviews on optimum moisture loss for CO_2 adsorbent and the overall thermal degradation of all the three adsorbents are lower than the recommended rate of 30 % for BAC indicating the stable thermal properties at high temperatures (N. A. Rashidi & Yusup, 2019).

4.1.2 Surface Morphological Analysis

SEM-EDX analysis provide high resolution images of adsorbents at high magnifications and morphological textural behavior of the adsorbent. On the other hand, EDX analysis is similar to elemental analysis technique provides details on the element's presence on

the adsorbent samples. In this study all the three adsorbents were subjected under SEM-EDX analysis and the result obtained had confirmed the formation of porous structure and impregnation of MgO.

4.1.2.1 PKS-Char

PKS-Char, as observed in Figure 4.4 exhibits a brittle and macro-porous surface, characterized by a honeycomb-like structure with sizeable cavities. Additionally, the SEM images reveal the presence of longitudinal fibrous structures, likely derived from the cellulosic structure of PKS and these fibrous and prismatic groups contribute to the adsorbent's unique morphology and properties.

EDX analysis of PKS-Char in Figure 4.5 confirms that PKS-Char is predominantly composed of carbon, constituting 97 wt% of its composition. Additionally, a small amount of nitrogen, approximately 3 wt%, is also detected. This finding is consistent with previous research by (Boujibar et al., 2018) which reported a similar nitrogen content of approximately 2.95 wt.% in Argan shell carbonized under N_2 flow. The incorporation of nitrogen during the carbonization process served a dual purpose. Firstly, it created an inert environment, preventing the formation of ash and preserving the structural integrity of the char. Secondly, the presence of nitrogen in PKS-Char enhanced its electrochemical performance and CO_2 adsorption capacity, as demonstrated by in (Balou, Babak, & Priye, 2020) studies involving nitrogen-doped adsorbents.

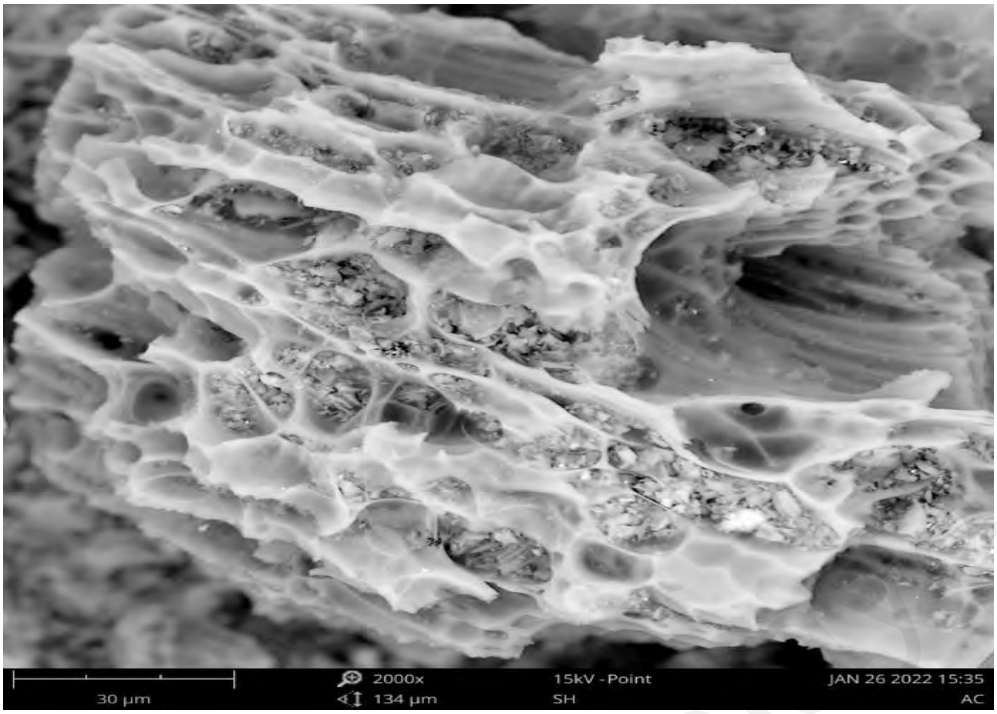

Figure 4.4: The surface morphology of PKS-Char under magnification of 2000x

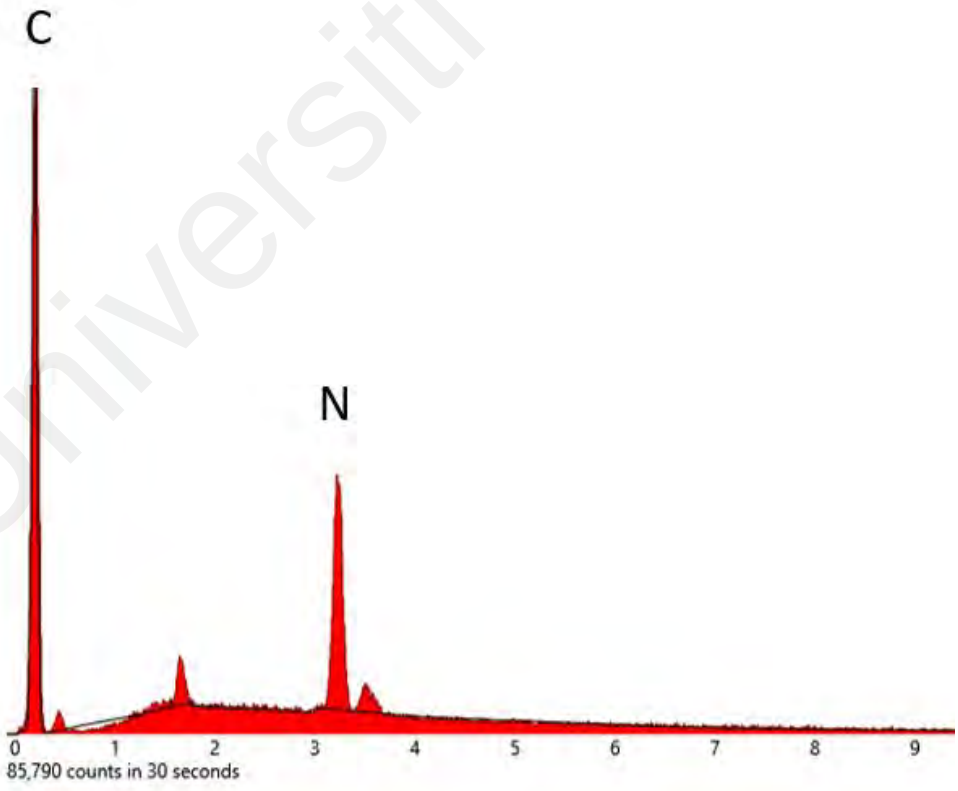

Figure 4.5: The composition of PKS-Char under EDX analysis**.**

In conclusion, PKS-Char's high carbon content, coupled with a small but significant nitrogen fraction, makes it a promising candidate for various applications, particularly in adsorption and electrochemical processes.

4.1.2.2 PKS-AC

PKS-AC and PKS-Char exhibited distinct surface morphologies and chemical compositions, as revealed by SEM and EDX analyses. SEM images of PKS-AC in Figure 4.6 display irregular and heterogeneous surface morphology with pores of varying sizes and shapes.

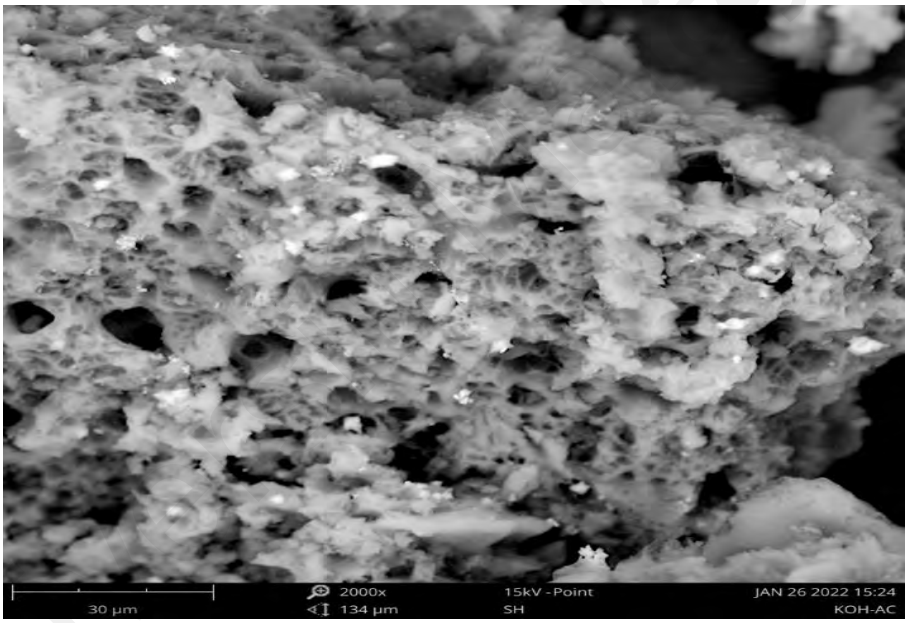

Figure 4.6: The surface morphology of PKS-AC under magnification of 2000x

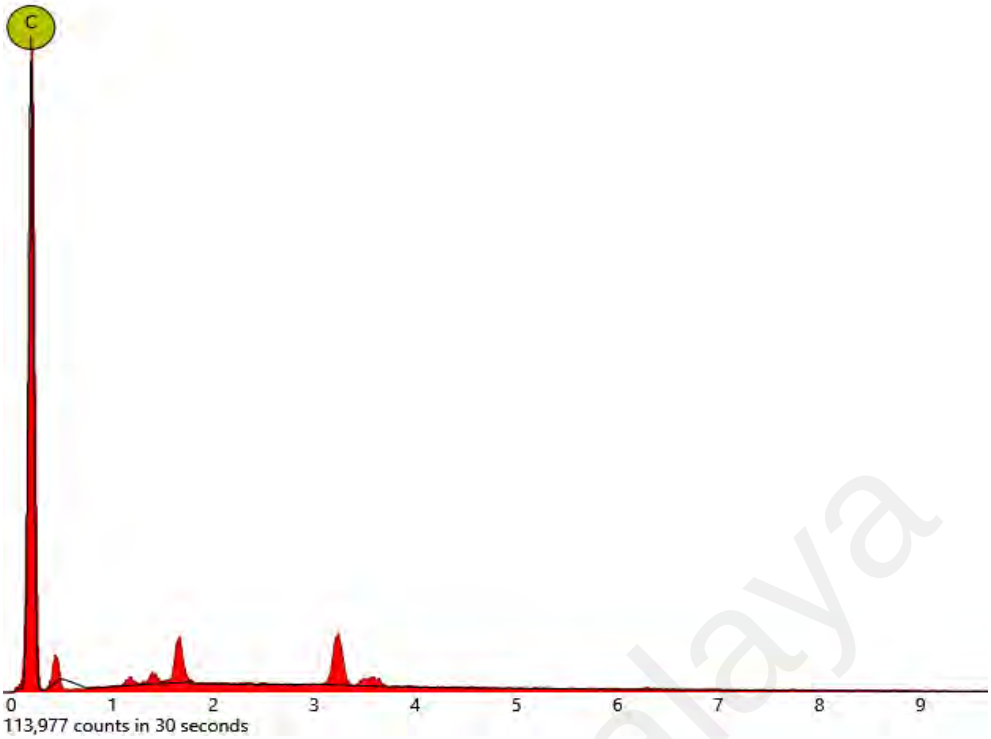

Figure 4.7: The composition of PKS-AC under EDX analysis

The result revealed that, the two-step carbonization not only reduced the moisture loss but also increased the surface area and pore volume by facilitating the diffusion of KOH molecules into the pores and promoting the KOH-carbon reaction (R. Wang et al., 2012). EDX analysis of PKS-AC, as depicted in Figure 4.7, demonstrated that the majority of impurities had been washed out, leaving primarily carbon elements in PKS-AC. However, some trace elements were detected, likely due to the KOH activation process (Pu et al., 2021). In summary, PKS-AC and PKS-Char differed in their surface morphology and chemical composition. PKS-AC displayed irregular and heterogeneous surfaces meanwhile PKS-Char lacked the enhanced surface area and oxygen-containing groups present in PKS-AC, making the latter more suitable for applications requiring high surface activity and functional groups.

4.1.2.3 PKS-AC-MgO

PKS-AC-MgO in Figure 4.8 exhibits a more well-formed structure with meso/micro pores, due to the synergistic effect of KOH activation and MgO impregnation (Creamer et al., 2018).

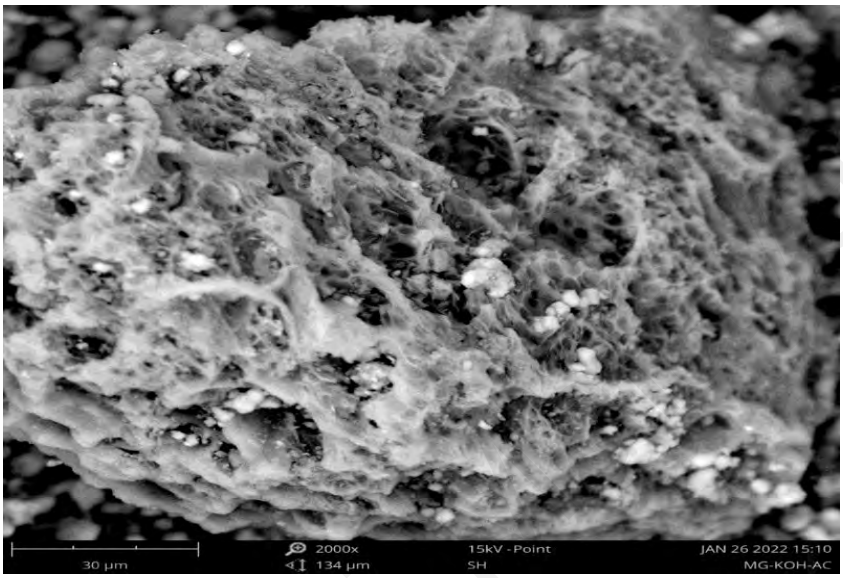

Figure 4.8: The surface morphology of PKS-AC-MgO under magnification of 2000x

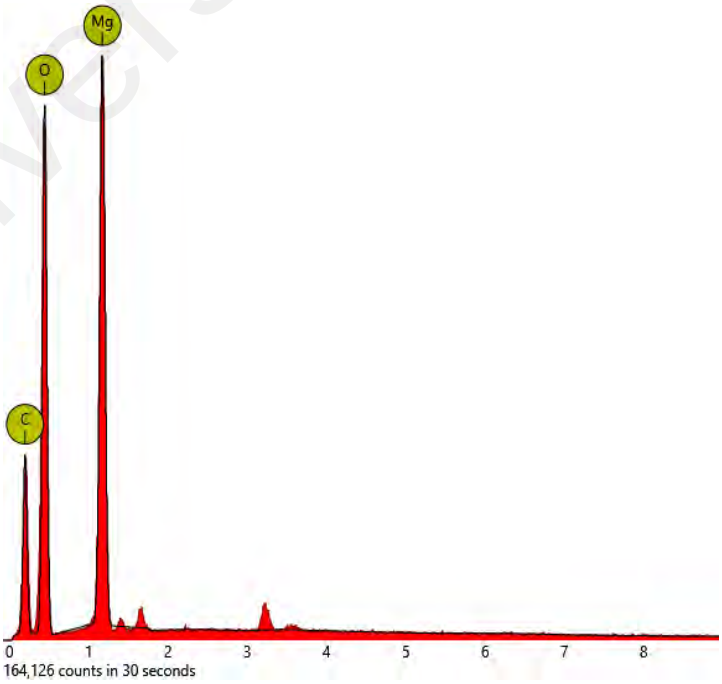

Figure 4.9: The composition of PKS-AC-MgO under EDX analysis

The impregnation of MgO further expanded the existing pores, particularly the mesopores, and introduced new pores, increasing the overall porosity of PKS-AC-MgO (Duran-Jimenez et al., 2021). While both PKS-AC and PKS-AC-MgO possessed well-developed porous structures, the pores in PKS-AC-MgO appeared somewhat blocked, likely due to the MgO modification process (Y. Li et al., 2013). This indicated the importance of the KOH activation step in opening up pores for efficient CO_2 adsorption (Birgani et al., 2016). The EDX analysis in Figure 4.9 confirms the elemental composition of PKS-AC-MgO, with the presence 25 % carbon (C), 51 % oxygen (O), and 24 % magnesium (Mg). The oxygen is attributed to the presence of oxygen-containing functional groups like hydroxyl and carboxyl groups, and it may also result from the MgO impregnation process. The presence of Mg indicates the successful impregnation of magnesium oxide particles onto PKS-AC-MgO, giving it acid-base properties that enhance its ability to adsorb molecules such as CO_2 (Siriwardane et al., 2017).

Overall, the SEM images and EDX analysis suggested that PKS-AC-MgO possessed a well-developed porous structure with enhanced adsorption potential. The combination of KOH activation and MgO impregnation played a crucial role in developing the porous surface, making PKS-AC-MgO a potential candidate for CO_2 adsorption applications (Rodgers, Healy, & Mulqueen, 2005).

4.1.3 Functional Group Analysis

4.1.3.1 PKS-Char

PKS-Char sample, as depicted in Figure 4.10, reveals distinct peaks corresponding to various functional groups. Narrow, short peaks observed at 3747 cm^{-1} and 3619 cm^{-1} indicated the presence of O-H (alcohol) groups in the sample groups which was due to the carbohydrates present in it (Wibawa, Nur, Asy'ari, & Nur, 2020). Additionally, a broad peak was detected at 1924 cm^{-1} , 1530 cm^{-1} , 1780 cm^{-1} , and 3747 cm^{-1} , which

could be attributed to C-N stretching, N-H in-plane deformation, N-H and/or-OH stretching, and N-O nitro compound groups or C=N functional groups (Inagaki, Toyoda, Soneda, & Morishita, 2018).

These bonds were formed during the pyrolysis of PKS-Char in the presence of nitrogen flow, leading to the introduction of nitrogen-containing functional groups. This incorporation of N-containing groups enhanced the adsorption performance of PKS-Char, increasing its affinity for adsorbates (Shi & Liu, 2021). Additionally, peaks observed at the fingerprint region of 919 cm^{-1} indicated various types of CCCC stretching. The presence of multiple bands in this spectral range was expected due to the involvement of different combinations of carbon atoms in the vibrations (Z. Guo, Xiong, Sohail, & Yang, 2021). In conclusion, the spectral analysis of PKS-Char revealed the presence of O-H (alcohol) groups and various nitrogen-containing functional groups formed during the pyrolysis process. These functional groups contributed to the enhanced adsorption performance of PKS-Char, making it a promising adsorbent for adsorption applications. The presence of multiple bands in the fingerprint region further illustrated the diverse carbon atom combinations present in PKS-Char's structure.

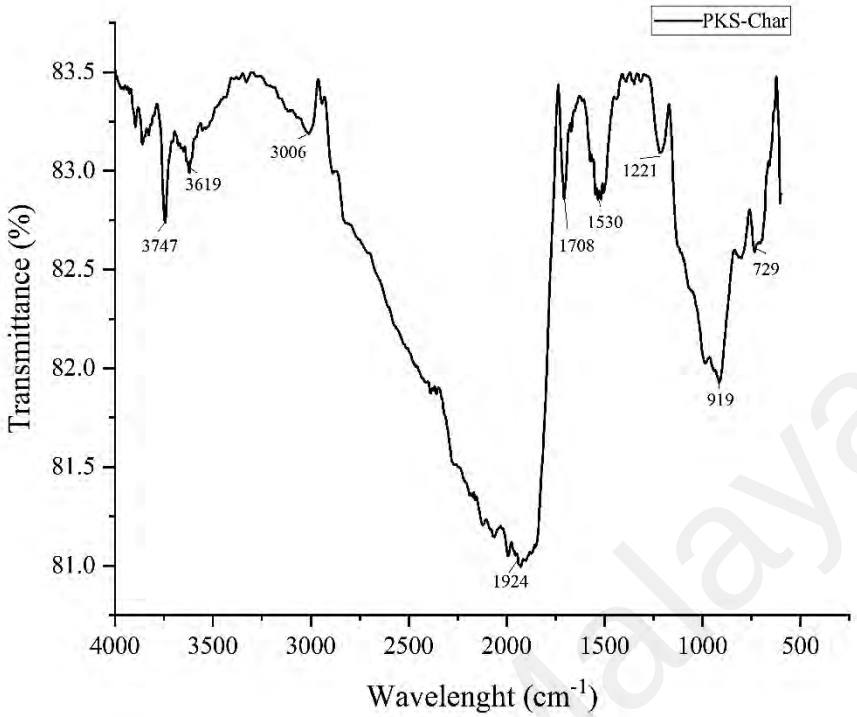

Figure 4.10: FTIR spectrum of PKS-Char

4.1.3.2 PKS-AC

The analysis of both PKS-Char and PKS-AC spectra showed similarities above 1500 cm^{-1}, indicating the presence of similar functional groups in both materials. However, notable changes occurred in the fingerprint region below 1500 cm^{-1}, primarily attributed to the KOH activation process undergone by PKS-AC. After activation, PKS-AC exhibited the formation of two new bands compared to PKS-Char, indicating an increase in oxygen functional groups, particularly phenolic groups. Peaks at 3541 $cm^{-1}$and 3010 cm^{-1} suggested the presence of C-H groups in PKS-AC (Figure 4.11). Additionally, peaks at 2315 cm^{-1}, 2090 cm^{-1}, and 1897 cm^{-1} were observed, indicating the presence of nitrile functional groups (C≡N) and weak triple C bonds (C≡C) which arise from the breakdown and rearrangement of compounds during KOH activation at 850°C (L. Zhao et al., 2010).

KOH activation had resulted in numerous new O-containing functional groups, such as CO, OH, CO, OCO, and COOH groups (Chen et al., 2020). The reaction between KOH and PKS-Char during the activation process, described by Equation 4.2 introduced significant voids in PKS-AC which were rapidly filled with OH- ions from KOH. PKS-AC exhibited peak between 1700 cm^{-1} and 1490 cm^{-1} resulting from C=C symmetrical stretching of pyrone groups and C=O of carboxylic groups, which formed from the rearrangement of phenolic compounds, and their presence was indicative of the complex chemical transformations occurring during KOH activation (Matos, Nahas, Rojas, & Rosales, 2011). Moreover, carbon atomic vibrations were also detected where the peak at 915 cm^{-1} was observed and this showed the presence of C–C and C–N stretching from quinazoline ring or NO_2 stretching (Z. Guo et al., 2021).

$$6KOH + 2C \leftrightarrow 2K + 3H_2 + 2K_2CO_3 \quad (4.2)$$

In summary, while both PKS-Char and PKS-AC shared some common functional groups, the KOH activation process significantly altered the spectrum of PKS-AC, leading to the introduction of new functional groups, including phenolic and nitrile groups. These modifications enhanced the adsorption properties of PKS-AC, making it a promising material for various adsorption applications.

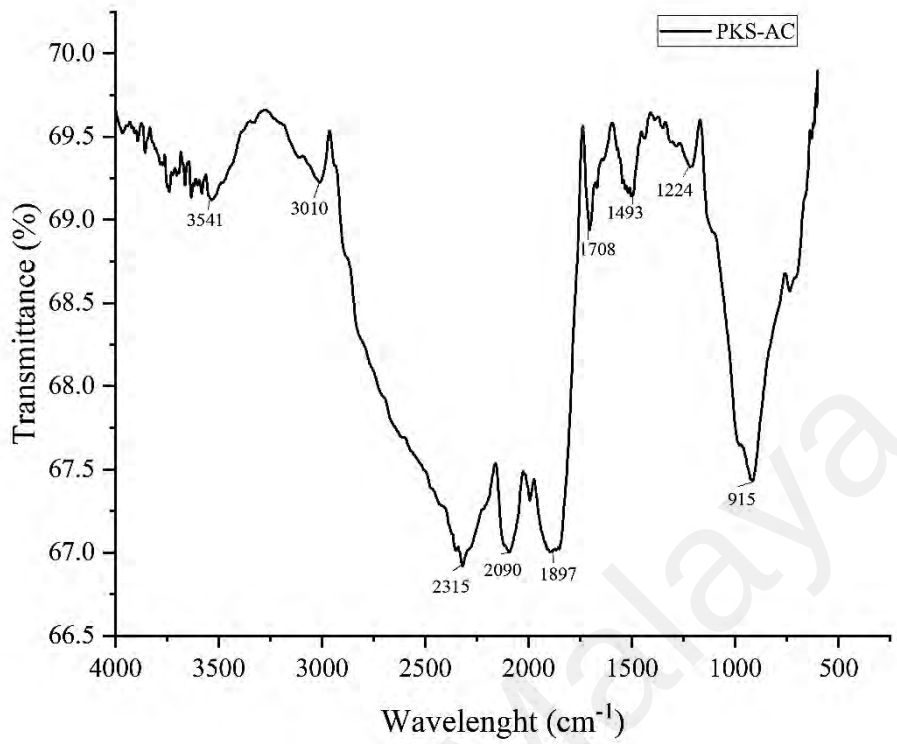

Figure 4.11: FTIR spectrum of PKS-AC

4.1.3.3 PKS-AC-MgO

In contrast, the FTIR result of PKS-AC-MgO was in tally with thermogravimetric analysis (Figure 4.12) showing loss of moisture and other volatile compounds followed by two endothermic peak exhibited different peaks. There is loss in some functional group such as C≡N, C=C and decrease in C-O in the plot obtained for PKS-AC-MgO as compared to PKS-AC and PKS-Char.

A sharp band observed at 3696 cm^{-1} attributing to the oxygen-containing functional groups O–H stretch in alcohols, phenols, and OH stretching which is also means that $Mg(OH)_2$ is present on PKS-AC-MgO and the peak at 1408 cm^{-1} attributes to the C-O stretching vibration (Wibawa et al., 2020). The region under 1000 cm^{-1} may be used to rapidly locate peaks in a MgO matrix (L. Zhao et al., 2010) whereas, the

transmittance band at 861 cm^{-1} is assigned to a series of transitions that involve Mg-O-Mg and a peak is formed at 617 cm^{-1} shows the Mg-O bond stretching metal oxygen bonding vibration (W. Gao et al., 2018). Similarly, in the investigation by (Tahir, Sillanpaa, Almutairi, Mohammed, & Ali, 2023) a comparable outcome was observed, where the existence of the Mg-O-Mg bond in the AC/MgO photocatalyst was identified by a broad peak ranging from 777 cm^{-1} to 501 cm^{-1}. In overall there were only two long sharp peaks and three small broad peaks were found in Figure 4.12 for PKS-AC-MgO, indicating that the most functional category of non-carbon elements were lost after carbonization and formation of five bands in PKS-AC-MgO indicated that the AC was a simple organic compound with small mass molecular weight (L. Zhao et al., 2010).

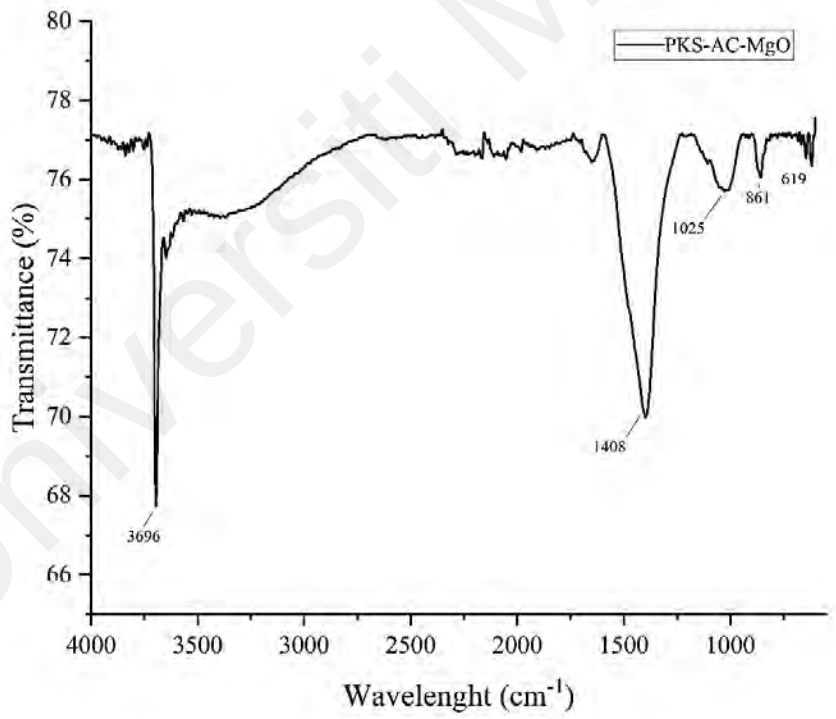

Figure 4.12: FTIR spectrum of PKS-AC-MgO

In summary the FTIR analysis indicated that PKS-AC-MgO had undergone significant changes in functional groups compared to PKS-Char and PKS-AC. The introduction of MgO on the surface of PKS-AC led to the formation of new peaks and the loss of certain functional groups. PKS-AC-MgO displayed a distinct spectral pattern, suggesting its unique composition and potential for specific applications, such as photocatalysis and adsorption.

4.1.4 Crystallographic Structure Analysis

4.1.4.1 PKS-Char

The X-ray diffraction (XRD) analysis of PKS-Char (Figure 4.13) revealed the presence of only two broad peaks around $2\theta = 24°$ and 43°, corresponding to the diffraction of (002) and (100) crystal planes, respectively. The appearance of the peak at around 24°, particularly at pyrolysis temperature of 700 °C, indicated an increase in the regularity of the crystalline structure, leading to improved layer alignment (Zamboni et al., 2016).

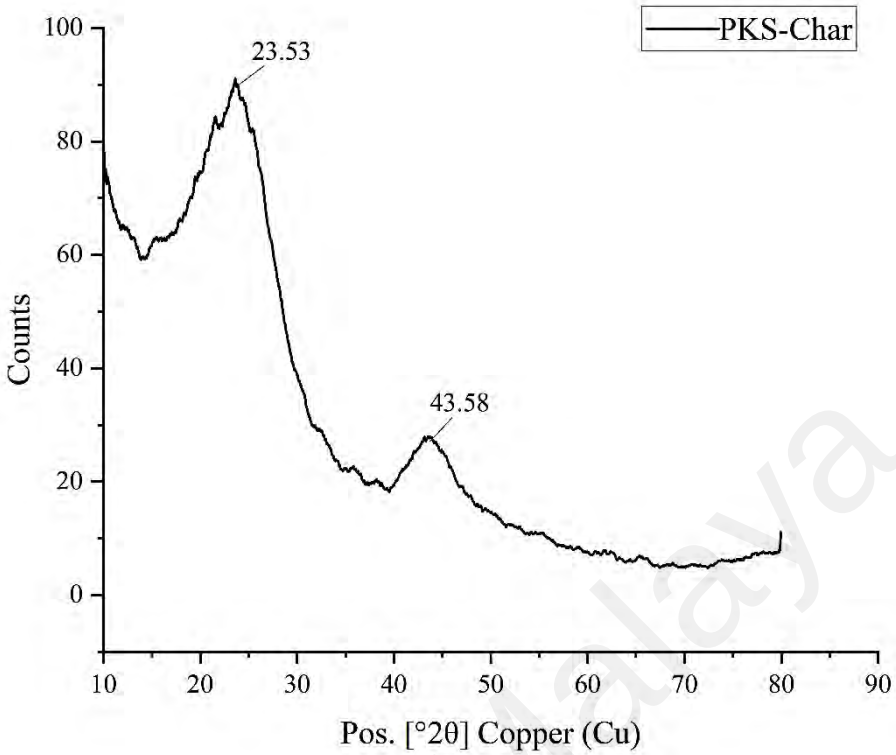

Figure 4.13: XRD Analysis of PKS-Char

The absence of extra peaks in the XRD spectrum showed the absence of any other x-ray traceable compounds PKS-Char. This suggested that the PKS-Char was primarily composed of carbon with a highly amorphous structure and did not contain any significant crystalline phases or impurities due to the natural composition and arrangement of the organic molecules of the PKS biomass structure that was lacked in well-defined crystalline regions. Furthermore, as the pyrolysis process was carried out at higher temperature of 700°C, this could lead to the removal of volatile components and the rearrangement of carbon atoms, which could result in breakdown of crystalline structures and promote the formation of amorphous carbon structures in PKS-Char.

4.1.4.2 PKS-AC

The XRD analysis of PKS-AC exhibited similar patterns with PKS-Char, showing the presence of only two broad peaks at around 2θ = 24° and 43°, corresponding to the diffraction of (002) and (100) crystal planes, respectively (Figure 4.13 and Figure 4.14).

This was due to the KOH activation at 850℃, caused chemical and physical changes to PKS-AC and break down crystalline structures, resulting in the formation of amorphous carbon structures which was in consistent with other carbonaceous material (Birgani et al., 2016). Moreover, KOH also has tendency to react with various components present in PKS-biomass, leading to the removal of volatile components, the creation of pores, and the development of new chemical species which led to the disruption of existing crystalline structures and contributed to the formation of amorphous carbon (Creamer et al., 2018). Both the PKS-Char and PKS-AC exhibited the crystalline structure of monoclinic and orthorhombic which had unequal lattice parameters and could also display anisotropic properties. This varying lattice parameters could result in diverse surface sites and potential for selective adsorption (Basheer et al., 2021).

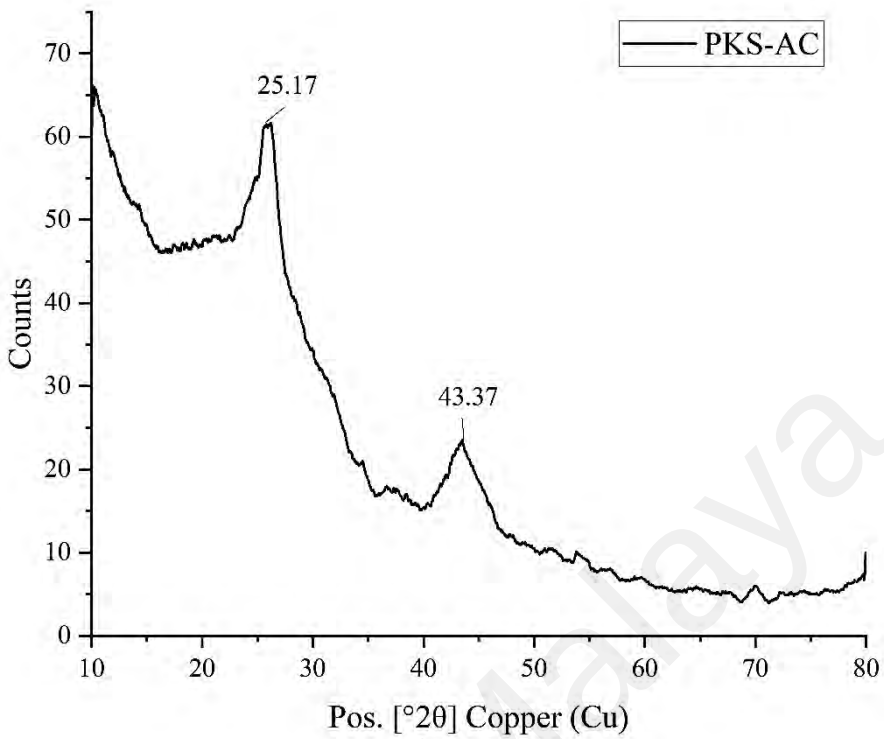

Figure 4.14: XRD Analysis of PKS-AC

In summary, the combined effects of KOH chemical reactions, pore development, high surface area, and the disruption of crystalline structures contributed to the amorphous nature of the PKS-AC. The similarity in XRD pattern of PKS-AC and PKS-Char suggested that both materials possessed well-defined carbon matrices suitable for their applications as carbonaceous adsorbents.

4.1.4.3 PKS-AC-MgO

XRD result of PKS-AC-MgO (Figure 4.15) revealed the presence of five well-defined peaks at 18.42º, 37.98º, 50.81º, 58.79º, and 62.02º, corresponding to the hexagonal crystal structure. The presence of these peaks attributed to the interactions between MgO and the PKS carbon structure during the impregnation and activation processes indicated the successful impregnation of magnesium oxide (MgO) on PKS-AC-MgO.

MgO is known for its catalytic and adsorptive properties and the impregnation of MgO on the surface of PKS-AC-MgO resulted in interaction with PKS-carbon structure. This reaction had led to physical and chemical interaction leading to a well-defined crystalline structure. Furthermore, the diffraction peaks at 37° (200) and 62° (220) correspond to the standard diffraction pattern of MgO, further confirming the presence of MgO in the material (Vall, Hultberg, Strømme, & Cheung, 2019). This shows that the impregnation of MgO had resulted in sharp peak points due to the sharp edges of the oxide particles. Similarly the study by (Tahir et al., 2023) it was observed that the interplanar spacing and diffraction pattern of the material closely corresponded with the standard diffraction pattern of MgO.

In summary, the combination of MgO impregnation and KOH activation in PKS-AC-MgO could lead to the development of crystalline structures due to the interactions, catalytic effects, and impregnation influences of MgO on the carbon structure during the activation process. PKS-AC-MgO exhibited well-formed hexagonal crystal particles which had close-packed layers of atoms, potentially leading to a higher surface area and more accessible adsorption sites (Duran-Jimenez et al., 2021). The crystallite size of PKS-AC-MgO was determined to be 9.41 nm, confirming the good crystalline structure of the PKS-AC-MgO. Overall, the XRD analysis provided valuable information about the crystallographic structure and their suitability for specific CO_2 adsorption applications.

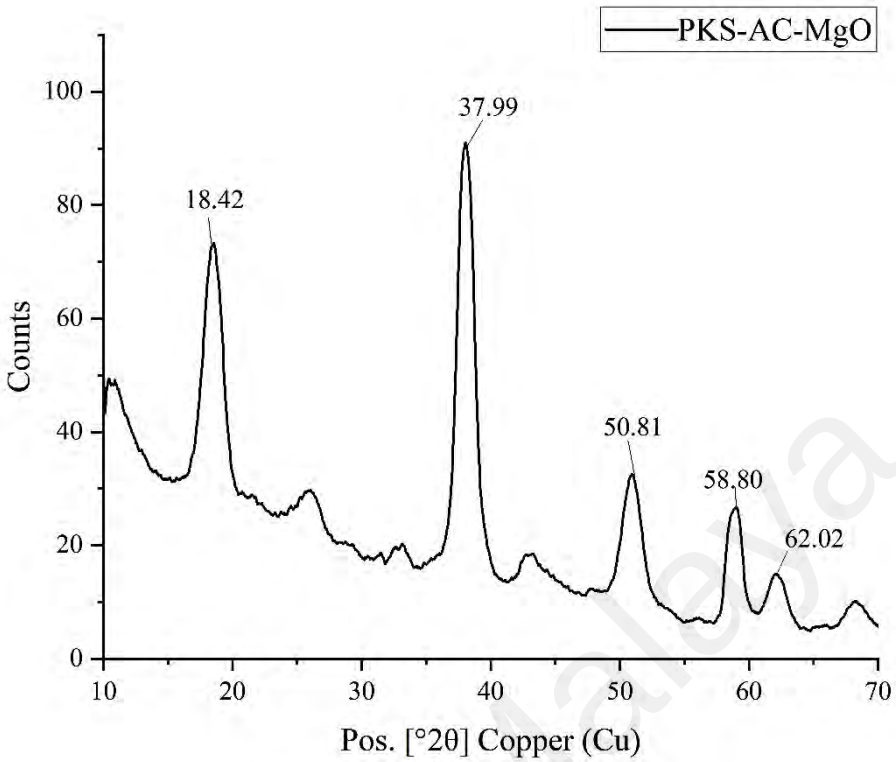

Figure 4.15: XRD Analysis of PKS-AC-MgO

4.1.5 Surface Area Analysis

4.1.5.1 PKS-Char

According to the International Union of Pure and Applied Chemistry (IUPAC) classification, the surface area analysis of PKS-Char (Figure 4.16) revealed a mix of Types III and IV physisorption isotherm curves. Type III is characterized by a gradual increase in adsorption with relative pressure. This typically indicates PKS-Char with mesoporous structures, where pores have a broad size distribution. The adsorption begins at a lower relative pressure and gradually rises, suggesting that the PKS-Char had a limited number of small pores. This isotherm indicates that PKS-Char with a wide range of pore sizes and can be associated with irregular pore structures.

Meanwhile, Type IV isotherm exhibits a steep increase in adsorption at higher relative pressures forming an "unclosed hysteresis loop" phenomenon in PKS-Char

indicates the presence of mesopores or macropores, and often suggests a more complex pore structure. An unclosed hysteresis loop observed in the adsorption-desorption isotherm of PKS-Char also can be due to the capillary condensation occurring in interconnected pores, which are often found in aggregates of particles with slit-like pores (Goel et al., 2021).

Surface area analysis revealed that PKS-Char had a BET surface area of 435 m^2/g, which was significantly higher than the surface area of raw palm kernel shell without any activation or modification (0.793 m^2/g) (Gayathiri et al., 2022). The Langmuir surface area, indicating monolayer surface coverage, showed a slightly increased value of 490 m^2/g for PKS-Char. This reading was higher compared to KOH activated garlic peel based adsorbent 262 m^2/g and also nitric acid activated walnut shell-based AC 418 m^2/g (Duan et al., 2017; G.-g. Huang et al., 2019). This indicates that PKS-Char had a higher surface area compared to other unmodified biomass-based adsorbents found in the literature (J. Chen et al., 2016).

A high pore volume indicates that the AC had a substantial amount of pore space, which is important for adsorption capacity. Therefore, the pore volume of PKS-Char was 0.231 cm^3/g, suggested that for every gram of PKS-Char, there was a volume of pores that occupied 0.231 cm^3. The pore diameter of PKS-Char was 2.1 nm indicated the average size of the pores falls within the mesopore range. Overall, the combination of a high BET surface area, Langmuir surface area, a high pore volume and a mesopore diameter of 2.1 nm indicated that the PKS-Char had a significant amount of relatively larger pores, which could be advantageous for various applications such as environmental remediation, water purification, and gas adsorption.

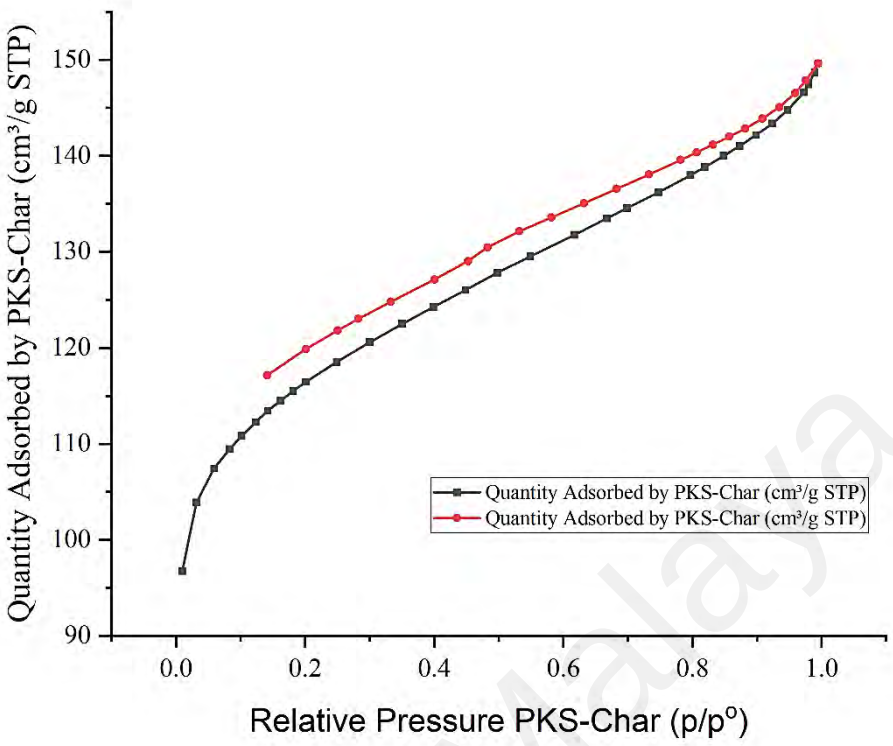

Figure 4.16: Nitrogen adsorption-desorption isotherm at 77K of PKS-Char

4.1.5.2 PKS-AC

The surface area analysis of PKS-AC revealed Types II and IV physisorption isotherm curves (Figure 4.17). The Type II isotherm shows a sharp initial rise in adsorption with relatively low relative pressure, indicating adsorption primarily onto a monolayer on the surface. This isotherm type suggests the presence of slit-shaped pores indicates a PKS-AC with relatively uniform and well-defined pores. As the N_2 molecules enter these pores, they form a condensed monolayer, resulting in the characteristic loop during desorption.

Type IV shows a rapid adsorption increase at lower relative pressures, indicating the presence of mesopores. This isotherm often points to materials with a combination of micro- and mesopores, typically in the range of 2 to 50 nm in diameter (Danish et al., 2021). The presence of both Type II and Type IV isotherms in the analysis of PKS-AC suggested a diverse pore structure that included micropores and mesopores. This is

consistent with the activation process involving KOH, which can lead to the creation of a wide range of pore sizes. The Type II isotherm indicates that the PKS-AC had well-defined micropores, while the Type IV isotherm reflects the presence of mesopores. These pores contribute to a high surface area and adsorption capacity. The KOH activation process likely generates both micro- and mesopores by creating voids and channels within the PKS-AC, leading to the observed isotherm behavior.

The BET surface area of PKS-AC is 1086 m^2/g, significantly higher than other biomass-based adsorbents like KOH-activated pine wood (980 m^2/g) and KOH-activated pomegranate peels (585 m^2/g). The KOH activation process contributed to the increased surface area and pore volume of PKS-AC, which reached 0.58 cm^3/g. However, the pore diameter remained unchanged at 2.1 nm due to the KOH activation process, which led to the removal of volatile components, carbonization of the PKS, and the formation of voids and pores. As a result, new pores were developed, leading to an increase in surface area and pore volume while preserving the fundamental structural characteristics of the original pores (Hurley, Li, & Xu, 2010). The findings from the surface area analysis were consistent with the SEM analysis, which revealed that PKS-AC exhibited significantly greater textural porosity compared to the parent material (Yuan et al., 2021). In summary, the KOH activation process had resulted in a notable increase in surface area and pore volume, signifying the successful creation of a highly porous structure than those of PKS-Char, highlighting the improved adsorption capacity and the potential utility of PKS-AC as an effective adsorbent.

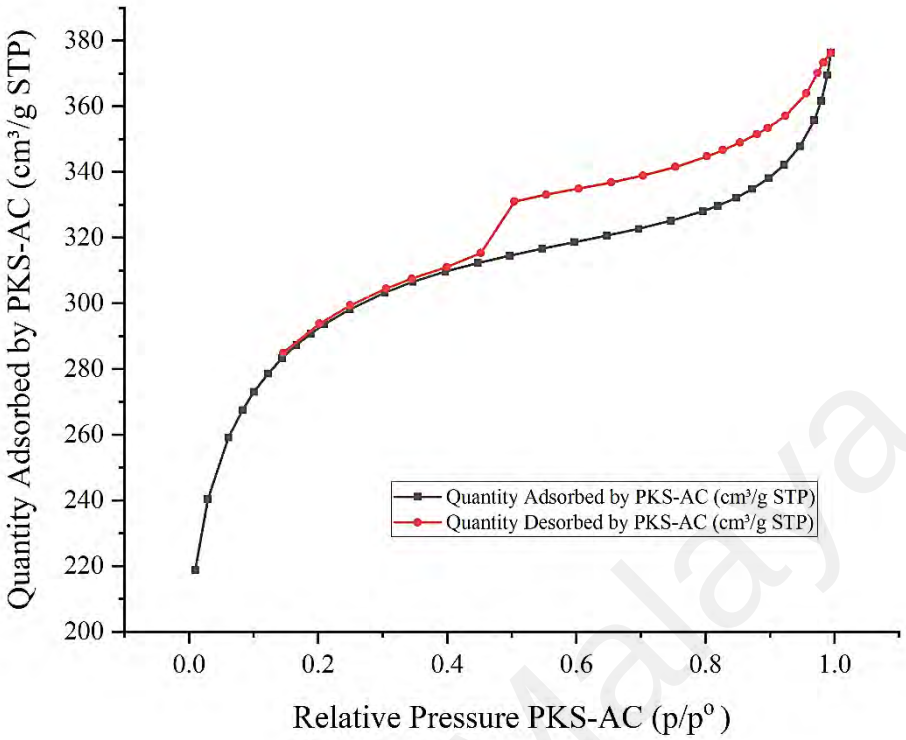

Figure 4.17: Nitrogen adsorption-desorption isotherm at 77K of PKS-AC

4.1.5.3 PKS-AC-MgO

PKS-AC-MgO (Figure 4.18) revealed Types II and IV physisorption isotherm curves which was similar to PKS-AC. The Type II isotherm suggests the existence of microporous features with pore diameters less than 2 nm, while Type IV indicates a mesoporous structure. The hysteresis loop's shape is correlated with the pore morphologies of the adsorbents, and PKS-AC-MgO demonstrates a porous material with hysteresis loop patterns closely resembling those of porous materials like AC and metal organic frameworks (MOFs) (Danish et al., 2021).

Compared to PKS-AC, there was a significant drop in surface are of PKS-AC-MgO; BET surface area (Table 4.1) of 431 m^2/g and a Langmuir surface area of 471 m^2/g could be attributed to the introduction of MgO onto the surface of the PKS-AC-MgO. The impregnation of MgO could lead to changes in the pore structure and surface

characteristics of the adsorbent, which in turn affected the surface area measurements. The impregnation of MgO onto the PKS-AC-MgO could potentially block or partially filled some of the pores which could reduce the overall available surface area for adsorption, leading to a decrease in measured surface area (Alkadhem, Elgzoly, Alshami, & Onaizi, 2021). However, the obtained surface area of PKS-AC-MgO is still comparatively greater than other adsorbents used for CO_2 adsorption in the literature as discussed in subtopic 4.10.

Despite, the reduction in surface area PKS-AC-MgO obtained higher pore volume of 0.294 cm^3/g compared to PKS-Char. This was due the addition of MgO which could lead to the creation of additional pores and voids within the PKS-AC-MgO. These newly formed pores, combined with the existing pore structure of PKS-AC, contributed to the higher pore volume observed in PKS-AC-MgO. Moreover, the pore diameter of PKS-AC-MgO was also higher 0.28 nm compared to PKS-AC- and PKS-Char which could be due to pore widening of existing pores caused by impregnation of MgO (W. Gao et al., 2018). The higher pore volume and larger pore diameter in PKS-AC-MgO compared to PKS-AC and PKS-biochar could be attributed to the introduction of MgO, which could result in the creation of new pores, widening of existing pores, changes in pore interconnectivity, and alterations in the overall porous structure. These modifications highlighted the potential impact of MgO on the development of porous materials for CO_2 adsorption applications.

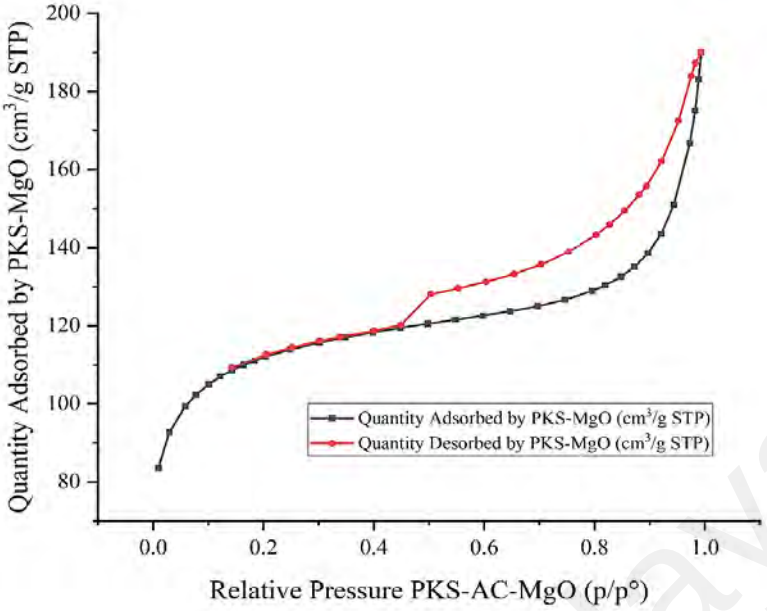

Figure 4.18: Nitrogen adsorption-desorption isotherm at 77K of PKS-AC-MgO.

Non-local density functional theory (NLDFT) is a theoretical framework used to simulate and analyze the pore structure of porous materials which builds upon classical density functional theory (DFT) by accounting for non-local effects, which are important in systems with long-range interactions and complex geometries, such as porous materials such as PKS-adsorbents in this study (Baby, Hussein, Zainal, & Abdullah, 2023). NLDFT simulations are typically more accurate for materials with well-defined and predominant pore sizes within the mesopore or micropore ranges (Gil & Grange, 1996). Out of the three synthesized adsorbents, only PKS-AC-MgO successfully obtained the PSD values. The other two adsorbents may exhibit a wide distribution of pore sizes or lacks distinct pore features.

The nitrogen isotherms exhibit a prominent peak (Figure 4.21) at around 5 nm, which corresponded to the mesoporous channels created by the elimination of non-carbon material by carbonization (He, Mei, Bao, & Wilcox, 2014). The cumulative surface area (Figure 4.19) represented the total surface area of the PKS-AC-MgO available for

adsorption. The value of 21.313 m^2/g indicated that for every gram of the PKS-AC-MgO, there was a substantial surface area available for gas molecules, including CO_2, to adsorb onto. A higher surface area generally corresponds to more adsorption sites, enhancing the PKS-AC-MgO's capacity to capture gas molecules (C. Wu et al., 2013). Meanwhile, the cumulative pore volume (Figure 4.20) represented the total volume of pores within the PKS-AC-MgO available for gas adsorption. A higher cumulative pore volume indicated a greater volume of interconnected pores that could accommodate gas molecules. The value of 0.27109 cm^3/g suggests that the PKS-AC-MgO possessed a significant porosity, enabling the accommodation of a substantial amount of gas, such as CO_2 (Gil & Grange, 1996).

Overall, the combination of a substantial cumulative surface area and a significant cumulative pore volume in PKS-AC-MgO demonstrated its superior adsorption properties for CO_2. These factors collectively boosted the PKS-AC-MgO's CO_2 adsorption behavior, making it a promising candidate for applications in carbon capture and other environmentally relevant processes.

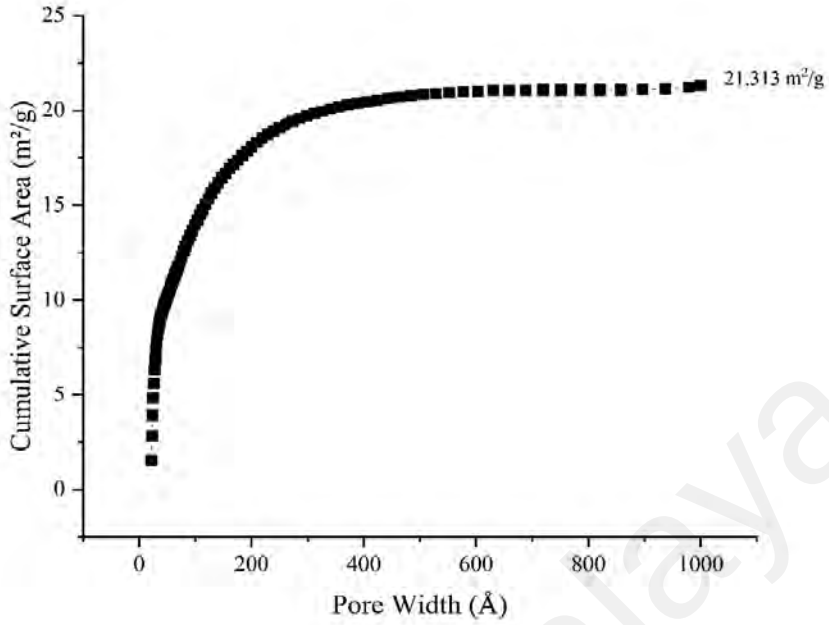

Figure 4.19: Non-Local Density Functional Theory (NLDFT) simulation of pore structure (Cumulative - Surface Area) (PKS-AC-MgO)

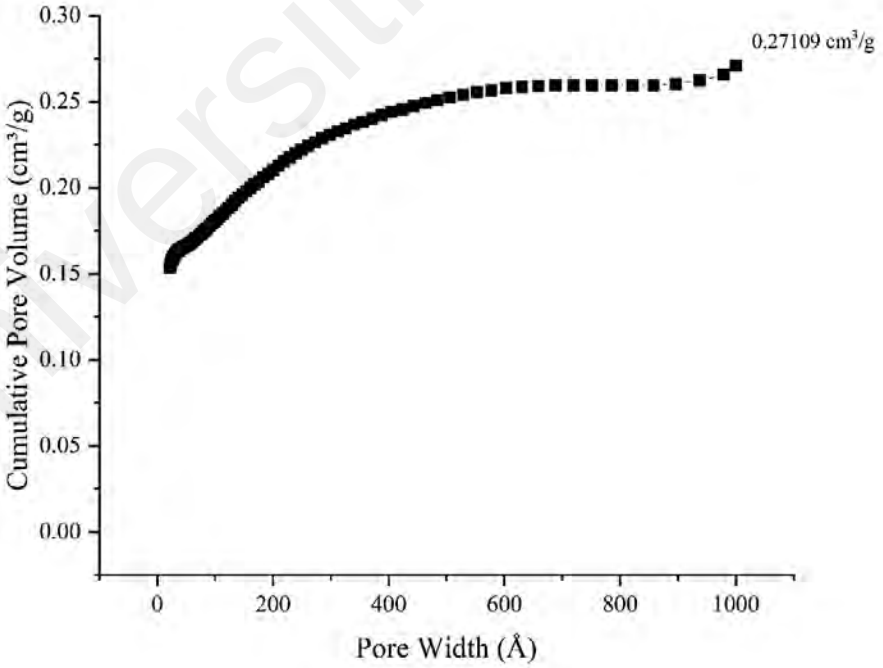

Figure 4.20: Non-Local Density Functional Theory (NLDFT) simulation of pore structure (Cumulative – Pore Volume) (PKS-AC-MgO)

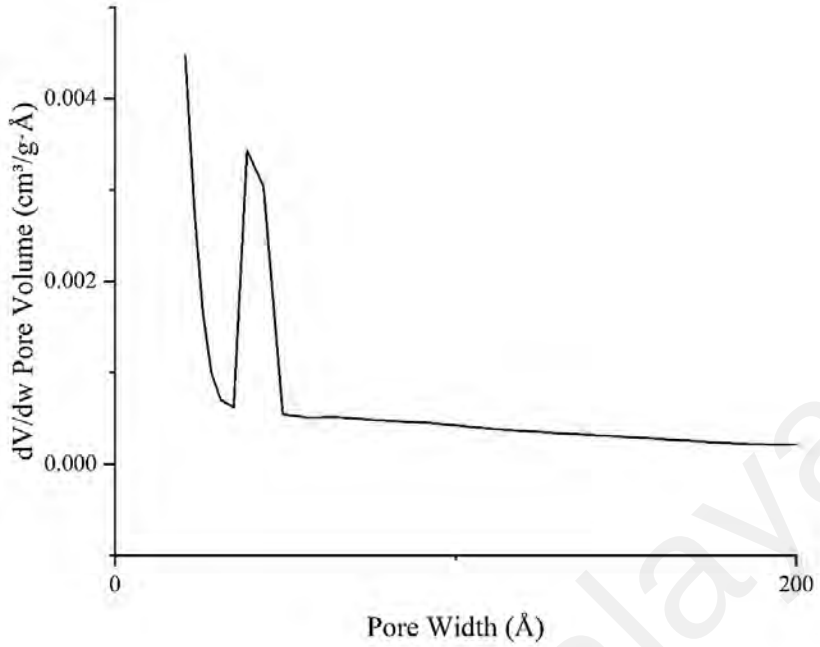

Figure 4.21: BJH dv/dw pore volume vs pore width (PKS-AC-MgO)

Table 4.1: Surface area properties of PKS-Char, PKS-AC and PKS-AC-MgO

Sample	BET Surface Area (m^2/g)	Langmuir Surface Area (m^2/g)	Pore Volume (cm^3/g)	Pore Diameter (nm)
PKS-Char	435	490	0.231	2.1
PKS-AC	1086	1224	0.582	2.1
PKS-AC-MgO	418	471	0.294	2.8

4.2 CO_2 Adsorption Performance of PKS-Char

Table 4.2, shows the result obtained from the set of experimental design suggested by RSM- CCD for the adsorption using PKS-Char. A total of 9 experiments have been conducted at operating conditions of temperature (25℃ -75℃) and pressure (1 bar- 5 bar). Figure 4.22 reveals that the adsorption of CO_2 onto PKS-Char increased as the temperature decreased and the pressure increased. PKS-Char also exhibited a higher CO_2

adsorption capacity of 3.13 mmol/g at 25℃ and 5 bar. At the constant pressure of 5 bar, the adsorption capacity decreased by 18.15% (2.57 mmol/g) when the temperature increased from 25℃ to 50℃, and by 20.6% (2.04 mmol/g) when the temperature increased from 50℃ to 75℃.

Table 4.2: Experimental design suggested by RSM, and the result obtained on CO_2 adsorption capacity for PKS-Char.

Run	Temperature (℃)	Pressure (Bar)	Adsorption Capacity (mmol/g)
1	25.00	5.00	3.14
2	50.00	3.00	2.15
3	85.36	3.00	1.10
4	75.00	1.00	0.50
5	75.00	5.00	2.04
6	25.00	1.00	1.05
7	50.00	0.17	0.45
8	14.64	3.00	2.75
9	50.00	5.83	2.65

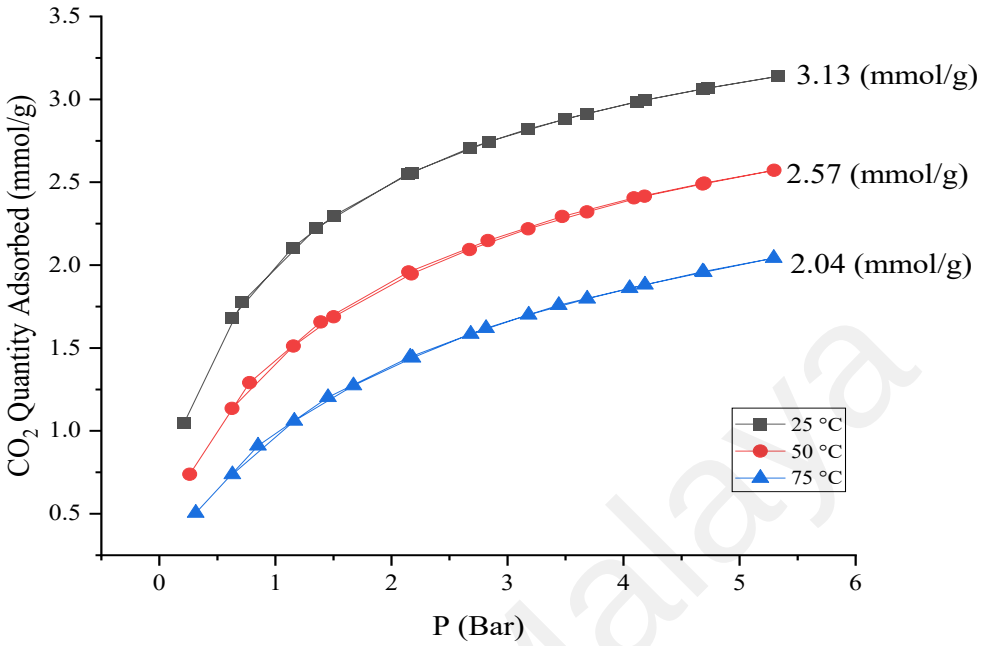

Figure 4.22: Experimental adsorption and desorption isotherm of CO_2 on PKS-Char at 25°C, 50°C and 75°C

Table 4.3: ANOVA analysis of the CCD for CO_2 Adsorption Capacity on PKS-Char

Source	**Sum of Squares**	**df**	**Mean Square**	**F-value**	**p-value**
Model	8.480	5	1.700	121.0	< 0.0001
A-Temperature	1.980	1	1.980	141.6	< 0.0001
B-Pressure	5.680	1	5.68	405.5	< 0.0001
AB	0.0756	1	0.0756	5.400	0.0531
A^2	0.1109	1	0.1109	7.910	0.0260
B^2	0.6848	1	0.6848	48.88	0.0002
R^2	0.9886				
Adjusted R^2	0.9804				
Predicted R^2	0.9187				
Adeq Precision	35.53				

From the hypothesis generated by ANOVA for PKS-Char (Table 4.3) reveals that the Model F-value of 121 indicates models are statistically significant. Terms of A, B, A^2, and B^2 exhibit significance with p-values less than 0.0500. Additionally, the modified R^2 value of 0.9804 closely aligns with the expected R^2 value of 0.9187 indicating a good agreement with the suggested model fits the data well. Equation 4.3 shows the regression equation describing the relationship between the variable equation representing the developed model of PKS-Char.

$$CO_2\ A\ dsorption_{PKS-Char} = 2.15 - 0.4979A + 0.8427B - 0.1375AB + 0.1262A^2 - 0.3138B^2 \quad (4.3)$$

The correlation between the operating parameters and CO_2 adsorption capacity was successfully demonstrated by the close agreement between theoretical (predicted) and experimental (actual) values, as depicted in Appendix B. The perturbation graph of PKS-Char revealed a steeper slope for the parameter B (operating pressure), indicating that changes in pressure had a greater impact on CO_2 adsorption capacity compared to temperature (parameter A). In summary, PKS-Char exhibited successful CO_2 adsorption across the range of tested temperatures and varied pressures. The adsorption capacity was observed to increase with increasing pressure, with the maximum capacity achieved at 25℃. The developed model effectively established the relationship between the operating parameters and CO_2 adsorption capacity.

4.3 CO_2 Adsorption Performance of PKS-AC

Table 4.4 presents the results obtained from conducting a set of experimental suggested by RSM-CCD. 9 runs of experiment were conducted for PKS-AC to investigate the effects of temperature (ranging from 25℃ to 75℃) and pressure (ranging from 1 bar to 5 bar) on CO_2 adsorption. Figure 4.23, illustrates that PKS-AC exhibited a higher

adsorption capacity of 3.40 mmol/g at 25℃. However, the adsorption capacity did not decrease constantly with increasing temperature. From 25℃ to 50℃, the adsorption capacity decreased by 47.7% (1.78 mmol/g), and from 50℃ to 75℃, it decreased by 20.8% (1.41 mmol/g). The significant drop in CO_2 adsorption capacity after 25℃ might be attributed to the instability of PKS-AC's structure at higher temperatures. SEM magnified images of PKS-AC (Figure 4.8) showed a multiple mesopores developed after activation using KOH, where the surface area of PKS-AC increased significantly after activation, which could render the structure more susceptible to temperature changes due to weaker intermolecular bonding within the carbon matrix (Abuelnoor et al., 2021). However, when compared to PKS-Char, PKS-AC exhibited an additional hike of 8% CO_2 adsorption at 25℃, attributed to the pore development resulting from KOH activation (Al Mesfer, 2020).

Table 4.4: Experimental design suggested by RSM, and the result obtained on CO_2 adsorption capacity for PKS-AC

Run	Temperature (℃)	Pressure (Bar)	Adsorption Capacity (mmol/g)
1	50.00	5.83	1.78
2	50.00	0.17	0.10
3	50.00	3.00	1.15
4	75.00	5.00	1.41
5	25.00	5.00	3.40
6	14.64	3.00	2.70
7	85.36	3.00	0.40
8	25.00	1.00	0.73
9	75.00	1.00	0.21

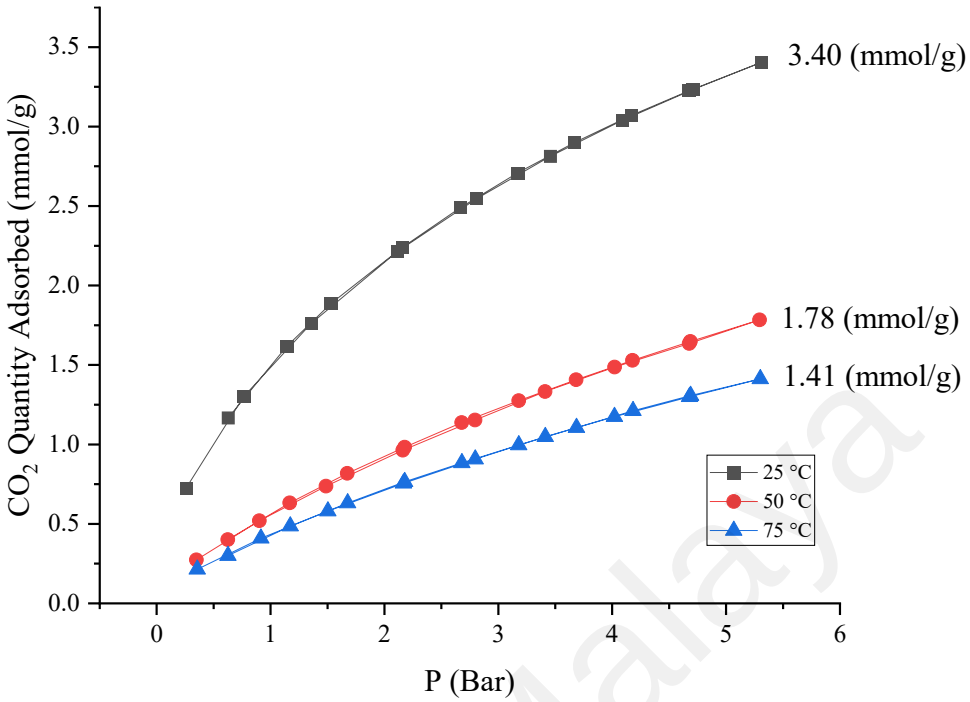

Figure 4.23: Experimental adsorption and desorption isotherm of CO_2 on PKS-AC at 25°C, 50°C and 75°C

Table 4.5: ANOVA analysis of CCD for CO_2 Adsorption Capacity on PKS-AC

Source	**Sum of Squares**	**df**	**Mean Square**	**F-value**	**p-value**
Model	9.57	3	3.190	31.65	< 0.0001
A-Temperature	4.15	1	4.150	41.20	0.0001
B-Pressure	4.88	1	4.880	48.40	< 0.0001
AB	0.5402	1	0.5402	5.360	0.0458
R^2	0.913				
Adjusted R^2	0.884				
Predicted R^2	0.722				
Adeq Precision	17.05				

The significance of the model is indicated by the F-value of 31.65 presented in Table 4.5, with model terms A, B, and AB being statistically significant, as their p-values are less than 0.0500. The adjusted R^2 value of 0.8846 closely approximates the predicted value of 0.7224. Equation 4.4 shows the regression equation describing the relationship between the variable equation representing the developed model of PKS-AC. This equation is valuable as it allows to make predictions about the dependent variable for given values of the independent variables. It provides a way to quantify and formalize relationships within the data and can be used for various purposes such as making forecasts, understanding cause-and-effect relationships, optimizing processes, and more.

$$\boldsymbol{CO_2\ Adsorption_{PKS-AC}} = \mathbf{1.27} - \mathbf{0.7203}\boldsymbol{A} + \mathbf{0.7807}\boldsymbol{B} - \mathbf{0.3675}\boldsymbol{AB} \quad (4.4)$$

The operating pressure (B) exhibits a significantly higher F-value of 48.40 compared to the operating temperature (A), indicating that operating pressure had a more pronounced influence on CO_2 adsorption capacity. Appendix B depicts the theoretical (predicted) versus experimental (actual) values of CO_2 adsorption, demonstrating the close agreement between the two sets of values and confirming the success of the developed model in establishing the correlation between the operating parameters and CO_2 adsorption capacity displays the perturbation plot with the reference point set at the centre of each parameter's range. The response is plotted against the deviation from the reference point achieved by altering the range of each individual factor reveals a steeper slope for parameter B (operating pressure), indicating that changes in pressure have a greater impact on CO_2 adsorption capacity compared to temperature (parameter A).

4.4 CO_2 Adsorption Performance of PKS-AC-MgO

Table 4.6, shows the result obtained from the set of experimental design and result obtained for the adsorption using PKS-AC-MgO at temperature (25℃ -75℃) and pressure (1 bar- 5 bar) for CO_2 adsorption have been investigated.

Table 4.6: Experimental design suggested by RSM, and the result obtained on CO_2 adsorption capacity for PKS-AC-MgO

Run	Temperature (℃)	Pressure (Bar)	Adsorption Capacity (mmol/g)
1	50.00	3.00	2.17
2	25.00	5.00	3.53
3	50.00	0.17	0.25
4	75.00	1.00	0.28
5	75.00	5.00	2.11
6	25.00	1.00	1.05
7	50.00	5.83	2.70
8	85.36	3.00	0.80
9	14.64	3.00	3.30

Figure 4.24 illustrates that PKS-AC-MgO exhibited a higher adsorption capacity of 3.53 mmol/g at 25℃. The adsorption capacity remained constant as the pressure increased from 1 bar to 5 bar. Moreover, a consistent decrease in adsorption capacity was observed as the temperature rose. Specifically, there was a 23.7% reduction in adsorption capacity from 25℃ to 50℃ and a further 21.5% reduction from 50℃ to 75℃. The consistent drop in adsorption capacity with increasing temperature suggested that PKS-AC-MgO remained stable within a wide temperature range. This stability was attributed to the thermally resistant textural morphology of PKS-AC-MgO, as supported by SEM analysis in Figure 4.10, which revealed well-developed pores that exhibited an orderly arrangement. The image showcased the presence of numerous distinct and interconnected pores distributed uniformly across the carbon matrix (Al Mesfer, 2020). These pores

demonstrated a consistent and organized structure throughout the PKS-AC-MgO. This intricated pore network played a vital role in enhancing the adsorption capacity (Abuelnoor et al., 2021).

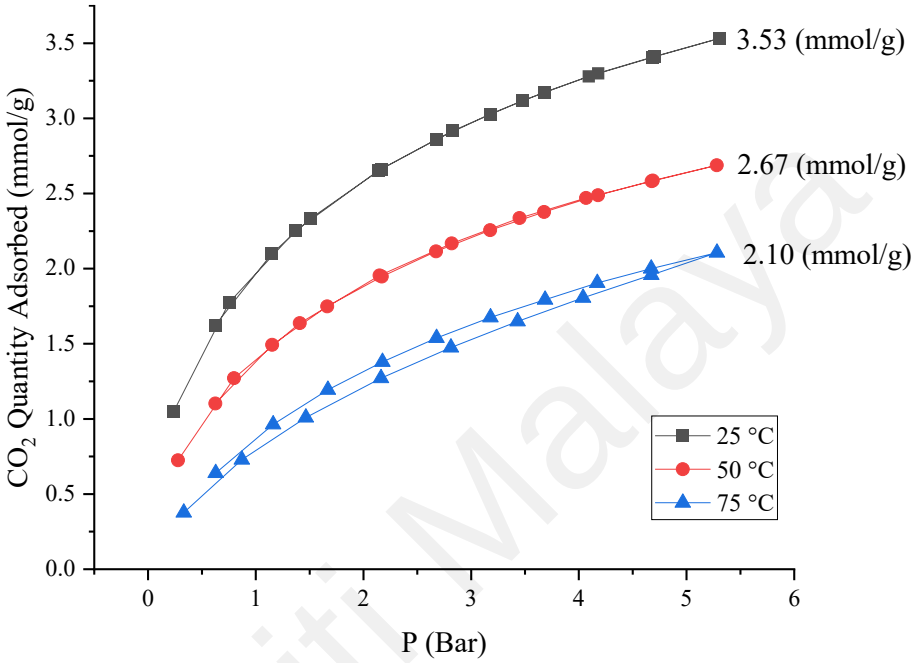

Figure 4.24: Experimental adsorption and desorption isotherm of CO_2 on PKS-AC-MgO at 25℃, 50℃ and 75℃

From the hypothesis generated by ANOVA (Table 4.7) the Model F-value is 55.87, it may conclude that the model is statistically significant. For this particular model, terms A, B, and B^2 are significant. The expected R^2 of 0.8262 and the adjusted R^2 of 0.9581 are in reasonable agreement. The developed model equation was established in the following Eq (4.5):

$$Adsorption_{PKS-KOH-MgO} = 2.17 - 0.7157A + 0.9719B - 0.1625AB - 0.0650A^2 - \ 0.3525\text{B}\text{\^{}}2 \quad (\mathbf{4.5})$$

Table 4.7: ANOVA analysis for the CCD for CO_2 Adsorption Capacity for PKS-AC-MgO

Source	Sum of Squares	df	Mean Square	F-value	p-value
Model	12.63	5	2.530	55.87	< 0.0001
A-Temperatures	4.100	1	4.100	90.66	< 0.0001
B-Pressure	7.560	1	7.560	167.17	< 0.0001
AB	0.1056	1	0.1056	2.340	0.1702
A^2	0.0294	1	0.0294	0.6503	0.4465
B^2	0.8644	1	0.8644	19.12	0.0033
R^2	0.9756				
Adjusted R^2	0.9581				
Predicted R^2	0.8262				
Adeq Precision	24.31				

The operating pressure (B) with F value of 167.17 was discovered to be a major factor in leaving an impact on CO_2 adsorption capacity. Followed by operating temperature (A). The theoretical (predicted) versus experimental (actual) values of the CO_2 adsorption are shown in Appendix D. The theoretical value was very close the experimental value which proved that developed model showed success in linking the correlation between the operating parameter and the CO_2 adsorption capacity. The perturbation plot and the reference point were adjusted at the centre of the range of each parameter. The response was plotted against the deviation from the reference point chosen by making some change in the range of every individual factor. The perturbation graph of PKS-AC-MgO shows a slope for parameter (B) and followed by (A) which implies the

response of CO_2 adsorption capacity is more susceptible of pressure changes followed by temperature.

4.5 Model Optimization of CO_2 Adsorption

The Design of Experiments (DOE) optimization and model validation process for CO_2 adsorption using PKS-Char, PKS-AC, and PKS-AC-MgO involved the analysis of three-dimensional response surface plots, as shown in Appendix C, E and G. Notably, all three adsorbents exhibited higher CO_2 adsorption capacities at lower temperatures, particularly at 25°C, and at higher pressures, specifically at 5 bar.

The presence of active nitrogen-containing pores within PKS-Char contributed to its enhanced performance (L. An et al., 2019). The optimized parameters for PKS-Char were identified at 61.2°C and 3.5 bar, resulting in a CO_2 adsorption capacity of 2.095 mmol/g. At this temperature, nitrogen-doped PKS-Char showcased improved CO_2 adsorption compared to undoped AC. The higher temperature facilitated better diffusion of CO_2 molecules into the adsorbent's porous structure, enabling stronger adsorption interactions between CO_2 and the nitrogen groups on PKS-Char surfaces (Kasera, Kolar, & Hall, 2022)

In the case of PKS-AC, the CO_2 adsorption capacity was influenced by temperature and pressure. However, unlike PKS-Char, PKS-AC did not maintain a consistently high adsorption capacity at elevated temperatures. This could be attributed to the denaturation of unstable pores within the material (Duran-Jimenez et al., 2021). The optimized conditions (Table 4.8) for PKS-AC were determined to be 26.2°C and 3.4 bar, resulting in a CO_2 adsorption capacity of 2.202 mmol/g. The high surface area and pore structure of PKS-AC made it ideally suited for efficient CO_2 adsorption under elevated pressure conditions. The optimized conditions for PKS-AC-MgO were identified

at 39.9°C and 3.3 bar, resulting in a CO_2 adsorption capacity of 2.614 mmol/g. The presence of MgO led to an excellent CO_2 adsorption capacity (Creamer et al., 2018). Afterwards, validation runs at these optimum conditions have been carried out in order to determine the reproducibility, and the findings are tabulated in Table 4.8. Water bath temperature and pressure gauge reading were monitored continuously to get the consistent reading with the optimized condition. Based on Table 4.8, it shows that the experimental value of responses, R1 was closer to predicted value, with relatively small error between the predicted and actual experimental value which is below 1%.

In conclusion, the utilization of response surface plots in the DOE optimization and model validation process elucidated the influence of temperature and pressure on the CO_2 adsorption capacities of PKS-Char, PKS-AC, and PKS-AC-MgO. These findings underscore the importance of tailoring adsorption conditions to maximize the performance of different adsorbents for effective carbon capture applications.

Table 4.8: Validation of experimental runs at optimum levels.

Adsorbent	**Temperature (°C)**	**Pressure (Bar)**	**Predicted Adsorption Capacity (mmol/g)**	**Validated Adsorption Capacity (mmol/g)**	**Variance (%)**
PKS-Char	61	3.6	2.095	2.086	0.42
PKS-AC	26	3.4	2.202	2.197	0.22
PKS-MgO	39	3.3	2.614	2.621	0.26

4.6 Effects of Parameters

4.6.1 Temperature

At lower temperature, the active sites of PKS-AC and PKS-Char engaged in an interactions with CO_2 molecules, encompassing van der Waals forces, hydrogen bonding, and dipole-dipole interactions (Al Mesfer, 2020). Remarkably, for PKS-AC the adsorption rate of CO_2 did not exhibit a drastic reduction at 50°C and 75°C. This observation could be attributed to the elevated surface reactivity of PKS-AC and its pore structure as temperatures increased. The elevated surface reactivity after KOH activation fostered a more favorable interaction between CO_2 molecules and the PKS-AC surface, thereby reinforcing the adsorption forces between the adsorbent and CO_2 (Ello et al., 2013a). However, there are limits to the effect of high temperatures, as excessive heat can also lead to the closure or collapse of some pores, reducing the overall surface area and adsorption capacity which can be related to PKS-AC (Q. Li et al., 2020). Moreover, the rise in temperature corresponds to a decrease in CO_2 gas density, resulting in fewer CO_2 gas molecules available for adsorption. This phenomenon ultimately resulted in reduced CO_2 uptake by PKS-AC (Nowrouzi, Younesi, & Bahramifar, 2018).

PKS-AC-MgO, demonstrated the highest adsorption capacity across all temperature ranges among the three adsorbents. Comparatively, both PKS-Char, with a surface area of 418 m^2/g, and PKS-AC-MgO, possessing a surface area of 435 m^2/g, exhibited substantial CO_2 adsorption capacities, showcasing a consistent and gradual decline as temperature increased. The data aligned with similar trends seen in other studies employing biomass-based adsorbents, characterized by negative linear correlations with temperature—approximate slopes of -0.71 mmol/g·°C for PKS-AC-MgO, -0.55 mmol/g·°C for PKS-AC, and -0.995 mmol/g·°C for PKS-Char, in comparison to a walnut-based adsorbent with a slope of -0.014 mmol/g·°C (Al Mesfer, 2020). CO_2

adsorption on magnesium oxide encompasses both physisorption and chemisorption mechanisms (Al Mesfer, 2020). In physisorption, the adsorbate (CO_2) is held onto the surface of the adsorbent (magnesium oxide) through weak van der Waals forces or other non-covalent interactions. As the temperature rises, the thermal energy of the CO_2 molecules increases, making it easier for them to break the weak interactions and desorb from the adsorbent surface (Aladin, Modding, Syarif, & Dewi, 2021). Consequently, this reduces the amount of CO_2 that can be adsorbed.

Moreover, the adsorption process is influenced by thermodynamic factors. At higher temperatures, the entropic contributions to the adsorption process become more significant (Andirova et al., 2015). As a result, the increase in entropy can favor the desorption of CO_2 over adsorption, further reducing the overall adsorption capacity. This indicates at higher temperatures, the thermal energy disrupts the CO_2 adsorption bonds, leading to a release of the adsorbed CO_2 molecules from the surface of adsorbent which results in a decrease in the overall adsorption capacity (Danish et al., 2021). Despite PKS-Char demonstrating a similar adsorption capacity to PKS-AC-MgO, the inclusion of MgO in PKS-AC-MgO played a vital role in enhancing CO_2 adsorption through chemisorption.

The presence of a strong chemical interaction between CO_2 and the integrated MgO in PKS-AC-MgO could enhance the contribution of chemisorption to the overall adsorption at high temperatures (Y. Guo et al., 2019). The improved thermal and mechanical stability of PKS-AC-MgO, attributed to the addition of MgO on its surface, led to higher and more stable CO_2 adsorption compared to PKS-AC without metal oxide support (W. Gao et al., 2018). Based on these observations, an adsorption temperature of 25°C or below was considered ideal for achieving high CO_2 adsorption capacity, as higher temperatures might result in decreased adsorption performance.

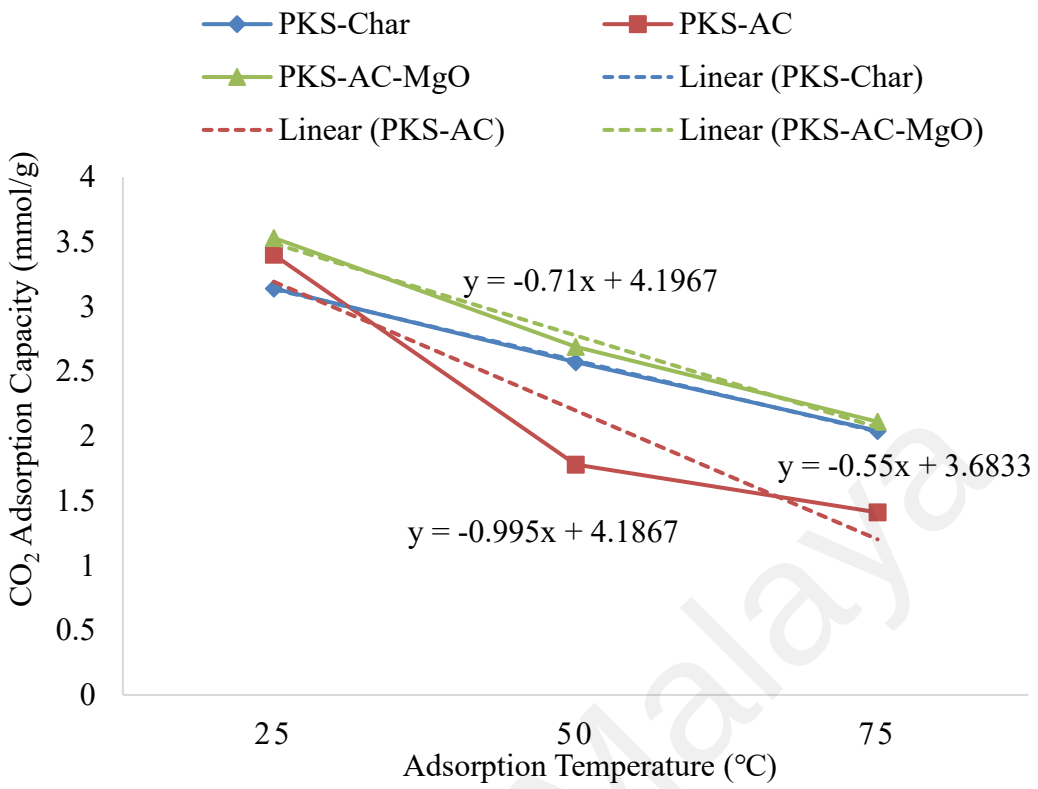

Figure 4.25: The effect of adsorption temperature on the CO_2 adsorption capacity on PKS-Char, PKS-AC and PKS-AC-MgO.

4.6.2 Pressure

It can be observed that the adsorption capacity increases with increasing pressure (Figure 4.26). This can be explained by the principle of adsorption equilibrium, where higher pressures result in a greater concentration of CO_2 molecules in the gas phase therefore creating a stronger driving force for CO_2 adsorption onto the surface of the adsorbent, leading to an overall increase in adsorption capacity. Previous studies by Abanades et al. (2005) and Lemus et al. (2012) supported this phenomenon, highlighting the role of increased CO_2 partial pressure in enhancing adsorption capacity (Abanades et al., 2005; Lemus et al., 2012). This is in accordance with Henry's law, which states that the amount of gas adsorbed is directly proportional to its partial pressure in the gas phase (Maring & Webley, 2013). Additionally, at higher pressures, CO_2 molecules have a higher tendency

of forming multilayer adsorption on the surface of adsorbent, further increasing the overall adsorption capacity (Shabbani et al., 2022).

PKS-Char and PKS-AC-MgO initially exhibited similar adsorption capacities at pressures of 1 bar to 2 bars. However, as the pressure increased, PKS-Char experienced a decrease in CO_2 adsorption capacity, while PKS-AC-MgO demonstrated a continuous increase. In contrast, PKS-AC initially had lower adsorption than PKS-Char at pressures of 1 bar to 3 bars, but it exhibited an increasing trend and surpassed PKS-Char at 4 bar. These findings indicate that PKS-AC performs better at higher pressures compared to PKS-Char. The adsorption capacity initially increases as the pressure rises due to the presence of available adsorption sites on the adsorbent surface. However, as the adsorption process continues and the adsorbed CO_2 molecules become more tightly packed, the number of potential adsorption sites decreases, leading to a decrease in CO_2 adsorption (Ammendola et al., 2017). Notably, PKS-AC-MgO demonstrated constant difference in adsorption capacity as the pressure increased, distinguishing it from the other adsorbents.

This suggests that the addition of MgO greatly enhances the suitability of PKS-AC-MgO for high-pressure applications. As observed, the adsorption capacity had not reached the maximum at 5 bars, indicating the potential for further adsorption at even higher pressures (Cai et al., 2022). To analyze the data, a power-law function $y = x^n$ was used to fit the curves. The obtained values of n were less than 1 for all three adsorbents: PKS-Char (0.4832), PKS-AC (0.5418), and PKS-AC-MgO (0.7036). These values align with findings from other studies using biomass adsorbents, where n values below 1 were commonly observed, for instance the study of Zhu et al. (2023) found n value of 0.824 (S. Zhu, Zhao, Zhang, & Su, 2023).

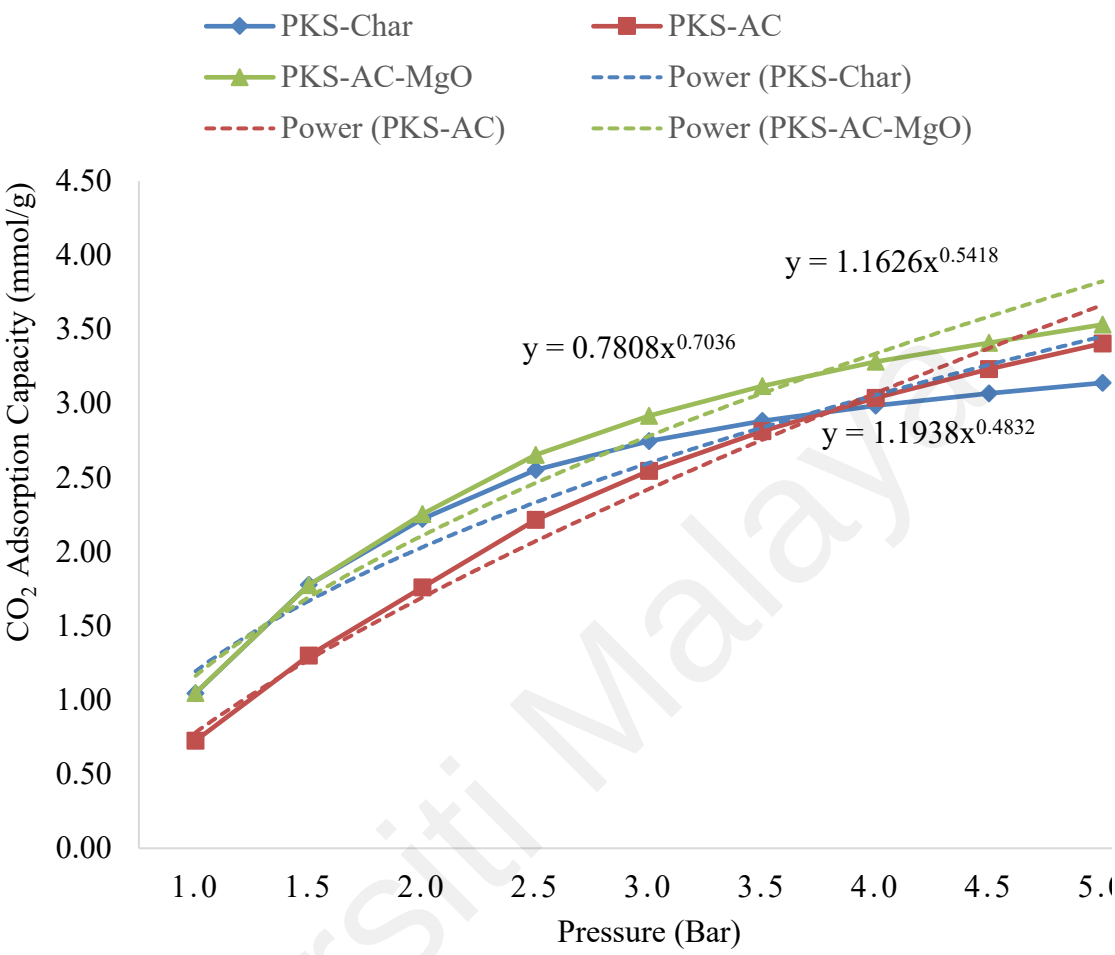

Figure 4.26: The effect of pressure on the CO_2 adsorption capacity for PKS-Char, PKS-AC and PKS-AC-MgO.

4.7 Process Mechanism and Adsorption Isotherm Analysis

4.7.1 PKS-Char

The CO_2 adsorption isotherm of PKS-Char was analyzed using various models (Table 4.9). Among the models applied, Langmuir isotherm, Elovich isotherm and Temkin isotherm exhibited the highest goodness of fit (R^2 > 0.85 to 1.00). Langmuir isotherm consistently provided the best fit at all temperatures: 25°C (R^2 = 0.9958), 50°C (R^2 = 0.9505), and 75°C (R^2 = 0.9944). This isotherm signifies the formation of monolayer

adsorption of CO_2 onto homogeneous surface of PKS-Char, indicating a finite number of identical adsorption sites. The maximum CO_2 adsorption on PKS-Char was calculated as 5.31 mmol/g at 25°C and 4.09 mmol/g at 75°C which showed the exothermic nature of CO_2 adsorption was in line with the decreasing Q_m value (maximum adsorption capacity) at elevated temperatures. The Langmuir constant (kL), representing adsorption affinity, exhibited a decrease with increasing temperature, indicating physisorption behavior (Darabi et al., 2021). Additionally, the favorability of the adsorption process was assessed using the separation factor R_L, with values within the 0-1 range indicating favorable adsorption (Figure 4.27). At lower pressures and temperatures, CO_2 adsorption on PKS-Char might involve physical adsorption. The interactions were primarily based on weak van der Waals forces, as PKS-Char polar functional groups could induce dipole-dipole interactions with CO_2, which was a polar molecule. The presence of nitrogen could enhance π-π interactions (L. An et al., 2019).

Elovich isotherm often used to describe chemisorption processes and assumes that adsorption occurs through a multistep process, involving both surface coverage and activation energy (Klusácek, Hudgins, & Silveston, 1989). The increased in the R^2 values, 0.8898 (at 25°C), 0.909 (at 50°C), and 0.9268 (at 75°C), as the temperature increases, was observed and this was because at higher temperatures, the kinetic energy of CO_2 molecules increased, potentially leading to more rapid surface interactions and reaction kinetics. Nitrogen functional group was observed in FTIR analysis if PKS-Char could introduce chemisorption sites on the PKS-char surfaces and these sites become more activated, increasing the availability CO_2 chemisorption and leading to increased maximum adsorption capacities with rising temperature (4.12 mmol/g < 4.91 mmol/g < 6.00 mmol/g). At higher pressures the nitrogen being electron-rich, could donate electrons to CO_2, leading to negatively charged chemisorption (Cao, Song, Zhao, & Zhong, 2013).

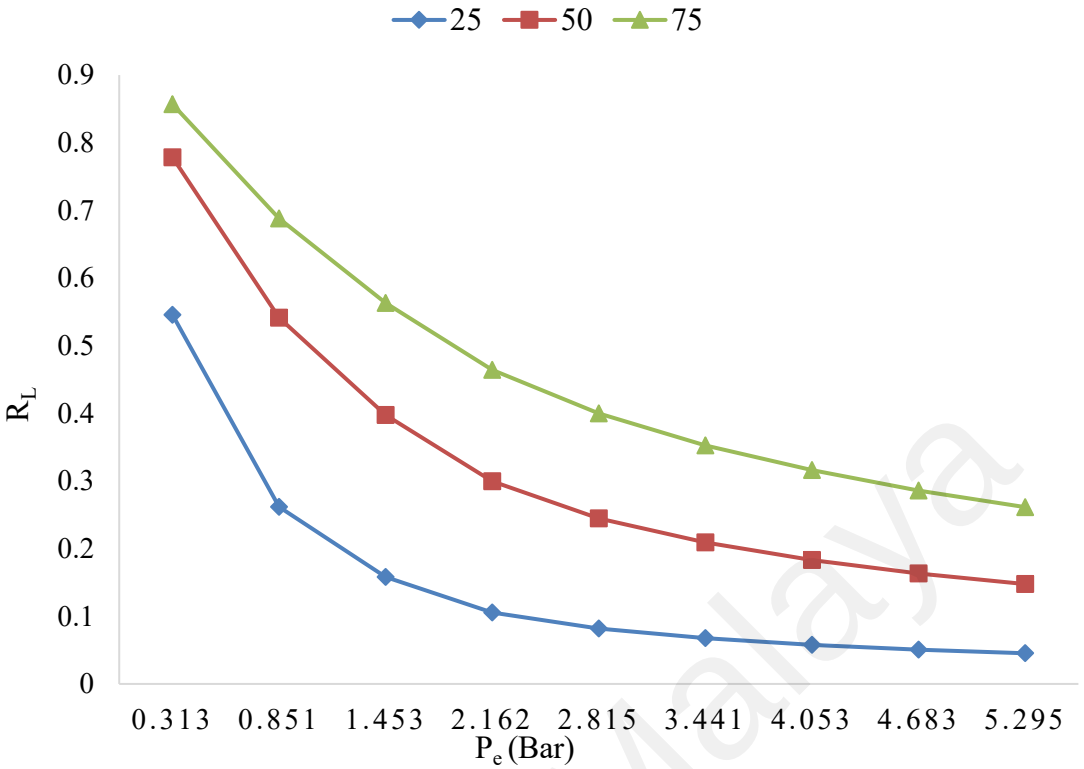

Figure 4.27: Langmuir separation factor, R_L as a function of pressure and temperature (25°C, 50°C and 75°C) of PKS-Char.

Moreover, the Temkin isotherm model with R^2 0.8522 (25°C), 0.8961 (50°C), and 0.929 (75°C) elucidated the indirect interaction between CO_2 molecules and PKS-Char surfaces with the heat of adsorption B (kJ/mol) increasing as temperature increased indicated that the adsorption process became more energetically favorable with rising temperature (Minani et al., 2014). Overall, the isotherm analyses have provided insights into the complex mechanisms governing CO_2 adsorption onto PKS-Char.

Table 4.9: Isotherm Model for PKS-Char

Two-Parameter Isotherm Models		**Temperature (°C)**		
		25	**50**	**75**
Langmuir	Q_m (mmol/g)	5.31	4.69	4.09
	K_L (1/bar) (Langmuir constant)	3.95	1.09	0.53
	R^2	0.9958	0.9949	0.9944
Freundlich	K_F (mmol/g.bar 1/n) affinity constant	1.35	0.95	0.65
	N (Freundlich constant)	20.49	17.54	15.43
	R^2	0.7434	0.7805	0.8081
Temkin	A_T (L/mg) equilibrium binding constant corresponding to the maximum binding energy	269.62	64.263	22.602
	B_T (J/mol) Temkin constant related to heat of adsorption	0.24	0.21	0.18
	B (kJ/mol) corresponding to the heat of adsorption	10.54	12.61	15.89
	B (J/mol) corresponding to the heat of adsorption	10542	12613	15888
	R^2	0.8522	0.8961	0.929
Dubinin	Q_m (mmol/g)	1.35	0.95	0.65
Radushkevich	E (kJ/mol)): mean free energy of adsorption	5.22	5.24	5.29
	λ (mol^2/J^2) ($\times 10^{-8}$)	-1.83	-1.81	-1.78
	R^2	0.7434	0.7805	0.8081
Elovich	Q_m (mmol/g)	4.12	4.91	6.00
	K_e	1.40	1.20	1.07
	R^2	0.8898	0.909	0.9268

4.7.2 PKS-AC

The adsorption isotherm modeling analysis of PKS-AC (Table 4.10), offers valuable insights into its CO_2 adsorption behavior. Among the various isotherm models applied, the Freundlich isotherm exhibited the best fit; 0.9813 (at 25°C), 0.9505 (at 50°C), and

0.9565 (at 75°C). The Freundlich isotherm well-suited for heterogeneous adsorption onto surfaces with varying adsorption energies and multilayer adsorption. This is particularly relevant for PKS-AC with KOH activation leads to high surface area and had a highly heterogeneous surface with varying pore sizes and functional groups (Ghosh et al., 2019). The decrease in the n values with increasing temperature highlights that higher temperatures are less favorable for CO_2 adsorption in PKS-AC. This can be attributed to the elevated energy levels acquired by adsorbed CO_2 molecules, enabling them to overcome van der Waals forces and return to the gas phase. Furthermore, the reduction in the constant K_F values with rising temperatures confirms the favorable adsorption behavior at lower temperatures and indicates an exothermic nature of the process (L. Li et al., 2019). The calculated R_L values at different pressures and temperatures, as shown in Figure 4.28, falling within the range of 0-1, indicate favorable CO_2 adsorption.

For higher temperature conditions (50°C and 75°C), the Temkin isotherm exhibited the best fit with R^2 values of 0.9910 and 0.9923, respectively. With continued CO_2 adsorption and temperature increase, enhanced repulsive forces among adsorbed molecules reduce the affinity to adsorb new CO_2 molecules, resulting in reduced adsorption capacity. This attributed to increase in heat of adsorption (B) with increasing temperature (Basheer et al., 2021). Additionally, the Dubinin Radushkevich isotherm provides insights into energy parameters, particularly the mean free energy of adsorption (E). Calculated E values within the range of 3-4 kJ/mol suggest that CO_2 adsorption onto PKS-AC is primarily physical in nature, given that E magnitudes are below 4.5 kJ/mol (Kwiatkowski, Serafin, Booth, & Michalkiewicz, 2021).

Table 4.10: Isotherm Model for PKS-AC

Two-Parameter Isotherm Models		**Temperature (°C)**		
		25	**50**	**75**
Langmuir	Q_m (mmol/g)	6.28	5.07	4.13
	K_L (1/bar) (Langmuir constant)	0.49	0.15	0.14
	R^2	0.8452	0.8848	0.8867
Freundlich	K_F (mmol/g.bar 1/n) affinity constant	0.90	0.33	0.26
	n (Freundlich constant)	13.48	10.92	10.85
	R^2	0.9813	0.9505	0.9465
Temkin	A_T (L/mg) equilibrium binding constant corresponding to the maximum binding energy	8.41	2.36	2.27
	B_T (J /mol) Temkin constant related to heat of adsorption	0.33	0.19	0.15
	B (kJ/mol) corresponding to the heat of adsorption	7.56	14.32	19.42
	B (J/mol) corresponding to the heat of adsorption	7558	14322	19417
	R^2	0.9589	0.9910	0.9923
Dubinin	Q_m (mmol/g)	0.90	0.33	0.26
Radushkevich	E (kJ/ mol)): mean free energy of adsorption	4.23	4.13	4.44
	λ (mol^2/J^2) ($\times 10^{-8}$)	-2.78	-2.92	-2.53
	R^2	0.8452	0.8848	0.8867
Hasley	K_H Halsey isotherm constants.	1.80	182.58	559.50
	N_H Halsey isotherm constants.	-5.85	-4.74	-4.71
	R^2	0.8452	0.8848	0.8867
Elovich	Q_m (mmol/g)	6.00	10.71	11.14
	K_e	1.16	0.97	0.95
	R^2	0.8885	0.8824	0.8794

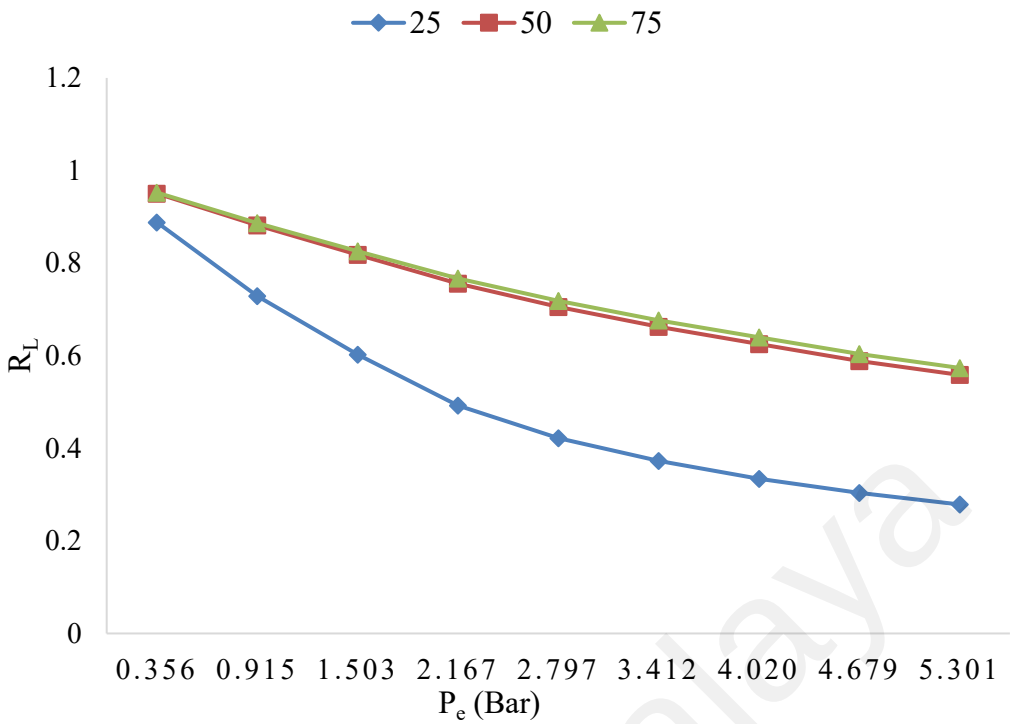

Figure 4.28: Langmuir separation factor, R_L as a function of pressure and temperature (25°C, 50°C and 75°C) of PKS-AC.

4.7.3 PKS-AC-MgO

The isotherm modeling results for PKS-AC-MgO (Table 4.12) shows that among various isotherm models, Langmuir, Temkin, and Elovich exhibit high coefficient of determination ($R^2 > 0.900$), indicating their accuracy in predicting CO_2 adsorption. The highest average R^2 value among these models is observed for Langmuir (0.9916), assumes monolayer adsorption, aligns well with the surface properties of PKS-AC-MgO. The decreasing trend of K_L values (1.288 at 25 °C, 0.77 at 50 °C, and 0.25 at 75 °C) as temperature increases indicates that PKS-AC-MgO had strong adsorbate-surface interactions at lower temperatures (Ammendola et al., 2017). The R_L values (0.1344 at 25°C, 0.1678 at 50°C, and 0.4473 at 75°C) falling within the range of 0-1 further confirm the favorable nature of CO_2 adsorption onto PKS-AC-MgO. The trends in the R^2 values of the Temkin isotherm, which increase with temperature, suggest indirect adsorbate-adsorbent interactions. An increasing heat of adsorption (B) value with temperature

indicates that the CO_2 adsorption process onto PKS-AC-MgO becomes more energetically favorable at higher temperatures, suggesting chemical interactions associated with chemisorption. Moreover, the Dubinin Radushkevich model and the E values (4.7-5.1 kJ/mol) provide insights into the physical-chemisorption of CO_2 onto PKS-AC-MgO (Iberahim et al., 2022).

From the isotherm analysis it revealed that PKS-AC-MgO and PKS-Char involved in both chemisorption and physisorption of CO_2. Meanwhile PKS-AC was governed by physisorption. The physisorption of CO_2 can occur via π-π interactions, van der Waals forces, electrostatic interactions (Alfe et al., 2021). All the synthesized adsorbent had a high surface area resulted from KOH activation which provided ample sites for CO_2 molecule to physically adhere (Asadi-Sangachini et al., 2019). Furthermore, the well-developed micropore volume in PKS-AC, PKS-Char and PKS-AC-MgO had also created network of pores where CO_2 permeated inner pore regions due to its size and linear structure and high boiling point fluids like CO_2 were rapidly adsorbed due to intermolecular attraction (Yusof et al., 2021). As stated in Table 4.11, CO_2 molecules are polarizable, meaning it can induce temporary dipoles in nearby atoms or molecules which allow CO_2 to experience van der Waals forces, particularly London dispersion forces, when in close proximity to the surface of the adsorbent (Creamer et al., 2018). These attractive forces between CO_2 and the adsorbent surface are relatively weak but can become significant when many CO_2 molecules are adsorbed. Additionally, the CO_2 permanent quadrupole moment leads to strong electrostatic contact enhanced CO_2 uptake on PKS-AC-MgO (3.53 mmol/g) is due to physical and chemical interactions (Ammendola et al., 2017).

The chemisorption of CO_2 onto PKS-AC-MgO can occur due to the functional group interactions MgO enhances surface polarity, enabling weak chemical contact with

CO_2 (Goel et al., 2021). Nitrogen active sites (PKS-Char) and MgO active sites (PKS-AC-MgO) present on the adsorbent can introduce specific functional groups such as amino ($-NH_2$) groups from nitrogen doping and oxygen vacancies from MgO, which can serve as active sites for chemical interactions with CO_2 molecules (Abuelnoor et al., 2021). Moreover, the nitrogen and oxygen present can act as a Lewis base, while CO_2 molecules can act as Lewis acids. This allows for Lewis acid-base interactions to occur, leading to the formation of chemical bonds between the CO_2 molecules and the functional groups on the adsorbent (L. An et al., 2019). Chemisorption can result in the formation of carbonate (CO_3^{2-}) and bicarbonate (HCO_3^-) species which is formed through chemical reactions between CO_2 and the functional groups on the surface of the adsorbent (Goel et al., 2021). Carbonate formation is catalyzed by the hydroxyl group, resulting in bicarbonate species (Yusof, Othaman, Setiabudi, & Teh, 2021). Bidentate carbonate arises from Mg^{2+} and O^{-2} sites interacting with CO_2, leading to CO_3-^{2} species formation on the MgO surface which was proven in the FTIR analysis presented in Figure 4.29. FTIR spectra analysis of PKS-AC-MgO before and after CO_2 adsorption confirms the formation of certain carbonates. The post-adsorption spectrum shows decreased wavelengths, indicating successful CO_2 filling. Additional peaks appear due to chemical bond formation between CO_2 and MgO, notably carbonate. The spectrum exhibits broad bands at 3013 cm^{-1} and 2887 cm^{-1}, attributed to hydroxyl (-OH) groups, contributing to enhanced CO_2 adsorption and hydrogen carbonate formation (Chang, Kao, Shen, Kang, & Wang, 2020). Chemical reaction products of MgO and CO_2 appear between 1750^{-1} and 600 cm^{-1}, aligning with Density Functional Theory (DFT) predictions of CO_2 adsorption on edge and corner sites of MgO (Baltrusaitis, Hatch, & Orlando, 2012). Peaks at 1559 cm^{-1} correspond to C-O stretching, and 612 cm^{-1} suggests magnesite ($MgCO_3$) presence. Similar observations of monodentate carbonate formation were reported in related studies (Ammendola et al., 2017).

Table 4.11: Physical and chemical characteristics of CO_2 molecules

Factors	CO_2 properties
Kinetic Diameter (nm)	0.33
Shape	Linear
Quadrupole moment (10^{-26}esu.cm^2)	4.30
Dipole moment (10^{-26} esu·cm^2)	0
Polarizability (10^{-25} cm^3)	29.1
Boiling Point (K)	216.55

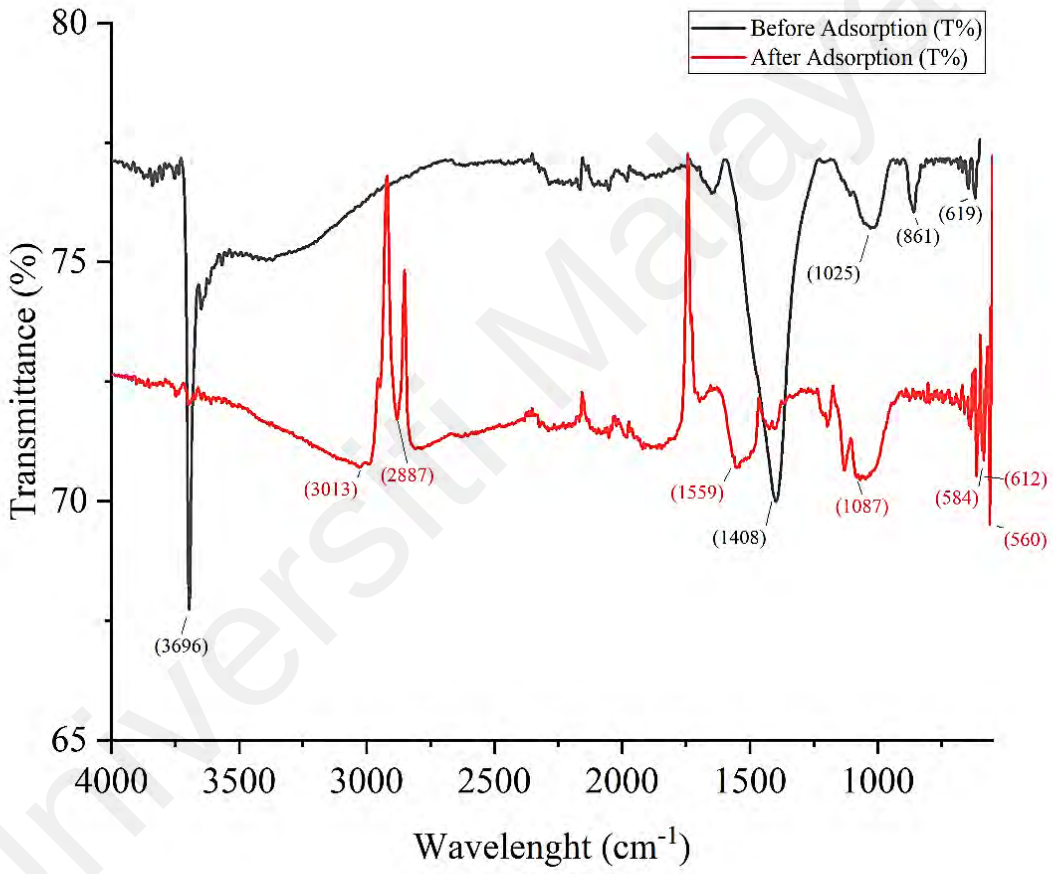

Figure 4.29: FTIR analysis on functional group present of PKS-AC-MgO before and after adsorption of CO_2.

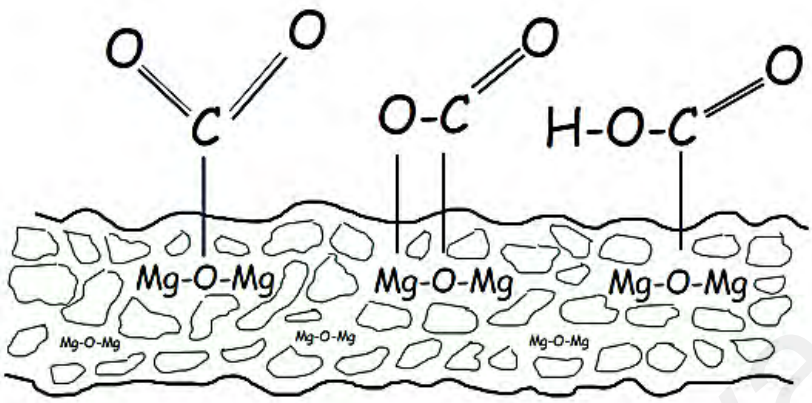

Figure 4.30: Carbonate species formed on PKS-AC-MgO adsorbent (monodentate carbonate, bidentate carbonate, bicarbonate)

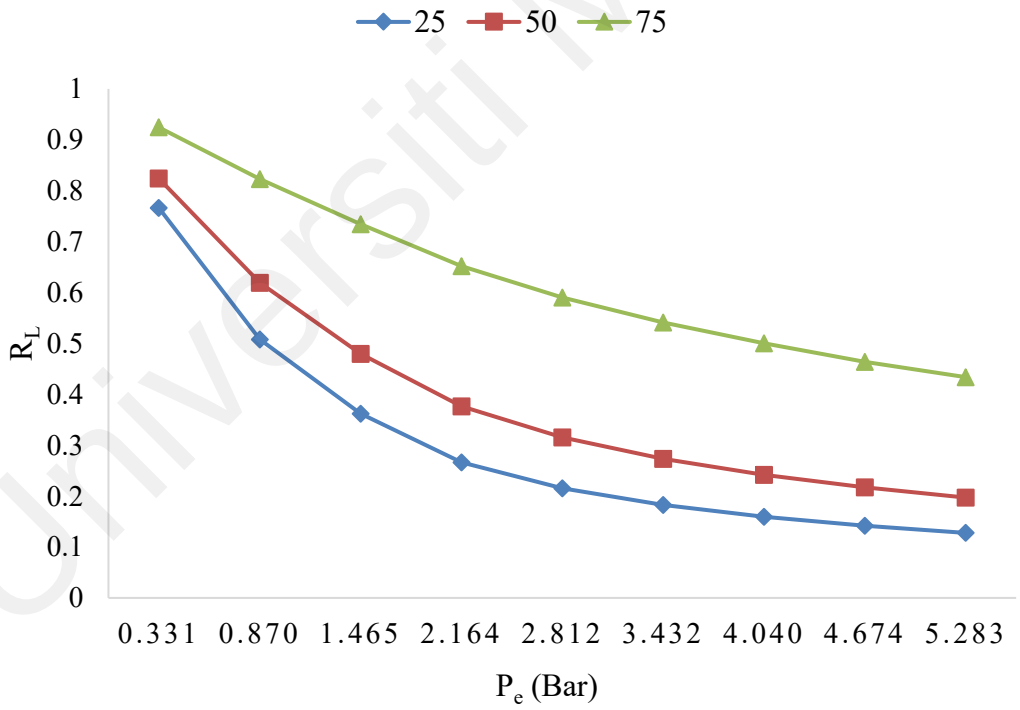

Figure 4.31: Langmuir separation factor, R_L as a function of pressure and temperature (25°C, 50°C and 75°C) of PKS-AC-MgO

Table 4.12: Isotherm Model for PKS-AC-MgO

Two-Parameter Isotherm Models		**Temperature (°C)**		
		25	**50**	**75**
Langmuir	Q_m (mmol/g)	6.78	5.07	4.98
	K_L (1/bar) (Langmuir constant)	1.29	0.77	0.25
	R^2	0.9916	0.9922	0.9785
Freundlich	K_F (mmol/g.bar 1/n) affinity constant	1.32	0.92	0.48
	N (Freundlich constant)	178.57	16.50	12.25
	R^2	0.7975	0.8047	0.8516
Temkin	A_T (L/ mg) equilibrium binding constant corresponding to the maximum binding energy	67.41	36.32	4.78
	B_T (J/ mol) Temkin constant related to heat of adsorption	0.29	0.23	0.21
	B (kJ/mol) corresponding to the heat of adsorption	8.56	11.65	13.80
	B (J/mol) corresponding to the heat of adsorption	8564	11645	13803
	R^2	0.9083	0.921	0.9749
Dubinin	Q_m (mmol/g)	1.32	0.92	0.48
Radushkevich	E (kJ /mol)): mean free energy of adsorption	4.87	5.08	4.72
	λ (mol^2/J^2) ($\times 10^{-8}$)	-2.09	-1.93	-2.24
	R^2	0.7975	0.8047	0.8516
Elovich	Q_m (mmol/g)	4.66	5.31	8.18
	K_e	1.32	1.17	1.01
	R^2	0.8872	0.9075	0.9178

In summary, the CO_2 adsorption isotherms for PKS-Char, PKS-AC, and PKS-AC-MgO exhibited distinct characteristics and mechanisms. The Langmuir isotherm, signifying monolayer adsorption, fitted well for both PKS-Char and PKS-AC-MgO. PKS-Char, produced through pyrolysis with nitrogen flow, showcased active nitrogen sites on its surface, contributing to both physisorption and chemisorption with a maximum adsorption capacity of 5.31 mmol/g at 25°C was achieved. In contrast, PKS-AC, activated with KOH to enhance its surface area, predominantly engaged in physisorption due to its

higher surface area and multilayer adsorption propensity. No nitrogen sites were detected on PKS-AC's surface, attributed to the absence of nitrogen during its second carbonization. PKS-AC achieved a maximum adsorption capacity of 6.28 mmol/g. Lastly, PKS-AC-MgO demonstrated primarily monolayer adsorption, attaining a notably higher maximum adsorption capacity of 6.78 mmol/g at 25℃, owing to the synergistic effect of MgO addition that enhanced chemisorption. The tailored characteristics of these adsorbents allowed for optimized CO_2 capture mechanisms in various conditions.

4.8 Thermodynamic Analysis

One of the essential characteristics for CO_2 adsorption is the isosteric heat of adsorption (ΔH_{ads}, kJ/mol), free energy (ΔG), and entropy (ΔS) as they are the major thermodynamic parameters that provide insight into the mechanism of adsorption processes. Table 4.13 presents the calculated thermodynamic properties of the synthesized adsorbent. The obtained results reveal an exothermic nature of the CO_2 adsorption process, as indicated by the negative sign of ΔH_o. The magnitude of ΔH_o provides insights into whether the CO_2 adsorption is a physical or chemical process. It was established that for physisorption, ΔH_o magnitudes are < 20 kJ/mol, while intermediate values (around 20 to 40 kJ/mol) encompass both weaker physisorption interactions and weaker chemisorption interactions (Ammendola et al., 2017). In this study, the computed ΔH_o value for PKS-AC was found to be 17.45 kJ/mol, indicating a physisorption behavior, consistent with previous findings (Nugent et al., 2013). PKS-Char and PKS-AC-MgO exhibited higher ΔH_o values of 23.52 kJ/mol and 28.47 kJ/mol, suggesting a combined physio-chemisorption mechanism (Crone & Türk, 2022). Overall, the relatively low heat of adsorption for all three adsorbents indicates that less energy is required for regeneration, and this is a favorable characteristic for practical applications (Ammendola et al., 2017).

The negative ΔS_o values obtained from the analysis indicate a higher degree of orderliness for CO_2 molecules upon adsorption. This suggests a transition from a disordered state on the adsorbent's surface to a more regulated state during the adsorption process, reflecting the behavior of CO_2 molecules (Kalaimurugan, Durairaj, Kumar, Senthilkumar, & Venkatesan, 2020). The reduction in entropy is attributed to the limited flexibility of CO_2 gas molecules as they encounter a lack of free space on the adsorbent's surface. Regarding the ΔG_o values, they can be classified into negative and positive regions. A negative ΔG_o at low temperatures signifies favorable and spontaneous adsorption, while a positive value at high temperatures indicates a non-spontaneous adsorption process (Bond, Alonso, West, & Dumesic, 2010).

Table 4.13: Thermodynamic parameter evaluated for CO_2 adsorption at different temperature (25 ℃, 50 ℃ and 75℃)

Adsorbents	Temperature (K)	ΔH (kJ/mol)	ΔS(kJ/mol)	ΔG(kJ/mol)
PKS-Char	298	-23.52	-0.10	-3.41
	323			-0.23
	348			1.82
PKS-AC	298	-17.45	-0.08	-1.78
	323			5.11
	348			5.68
PKS-AC-MgO	298	-28.47	-0.09	-0.63
	323			0.70
	348			4.04

Additionally, the decrease in the absolute value of ΔG with increasing temperature suggests that the affinity of CO_2 adsorption onto the prepared adsorbent diminishes at higher temperatures (Ammendola et al., 2017). Notably, all the adsorbents exhibited negative ΔG_o values at low temperatures, indicating the occurrence of viable, and spontaneous CO_2 adsorption in these adsorbents. The decrease in the absolute value of

ΔG with increasing temperature further illustrated the reduced affinity of CO_2 adsorption onto the prepared adsorbent at higher temperatures (Nugent et al., 2013).

4.9 CO_2 Desorption and Activated Carbon Regeneration Study

All of the adsorbents were subjected to a 0.6-bar CO_2 desorption process at 25 °C. As depicted in Figure 4.32, among the three adsorbents, PKS-AC exhibited a faster CO_2 desorption rate compared to PKS-Char and PKS-AC-MgO. Starting from an initially adsorbed value of 3.4 mmol/g, PKS-AC efficiently desorbed nearly 2.23 mmol/g of CO_2 as the pressure reached 0.63 bar. This observation aligns with the isotherm analysis, corroborating the prevalent physisorption mechanism, which posits that physiosorbed CO_2 can be readily desorbed from the adsorbent surface.

However, a delay in the desorption process was noticed for PKS-Char at higher pressures (4.67 bar) compared to PKS-AC-MgO, which exhibited rapid initial desorption. In accordance with the isotherm theory, both PKS-Char and PKS-AC-MgO experienced CO_2 adsorption through a combination of physisorption and chemisorption. The swift desorption rate can be attributed to the relatively weaker bicarbonate bonds formed between CO_2 and MgO. Notably, as the pressure decreased, PKS-Char progressively desorbed more CO_2 (2.06 mmol/g), whereas PKS-AC-MgO only desorbed 1.45 mmol/g of CO_2 by the end of the desorption process (A. H. Ruhaimi et al., 2021). CO_2 molecules chemisorbed on PKS-AC-MgO formed a strong monodentate bonding that could not be desorbed at 25 °C, indicating the presence of chemisorption in PKS-AC-MgO.

Temperature-programmed desorption (TPD) analysis was conducted to measure the amount of desorbed CO_2 from the sorbent subsequent to CO_2 exposure. Alongside adsorption capacity, the regenerative property, wherein chemically bonded CO_3^{2-} is released as CO_2 through thermal decomposition, constitutes one of the most pivotal considerations. This chemical phenomenon was examined to ascertain the maximum

desorption temperature and the amount of CO_2 chemisorbed onto PKS-AC-MgO adsorbent was 1.35 mmol/g.

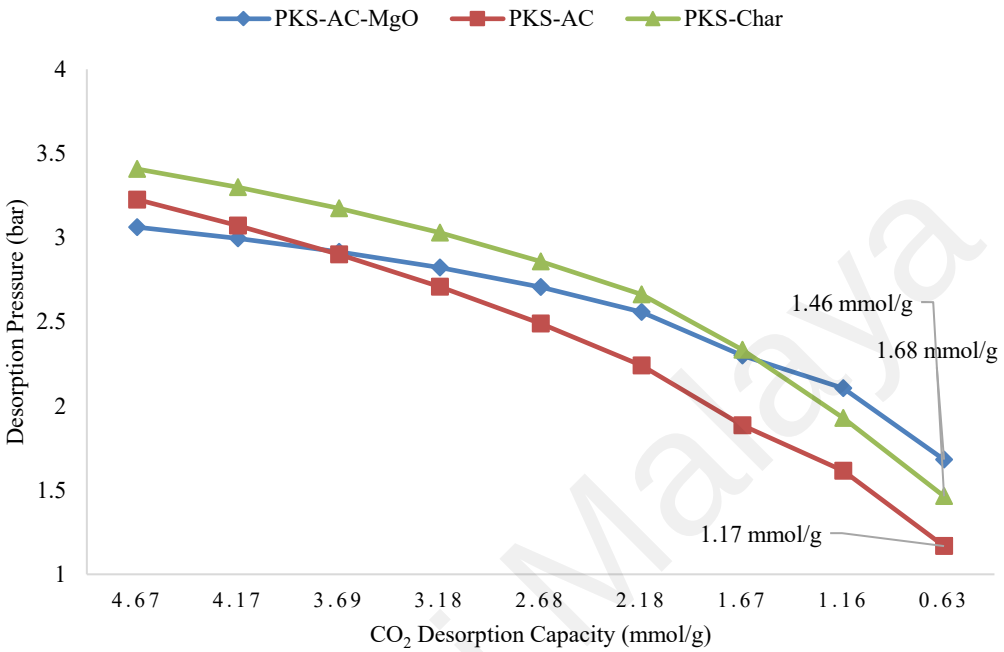

Figure 4.32: CO_2 desorption of PKS-Char, PKS-AC and PKS-AC-MgO

Based on Figure 4.33, the first desorption of adsorbed CO_2 occurred around below 100 °C, and the second desorption occurred between 400–600 °C. This shows that weakly bonded CO_2 had been easily desorbed at lower temperature meanwhile CO_2 with stronger bond with PKS-AC-MgO had a higher chemical desorption temperature indicating the presence of active site of MgO in deeper pores (J. Huang & Korzeniewski, 1999).

Throughout the pulse CO_2 chemisorption and desorption test depicted in Figure 4.34, a total of 10 cycles were executed. PKS-AC-MgO effectively conducted CO_2 adsorption and subsequent desorption for the initial 6 cycles, all accomplished within a span of 25 minutes. This timeframe highlighted the dynamic interaction between CO_2 molecules and the active sites present on the adsorbent surface.

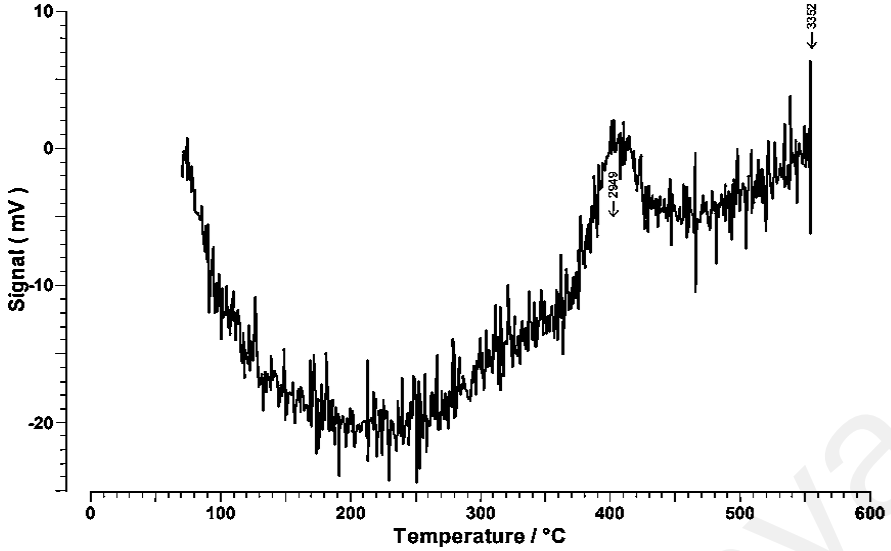

Figure 4.33: CO_2-TPD profiles of PKS-AC-MgO

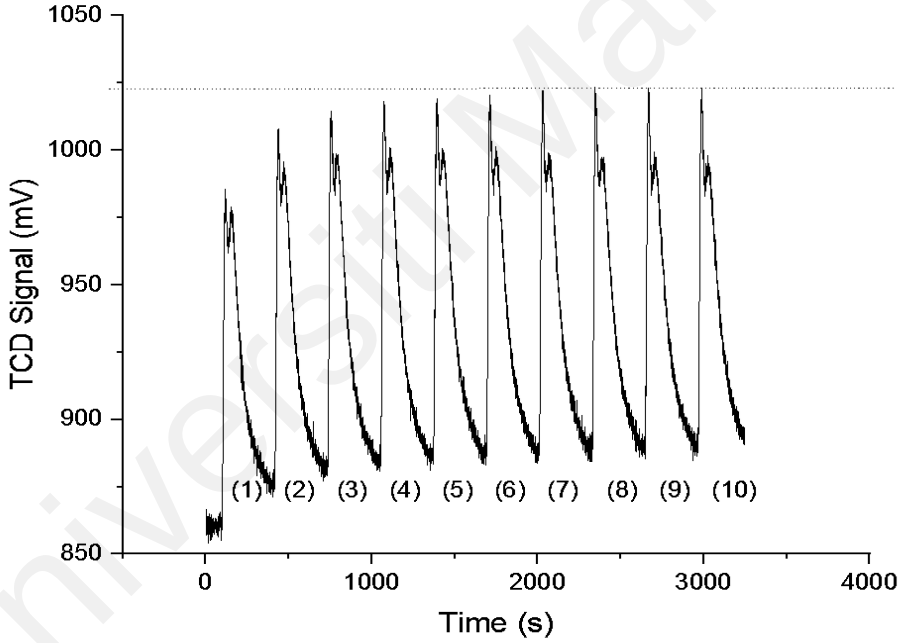

Figure 4.34: Temperature Programmed Desorption (TPD) graph for Pulse CO_2 Chemisorption using PKS-AC-MgO Adsorbent.

However, commencing from the 7th to the 10th cycle, the adsorption process reached a saturation point. At this stage, no further CO_2 could be adsorbed onto the adsorbent due to the active sites becoming fully occupied by CO_2 molecules. These molecules formed strong bonds with the MgO functional groups, necessitating elevated

energy levels for successful desorption. This behavior is attributed to the robust chemical bonding between CO_2 and the adsorbent, which is consistent with the requirement for higher energy during desorption (Cai et al., 2022).

4.10 Physiochemical Properties and CO_2 Adsorption Performance Comparison with Commercial Adsorbent.

Table 4.14 revealed that all the synthesized adsorbent in this study had improved adsorption capacity compared to various biomass-based adsorbents and commercial adsorbent. It shows a successful development of adsorbents from PKS biomass which had excellent characterization and adsorption properties. Norit GSX (commercial adsorbent) with surface were of 1002 m^2/g which commonly used in the water treatment and air purification process attained CO_2 adsorption of 2.99 mmol/g lesser compared to PKS-AC-MgO (3.53 mmol/g) and PKS-AC (3.40 mmol/g) (N. A. Rashidi & Yusup, 2019). Similarly commercial AC CarboTech PAK 800 (984 m^2/g) which used for gas purification such as hydrogen sulfide obtained CO_2 adsorption capacity of 2.13 mmol/g (Benedetti, Cordioli, Patuzzi, & Baratieri, 2019). In this context PKS-AC-MgO with lower surface area than CarboTech PAK 800 had outperformed. Additionally, silica gel is also being used for CO_2 adsorption and Davisil™ AMD16 is a type of silica gel manufactured by Grace Davison. Silica gels are amorphous and porous materials composed of silicon dioxide (SiO2), and from the study conducted by (Murakami, Watanabe, Kato, & Sugawara, 2013) it shows that Davisil AMD16 only attained 1.39 mmol/g of CO_2 adsorption at 25°C. PKS-Char with single carbonization had outperformed both the surface area and adsorption capacity of Davisil silica gel. Furthermore, raw metal oxide such as tungsten oxide (WO_3), cerium oxide (CeO_2), and magnesium oxide (MgO) have been investigated for their potential to adsorb CO_2 at an industrial level. From the study conducted by (Crone & Türk, 2022) these raw metal still

underperformed the synthesized PKS-based AC at 25℃. Utilization of raw MgO only resulted in 0.68 -1.81 mmol/g of adsorption capacity whereas the uptake capacity had been enhance when impregnated with carrier such as PKS (Andirova et al., 2015). The utilization of biomass as the support material not only enhanced the CO_2 intake but also increased the surface area of the AC (Chammingkwan et al., 2021).

Based on the comparison with various biomass-based adsorbent, PKS-char had a relatively high CO_2 adsorption capacity of 3.14 mmol/g when compared to other ACs such as wood-based biochar (0.85 mmol/g), walnut shell-based biochar (1.85 mmol/g), untreated sludge-based char (1.71 mmol/g), and rice straw char (1.87 mmol/g) (Abuelnoor et al., 2021). This is owing to PKS biomass's high carbon content of 44.74% when compared to other biomass (anak Erison et al., 2022). The presence of a nitrogen functional group in FTIR analysis contributed to the increase in alkalinity of the PKS-Char surface and improved the interaction between the carbon surface and the acid molecule of CO_2 (Baltrusaitis et al., 2012). Liying An (2019) had reported to obtain the CO_2 adsorption capacity of 2.39 mmol/g of by using graphene-derived N-enriched porous carbons synthesized from urea and KOH activation. They have suggested that the presence of nitrogen atom is one of the major factor for high intake of CO_2 (L. An et al., 2019). The strong dipole interaction between the massive quadrupole moment of the CO_2 molecule and the polar sites associated with the nitrogen functional group could increase the CO_2 uptake by 3-50% when compared to pristine biochar as reported by (Crone & Türk, 2022)

In overall the CO_2 uptake of PKS-adsorbent synthesized in this study were relatively high compared to the both commercial and biomass-based adsorbents which indicates it can be a great alternative to commercially available CO_2 adsorbent. However commercial AC products have already established in the market therefore to introduce a

new biomass-based adsorbent, it needs to be competitive not only in terms of performance but also in terms of cost. Hence technoeconomic analysis of biomass-based adsorbent is crucial was it provides insights into the economic feasibility, competitiveness, and sustainability.

4.11 Techno-Economic-Environmental Assessment

The proposed flow diagram of PKS-AC-MgO synthesis (Figure 4.35), had several processes including washing, drying, grinding, pyrolysis, KOH activation and MgO functionalization.

Table 4.14 : Comparison with various biomass-based and commercial adsorbents.

Biomass-based ACs and Commercial ACs	Synthesis Method	BET Surface area (m^2/g)	Experimental Condition	Result (mmol/g)	Reference
PKS-Char	Carbonization	413		3.14	**This study**
PKS-AC	Carbonization + Activation	1086		3.40	
PKS-AC-MgO	Carbonization +Activation + Impregnation	438		3.53	
Untreated sludge char	-	74.09		1.72	(C. Liu et al., 2023)
Rice straw char	-	-		1.88	
Metal Oxide (Tungsten (VI) oxide)	-	7	Temperature: 25°C Pressure: 1 Bar	0.30	(Crone & Türk, 2022)
Metal Oxide (Cerium (IV) oxide)	-	32		1.70	
Metal Oxide (Titanium dioxide)	-	57		3.10	
CaO-Fibrous Silica	-	45		0.76	(Yusof et al., 2021)
MgO-Egg Shell	-	79		1.55	(Amirul Hafiiz Ruhaimi & Ab Aziz, 2021)

Table 4.14 continued

Biomass-based ACs and Commercial ACs	Synthesis Method	BET Surface area (m^2/g)	Experimental Condition	Result (mmol/g)	Reference
Walnut Shell	Carbonization	700		1.86	(Al Mesfer, 2020)
Activated Carbon	Carbonization	500-1500		0.45-1.13	(Benedetti et al., 2019)
Zeolites	-	200-800	Temperature: 25°C Pressure: 1 Bar	0.11-0.34	
Metal organic frame works (HKUST-1)	-	2200		0.45-2.72	
Silica gel	-	300-800		0.22-0.45	
Norit GSX (Commercial AC)	-	1002		3.01	
CarboTech PAK 800 (Commercial AC)	-	984	Temperature: 50 °C	2.13	
Commercial AC (FPV)	-	-		2.24	(Sreńscek-Nazzal & Kiełbasa, 2019)

Table 4.14 continued

Biomass-based ACs and Commercial ACs	Synthesis Method	BET Surface area (m^2/g)	Experimental Condition	Result (mmol/g)	Reference
Commercial AC (WG-12)	-	-		2.04	
Commercial AC (CWZ-22)	-	-	Temperature: 25°C Pressure: 1 Bar	2.06	
Wood-based Char	Carbonization + KOH Activation	774		0.85	(Benedetti et al., 2019)
Magnesium Oxide	Direct Calcination	123	Temperature: 90°C	0.70	(Birgani et al., 2016)
	Meso-MgO	250	Temperature: 25°C	1.82	
Coffee grounds	KOH activated	-	Temperature: 25°C	2.67	(Al Mesfer, 2020; Cho et al., 2015)
Coconut Shell	Carbonization + Single stage (CO_2) activation	371	Temperature: 25°C	1.80	(Nor Adilla Rashidi, Yusup, Borhan, & Loong, 2014)
Silica (Davisil™) AMD16	-	199	Temperature: 25°C	1.40	(Murakami et al., 2013)

TEEA was begun with equation stated in Eq 3.4 to Eq 3.6 with an assumption of the annual duration for PKS-AC-MgO production of 7920 hours, considering 330 working days in a year.

The fixed capital estimation (FCE) for setting up a PKS-AC-MgO preparation unit includes expenses related to equipment purchase, installation, process piping, electrical systems, instrumentation and controls, buildings, yard improvements, construction. The working capital cost (WCC), which is 6.5% of the FCE, is also included. (Han, Fang, Liu, & Tang, 2016). Therefore, the total FCE for designing the preparation unit amounted to USD 282,534. According to Eq 3.5, the TCI is can be calculated at USD 717,295. The economic viability of PKS-AC-MgO can be assessed through a techno-economic analysis proposed by (Han et al., 2016).

Table 4.15 presents the AOC of PKS-AC-MgO preparation, where the C_{RM} cost is assumed to be USD 60. The total cost of utilities was estimated to be USD 2,200/year which was based on the water and electricity cost in Malaysia and in accordance with the evaluation done by (Yunus et al., 2020).

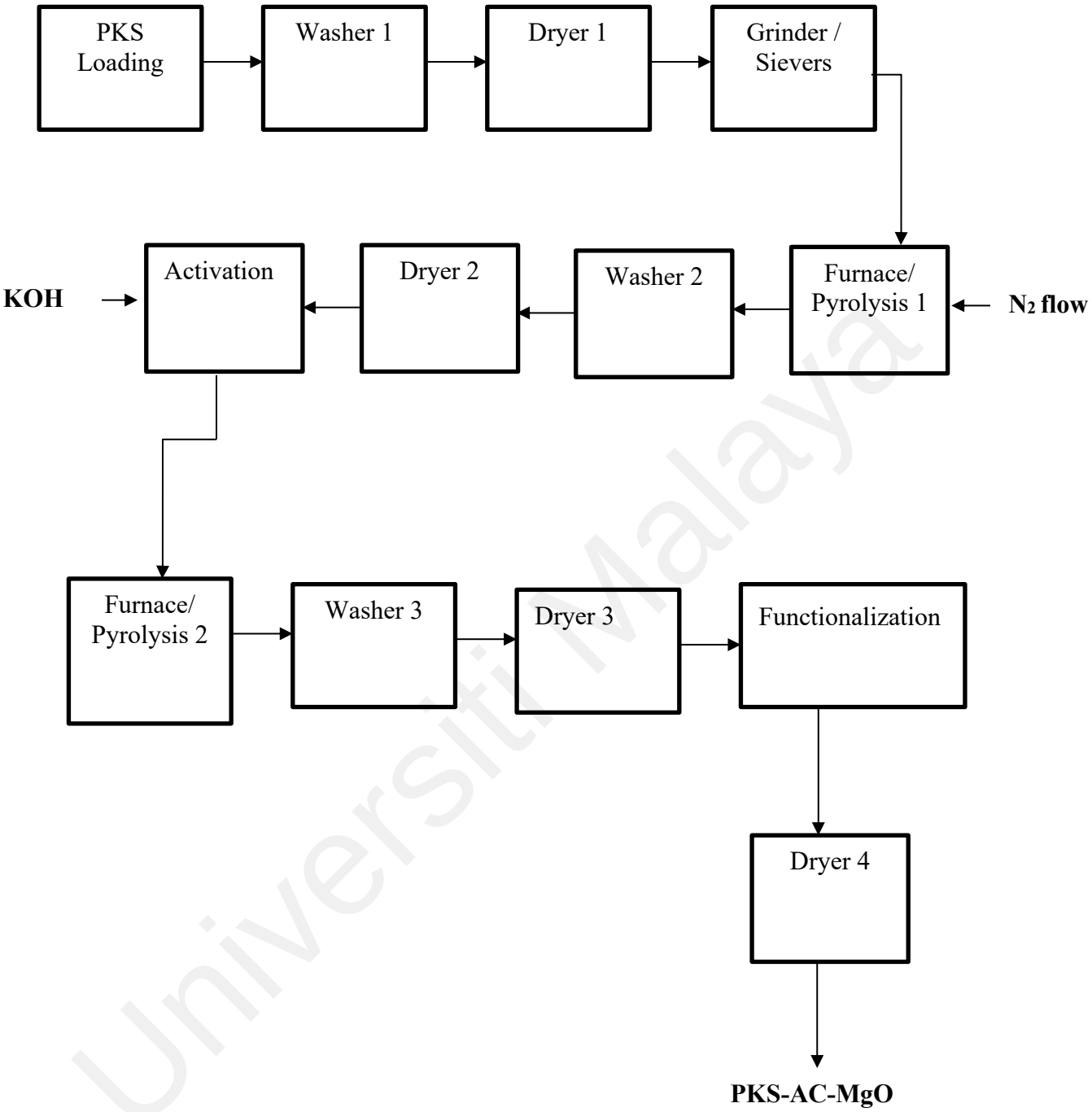

Figure 4.35: Process flowsheet for the synthesis of PKS-AC-MgO

Table 4.15: Fixed Capital Estimation (FCE) for the synthesis of PKS-AC-MgO

Item	Quantity	Percentage of FCE (%)	Cost (USD)	Total (USD)
Dryers	4	42.16	3,000	12,000
Mixing Tanks	2		3,000	6,000
Granulation Machine	1		15,000	15,000
Conveyor System	1		100,000	100,000
Washer Tanks	2		3,000	6,000
Furnace	2		20,000	40,000
Total				179,000
Equipment Installation	1	12.05		21,570
Process Piping	1	7.23		12,942
Electrical System	1	4.82		8,628
Buildings	1	4.82		8,628
Yard Improvement	1	19.28		34,511
Construction	1	2.41		4,314
			Total	282 534

Two operators were required for the operation of the PKS-AC-MgO unit and they were paid an average salary of 10,000.00 USD/year each. Maintenance and insurance costs were estimated at 2% and 1% of the FCE, respectively (Chong et al., 2020). The total annual operating cost of the unit was calculated to be USD 434,761.

Table 4.16: Annual operating cost for the synthesis of PKS-AC-MgO

Item	Component	Price (USD)	Unit	Quantity/Year	Cost (USD)
Raw material	PKS	60	USD/tonne	330	19,800
	Potassium Hydroxide (KOH)	506	USD/tonne	660	333,960
	Magnesium Oxide (MgO)	425	USD/tonne	165	70,125
Utilities	Electricity	0.04	USD/kWh	50000	2,000
	Water	0.01	USD/m^3	20000	200
Other costs	Labour	10,000	USD/employee	2	20,000
	Maintenance	2	% of FCE	0.02	5,651
	Insurance	1	% of FCE	0.01	2,825
				Total AOC	454,561

Table 4.17: Annual revenue and profitability for the synthesis of PKS-AC-MgO

	Price (USD/tonne)	Quantity/tonne	Value
PKS-AC-MgO	2500	231	577,500
Annual Revenue (A_R)			577,500
Annual operation cost			454,561
Local tax			86,625
Annual Profitability			36,314

About 70% of PKS-AC-MgO was obtained from 200 g of raw PKS. Therefore, it can be assumed that 2 tonne of raw PKS can yield almost 1.4 tonne of PKS-AC-MgO per day, requiring 4 tonne of KOH and 1 tonne of MgO. From the Table 4.17, the revenue for PKS-AC-MgO was estimated at USD 577,500 per year based on a current price of USD 2300 for 1 tonne of PKS-AC-MgO (Benedetti et al., 2019). The preparation process takes 2 days, and 165 processes can be carried out each year to produce 231 tonne of PKS-AC-

MgO. The local tax rate in Malaysia is 15%, which amounts to USD 86,625, and the AOC is USD 454,561 per year. After tax, the annual profitability of PKS-AC-MgO is USD 36,314. The specific cost of PKS-AC-MgO, is estimated at USD 1,967/tonne, which is 18% lower than the commercial market price of USD 2,400/tonne based on World AC Market Analysis (Asadi-Sangachini et al., 2019). Compared to other biomass-based AC , the cost of PKS-AC-MgO is relatively lower, for example, the current market price for AC is around USD 4,800/tonne in United States, while in Korea, the selling price is as high as USD 13,000/tonne (anak Erison et al., 2022).

The payback period for PKS-AC-MgO production was X = 2.31 years based on assumptions made in the analysis. Table 4.19 shows that the annual PKS-AC-MgO production is 231 tonne. The simple payback period is 2.31 years. The estimated annual processing capacity of PKS waste was 330 tonnes, which is expected to result in the production of 231 tonnes of PKS-AC-MgO per year. The carbon content and stability values of PKS-AC-MgO, 0.55 and 0.80 respectively, based on medium temperature pyrolysis (Alnouss, Shahbaz, McKay, & Al-Ansari, 2022).

Table 4.18: Cost-Comparison of PKS-AC-MgO with other commercial and biomass-based ACs.

Feedstock	Synthesize Method	Minimum selling price (U.S $/tonne)	Reference
PKS-AC-Mg	Slow pyrolysis (KOH, MgO)	1,967	Present Work
Rice husks	Microwave slow pyrolysis (NaOH)	3,580-3,770	(Caglar, Niemantsverdriet, & Weststrate, 2016)
Rice Bran	Slow pyrolysis with functionalization (CO_2)	3,540	(de Lorena Diniz Chaves, Siman, Ribeiro, & Chang, 2021)
Acid treated rice bran	Slow pyrolysis (CO_2)	20,450	(Creamer et al., 2016)
Pecan shells	Microwave slow pyrolysis (steam)	2,720	(Mohd Azmi, Buthiyappan, Abdul Raman, Abdul Patah, & Sufian, 2022)
Almond shell	Microwave slow pyrolysis (H_3PO_4)	2,450-2,820	(Creamer et al., 2016)
Commercial activated carbon	-	2,400-3,000	(Chong et al., 2020)

The environmental assessment was made using Eq 3.7 and Eq 3.8. The yearly decreases in the greenhouse gases emissions are projected to be 381.9 tons of CO_2. Where the annual electricity usage estimated is 50,000 kWh/year resulted in a 42.5 tCO_2 of carbon emission. This value is 9 times smaller than the annual GHG emission reduction by PKS-AC-MgO at 381.9 tCO_2 indicates that the synthesis of PKS-AC-MgO from PKS waste contributing to more carbon emission reduction than carbon emission (Bastianoni et al., 2014). In summary, the result indicates that the development of PKS-AC-MgO on a larger scale is technically, economically, and environmentally feasible.

Table 4.19: Performance Indicator of PKS-AC-MgO

Performance Indicators	**Amount**
Annual PKS-AC-MgO production	231 tonne
Simple payback period	2.31 years
Annual processing of PKS waste	330 tonne
Actual selling price	USD 1,967/ tonne
Annual Carbon Emission	42.5 tons of CO_2 (tCO_2)
Annual GHG emission reduction	381.9 tons of CO_2 (tCO_2)

CHAPTER 5: CONCLUSION

5.1 Conclusion

This study had successfully developed three types of PKS- adsorbents via sustainable approach involving slow pyrolysis, KOH activation, and MgO impregnation. The physiochemical characterization of adsorbents had revealed that KOH activation effectively enhanced the porosity of PKS-AC, significantly increasing its surface area compared to PKS-Char and PKS-AC-MgO. Despite a marginal reduction in surface area due to MgO binding, PKS-AC-MgO exhibited superior pore volume and diameter. SEM and BET analysis provided insights into the surface morphology, microstructure and particle size distribution of the synthesized adsorbents, showing well-formed hexagonal crystal particles of PKS-AC-MgO for enhanced adsorption. Thermal stability was demonstrated by the minimal thermal degradation of PKS-Char, PKS-AC, and PKS-AC-MgO up to 500°C, affirming their potential for high-temperature applications.

The findings of this study indicated that PKS-AC-MgO showed the maximum adsorption capability among PKS-AC and PKS-Char at a temperature of 25°C and pressure of 5 bar. Additionally, PKS-AC-MgO also showed superior adsorption rates at both lower and higher temperatures indicating its potential for effective CO_2 capture even at elevated temperatures. The inverse relationship observed between CO_2 adsorption capacity and temperature highlighted the exothermic nature of the adsorption process. Meanwhile the positive correlation between CO_2 adsorption and pressure emphasized the pressure-dependent nature of the adsorption mechanism.

The comprehensive isotherm analysis also showed excellent fit of Langmuir isotherms for PKS-Char and PKS-AC-MgO suggested the formation of monolayer CO_2 adsorption. The negative ΔS_o values indicated the transition of CO_2 molecules from a disordered to an ordered state on the adsorbent's surface during the adsorption process.

Moreover, the negative ΔG values at low temperatures indicated that CO_2 adsorption onto PKS-Char and PKS-AC-MgO was spontaneous. Remarkably, this analysis further highlighted the coexistence of physisorption and chemisorption processes in the synthesized adsorbents. By incorporating a practical aspect into the study, the economic analysis demonstrated that PKS-AC-MgO exhibited a specific cost of $1,977 per tonne which is 20% lower than the prevailing market price of $2,400 per tonne of commercial AC, thus highlighting the economic feasibility of the adsorbent. In the context of sustainability, the synthesis of PKS-based AC had led to a decrease of 381.9 tCO_2 in greenhouse gas emissions. In summary, this is strategy holds a significant potential for addressing CO_2 capture challenges and finding sustainable solutions for environmental concerns. This innovative approach, centered on circular economy principles and sustainable utilization of biomass resources, not only enhances the value of biomass residues but also contributes to mitigating greenhouse gas emissions.

5.2 Recommendation for Future Studies

Based on the findings of this study, the following recommendations can be used to improve future research.

1. Incorporating machine learning techniques into the present study provide holistic understanding of CO_2 adsorption mechanisms, optimize experimental conditions, and potentially discover novel insights that might not be evident through traditional approaches alone.
2. Scale-up studies are essential to evaluate the feasibility of using PKS-Char, PKS-AC, and PKS-AC-MgO in large-scale CO_2 capture applications.
3. Investigate potential synergistic effects when using PKS-Char, PKS-AC, and PKS-AC-MgO in combination with other CO_2 capture technologies, such as membrane

separation or absorption processes. Combining different capture methods can enhance overall efficiency and CO_2 removal capabilities.

4. Investigate the potential of PKS-Char, PKS-AC, and PKS-AC-MgO in adsorbing other pollutants, such as nitrogen oxides (NO_x) or sulfur dioxide (SO_2). Understanding their multi-pollutant adsorption capabilities can lead to more versatile and efficient pollution control technologies.

5.3 Output of This Study

A review paper had been published in the Journal of Industrial and Engineering Chemistry, which is a journal ranked by the ISI (Impact Factor: 6.1). A conference paper had been presented in International Congress on Pure & Applied Chemistry Kota Kinabalu (ICPAC KK) and waiting for the acceptance. Two technical papers that developed based on the objectives of the study are under review in Tier 1 and Tier 2, ISI ranked journals.

5.4 Knowledge Contribution

The study presents novel synthesis methods for preparing PKS- adsorbent, involve slow pyrolysis, KOH activation, and MgO impregnation, respectively. The combination of these techniques offers new avenues for producing efficient and sustainable CO_2 adsorbents from agricultural biomass residues.

Moreover, the adsorption mechanisms of CO_2 on the different adsorbents using isotherm analysis have been evaluated. The successful impregnation of PKS-AC with MgO to produce PKS-AC-MgO demonstrates the feasibility of metal oxide modification to enhance CO_2 adsorption capacity. This knowledge opens up possibilities for tailoring the properties of adsorbents to optimize their performance for specific CO_2 capture scenarios. The study examines the thermal stability and regenerability of the adsorbents,

providing crucial information for designing cyclic CO_2 capture processes. Understanding the stability of these adsorbents under high-temperature conditions is essential for practical industrial applications. In summary, the knowledge contribution of this study lies in its systematic exploration of PKS- adsorbents with KOH activation and MgO impregnation for CO_2 capture These findings pave the way for the development of sustainable and efficient CO_2 capture technologies using biomass-based adsorbents.

REFERENCES

Abanades, J. C., Anthony, E. J., Wang, J., & Oakey, J. E. (2005). Fluidized bed combustion systems integrating CO2 capture with CaO. *Environ Sci Technol, 39*(8), 2861-2866. doi:10.1021/es0496221

Abd, A. A., Naji, S. Z., Hashim, A. S., & Othman, M. R. (2020). Carbon dioxide removal through physical adsorption using carbonaceous and non-carbonaceous adsorbents: A review. *Journal of Environmental Chemical Engineering, 8*(5), 104142. doi:https://doi.org/10.1016/j.jece.2020.104142

Abdedayem, A., Guiza, M., & Ouederni, A. (2015). Copper supported on porous activated carbon obtained by wetness impregnation: Effect of preparation conditions on the ozonation catalyst's characteristics. *Comptes Rendus Chimie, 18*(1), 100-109. doi:https://doi.org/10.1016/j.crci.2014.07.011

Abuelnoor, N., AlHajaj, A., Khaleel, M., Vega, L. F., & Abu-Zahra, M. R. M. (2021). Activated carbons from biomass-based sources for CO2 capture applications. *Chemosphere, 282*, 131111. doi:10.1016/j.chemosphere.2021.131111

Adani, F., Papa, G., Schievano, A., Cardinale, G., D'Imporzano, G., & Tambone, F. (2011). Nanoscale structure of the cell wall protecting cellulose from enzyme attack. *Environ Sci Technol, 45*(3), 1107-1113. doi:10.1021/es1020263

Aguayo-Villarreal, I. A., Bonilla-Petriciolet, A., & Muñiz-Valencia, R. (2017). Preparation of activated carbons from pecan nutshell and their application in the antagonistic adsorption of heavy metal ions. *Journal of Molecular Liquids, 230*, 686-695. doi:https://doi.org/10.1016/j.molliq.2017.01.039

Ahmed, M. B., Hasan Johir, M. A., Zhou, J. L., Ngo, H. H., Nghiem, L. D., Richardson, C., . . . Bryant, M. R. (2019). Activated carbon preparation from biomass feedstock: Clean production and carbon dioxide adsorption. *Journal of Cleaner Production, 225*, 405-413. doi:https://doi.org/10.1016/j.jclepro.2019.03.342

Al-Amrani, W. A., Lim, P. E., Seng, C. E., & Ngah, W. S. (2012). Bioregeneration of mono-amine modified silica and granular activated carbon loaded with Acid Orange 7 in batch system. *Bioresour Technol, 118*, 633-637. doi:10.1016/j.biortech.2012.05.090

Al-Rowaili, F. N., Zahid, U., Onaizi, S., Khaled, M., Jamal, A., & Al-Mutairi, E. M. (2021). A review for Metal-Organic Frameworks (MOFs) utilization in capture and conversion of carbon dioxide into valuable products. *Journal of CO2 Utilization, 53*, 101715. doi:https://doi.org/10.1016/j.jcou.2021.101715

Al Mesfer, M. K. (2020). Synthesis and characterization of high-performance activated carbon from walnut shell biomass for CO2 capture. *Environ Sci Pollut Res Int, 27*(13), 15020-15028. doi:10.1007/s11356-020-07934-x

Aladin, A., Modding, B., Syarif, T., & Dewi, F. C. (2021). Effect of nitrogen gas flowing continuously into the pyrolysis reactor for simultaneous production of charcoal and liquid smoke. *Journal of Physics: Conference Series, 1763*(1), 012020. doi:10.1088/1742-6596/1763/1/012020

Alfe, M., Policicchio, A., Lisi, L., & Gargiulo, V. (2021). Solid sorbents for CO2 and CH4 adsorption: The effect of metal organic framework hybridization with graphene-like layers on the gas sorption capacities at high pressure. *Renewable and Sustainable Energy Reviews, 141*, 110816. doi:https://doi.org/10.1016/j.rser.2021.110816

Alkadhem, A. M., Elgzoly, M. A. A., Alshami, A., & Onaizi, S. A. (2021). Kinetics of CO2 capture by novel amine-functionalized magnesium oxide adsorbents.

Colloids and Surfaces A: Physicochemical and Engineering Aspects, 616, 126258. doi:https://doi.org/10.1016/j.colsurfa.2021.126258

Alnouss, A., Shahbaz, M., McKay, G., & Al-Ansari, T. (2022). Bio-methanol production from palm wastes steam gasification with application of CaO for CO2 capture: Sensitivity and techno-economic-environmental analysis. *Journal of Cleaner Production, 341*, 130849. doi:10.1016/j.jclepro.2022.130849

Alves, J. L. F., da Silva, J. C. G., Mumbach, G. D., Domenico, M. D., Bolzan, A., Machado, R. A. F., & Marangoni, C. (2022). Evaluating the bioenergy potential of cupuassu shell through pyrolysis kinetics, thermodynamic parameters of activation, and evolved gas analysis with TG/FTIR technique. *Thermochimica Acta, 711*, 179187. doi:https://doi.org/10.1016/j.tca.2022.179187

Ammendola, P., Raganati, F., & Chirone, R. (2017). CO2 adsorption on a fine activated carbon in a sound assisted fluidized bed: Thermodynamics and kinetics. *Chemical Engineering Journal, 322*, 302-313. doi:https://doi.org/10.1016/j.cej.2017.04.037

An, L., Liu, S., Wang, L., Wu, J., Wu, Z., Ma, C., . . . Hu, X. (2019). Novel Nitrogen-Doped Porous Carbons Derived from Graphene for Effective CO2 Capture. *Industrial & Engineering Chemistry Research, 58*(8), 3349-3358. doi:10.1021/acs.iecr.8b06122

An, Q., Miao, Y., Zhao, B., Li, Z., & Zhu, S. (2020). An alkali modified biochar for enhancing Mn2+ adsorption: Performance and chemical mechanism. *Materials Chemistry and Physics, 248*, 122895. doi:https://doi.org/10.1016/j.matchemphys.2020.122895

anak Erison, A. E., Tan, Y. H., Mubarak, N. M., Kansedo, J., Khalid, M., Abdullah, M. O., & Ghasemi, M. (2022). Life cycle assessment of biodiesel production by using impregnated magnetic biochar derived from waste palm kernel shell. *Environmental Research, 214*, 114149. doi:https://doi.org/10.1016/j.envres.2022.114149

Andirova, D., Lei, Y., Zhao, X., & Choi, S. (2015). Functionalization of Metal-Organic Frameworks for Enhanced Stability under Humid Carbon Dioxide Capture Conditions. *ChemSusChem, 8*(20), 3405-3409. doi:10.1002/cssc.201500580

Araújo, C. S. T., Almeida, I. L. S., Rezende, H. C., Marcionilio, S. M. L. O., Léon, J. J. L., & de Matos, T. N. (2018). Elucidation of mechanism involved in adsorption of Pb(II) onto lobeira fruit (Solanum lycocarpum) using Langmuir, Freundlich and Temkin isotherms. *Microchemical Journal, 137*, 348-354. doi:https://doi.org/10.1016/j.microc.2017.11.009

Asadi-Sangachini, Z., Galangash, M. M., Younesi, H., & Nowrouzi, M. (2019). The feasibility of cost-effective manufacturing activated carbon derived from walnut shells for large-scale CO2 capture. *Environ Sci Pollut Res Int, 26*(26), 26542-26552. doi:10.1007/s11356-019-05842-3

Baby, R., Hussein, M. Z., Zainal, Z., & Abdullah, A. H. (2023). Preparation of Functionalized Palm Kernel Shell Bio-adsorbent for the treatment of heavy metal-contaminated water. *Journal of Hazardous Materials Advances, 10*, 100253. doi:https://doi.org/10.1016/j.hazadv.2023.100253

Balou, S., Babak, S. E., & Priye, A. (2020). Synergistic Effect of Nitrogen Doping and Ultra-Microporosity on the Performance of Biomass and Microalgae-Derived Activated Carbons for CO2 Capture. *ACS Appl Mater Interfaces, 12*(38), 42711-42722. doi:10.1021/acsami.0c10218

Baltrusaitis, J., Hatch, C., & Orlando, R. (2012). Periodic DFT study of acidic trace atmospheric gas molecule adsorption on Ca- and Fe-doped MgO(001) surface basic sites. *J Phys Chem A, 116*(30), 7950-7958. doi:10.1021/jp3041988

Barber, P. S., Griggs, C. S., Gurau, G., Liu, Z., Li, S., Li, Z., . . . Rogers, R. D. (2013). Coagulation of chitin and cellulose from 1-ethyl-3-methylimidazolium acetate ionic-liquid solutions using carbon dioxide. *Angew Chem Int Ed Engl, 52*(47), 12350-12353. doi:10.1002/anie.201304604

Başakçılardan Kabakcı, S., & Baran, S. S. (2019). Hydrothermal carbonization of various lignocellulosics: Fuel characteristics of hydrochars and surface characteristics of activated hydrochars. *Waste Management, 100*, 259-268. doi:https://doi.org/10.1016/j.wasman.2019.09.021

Basheer, A. O., Hanafiah, M. M., Alsaadi, M. A., Al-Douri, Y., & Al-Raad, A. A. (2021). Synthesis and optimization of high surface area mesoporous date palm fiber-based nanostructured powder activated carbon for aluminum removal. *Chinese Journal of Chemical Engineering, 32*, 472-484. doi:https://doi.org/10.1016/j.cjche.2020.09.071

Bastianoni, S., Marchi, M., Caro, D., Casprini, P., & Pulselli, F. M. (2014). The connection between 2006 IPCC GHG inventory methodology and ISO 14064-1 certification standard – A reference point for the environmental policies at sub-national scale. *Environmental Science & Policy, 44*, 97-107. doi:https://doi.org/10.1016/j.envsci.2014.07.015

Bazan-Wozniak, A., Nowicki, P., & Pietrzak, R. (2021). Removal of NO2 from gas stream by activated bio-carbons from physical activation of residue of supercritical extraction of hops. *Chemical Engineering Research and Design, 166*, 67-73. doi:https://doi.org/10.1016/j.cherd.2020.11.021

Benedetti, V., Cordioli, E., Patuzzi, F., & Baratieri, M. (2019). CO2 Adsorption study on pure and chemically activated chars derived from commercial biomass gasifiers. *Journal of CO2 Utilization, 33*, 46-54. doi:https://doi.org/10.1016/j.jcou.2019.05.008

Birgani, P. M., Ranjbar, N., Abdullah, R. C., Wong, K. T., Lee, G., Ibrahim, S., . . . Jang, M. (2016). An efficient and economical treatment for batik textile wastewater containing high levels of silicate and organic pollutants using a sequential process of acidification, magnesium oxide, and palm shell-based activated carbon application. *Journal of Environmental Management, 184*, 229-239. doi:https://doi.org/10.1016/j.jenvman.2016.09.066

Bisinella, V., Hulgaard, T., Riber, C., Damgaard, A., & Christensen, T. H. (2021). Environmental assessment of carbon capture and storage (CCS) as a post-treatment technology in waste incineration. *Waste Management, 128*, 99-113. doi:https://doi.org/10.1016/j.wasman.2021.04.046

Bond, J. Q., Alonso, D. M., West, R. M., & Dumesic, J. A. (2010). gamma-Valerolactone ring-opening and decarboxylation over SiO2/Al2O3 in the presence of water. *Langmuir, 26*(21), 16291-16298. doi:10.1021/la101424a

Boujibar, O., Souikny, A., Ghamouss, F., Achak, O., Dahbi, M., & Chafik, T. (2018). CO2 capture using N-containing nanoporous activated carbon obtained from argan fruit shells. *Journal of Environmental Chemical Engineering, 6*(2), 1995-2002. doi:https://doi.org/10.1016/j.jece.2018.03.005

Bridgwater, A. V. (2012). Review of fast pyrolysis of biomass and product upgrading. *Biomass and Bioenergy, 38*, 68-94. doi:https://doi.org/10.1016/j.biombioe.2011.01.048

Caglar, B., Niemantsverdriet, J. W., & Weststrate, C. J. (2016). Modeling the surface chemistry of biomass model compounds on oxygen-covered Rh(100). *Phys Chem Chem Phys, 18*(34), 23888-23903. doi:10.1039/c6cp03891c

Cai, Y., Liu, W., Sun, Z., Yang, Y., & Li, P. (2022). Granulation of alkaline metal nitrate promoted MgO adsorbents and the low-concentration CO2 capture

performance in the fixed bed adsorber. *Journal of CO2 Utilization, 61*, 102047. doi:https://doi.org/10.1016/j.jcou.2022.102047
Cao, Y., Song, F., Zhao, Y., & Zhong, Q. (2013). Capture of carbon dioxide from flue gas on TEPA-grafted metal-organic framework Mg2(dobdc). *J Environ Sci (China), 25*(10), 2081-2087. doi:10.1016/s1001-0742(12)60267-8
Cha, J. S., Choi, J.-C., Ko, J. H., Park, Y.-K., Park, S. H., Jeong, K.-E., . . . Jeon, J.-K. (2010). The low-temperature SCR of NO over rice straw and sewage sludge derived char. *Chemical Engineering Journal, 156*(2), 321-327. doi:https://doi.org/10.1016/j.cej.2009.10.027
Chamas, A., Qi, L., Mehta, H. S., Sears, J. A., Scott, S. L., Walter, E. D., & Hoyt, D. W. (2019). High temperature/pressure MAS-NMR for the study of dynamic processes in mixed phase systems. *Magn Reson Imaging, 56*, 37-44. doi:10.1016/j.mri.2018.09.026
Chammingkwan, P., Mai, L. T. T., Ikeda, T., & Mohan, P. (2021). Nanostructured magnesium oxide microspheres for efficient carbon dioxide capture. *Journal of CO2 Utilization, 51*, 101652. doi:https://doi.org/10.1016/j.jcou.2021.101652
Chang, C.-W., Kao, Y.-H., Shen, P.-H., Kang, P.-C., & Wang, C.-Y. (2020). Nanoconfinement of metal oxide MgO and ZnO in zeolitic imidazolate framework ZIF-8 for CO2 adsorption and regeneration. *Journal of Hazardous Materials, 400*, 122974. doi:https://doi.org/10.1016/j.jhazmat.2020.122974
Chen, C., Kim, J., Yang, D.-A., & Ahn, W.-S. (2011). Carbon dioxide adsorption over zeolite-like metal organic frameworks (ZMOFs) having a sod topology: Structure and ion-exchange effect. *Chemical Engineering Journal, 168*(3), 1134-1139. doi:https://doi.org/10.1016/j.cej.2011.01.096
Chen, C., Qi, Q., Huang, D., Zeng, T., Bu, X., Huang, Y., & Huang, H. (2021). Effect of additive mixture on microwave-assisted catalysis pyrolysis of microalgae. *Energy, 229*, 120752. doi:https://doi.org/10.1016/j.energy.2021.120752
Chen, J., Yang, J., Hu, G., Hu, X., Li, Z., Shen, S., . . . Fan, M. (2016). Enhanced CO2 Capture Capacity of Nitrogen-Doped Biomass-Derived Porous Carbons. *ACS Sustainable Chemistry & Engineering, 4*(3), 1439-1445. doi:10.1021/acssuschemeng.5b01425
Chen, K., Ng, K. H., Cheng, C. K., Cheng, Y. W., Chong, C. C., Vo, D. N., . . . Ismail, M. H. (2022). Biomass-derived carbon-based and silica-based materials for catalytic and adsorptive applications- An update since 2010. *Chemosphere, 287*(Pt 2), 132222. doi:10.1016/j.chemosphere.2021.132222
Chen, S., Qi, G., Ma, G., & Zhao, X. (2020). Biochar amendment controlled bacterial wilt through changing soil chemical properties and microbial community. *Microbiological Research, 231*, 126373. doi:https://doi.org/10.1016/j.micres.2019.126373
Cheng, C., Liu, H., Dai, P., Shen, X., Zhang, J., Zhao, T., & Zhu, Z. (2016). Microwave-assisted preparation and characterization of mesoporous activated carbon from mushroom roots by phytic acid (C6H18O24P6) activation. *Journal of the Taiwan Institute of Chemical Engineers, 67*, 532-537. doi:https://doi.org/10.1016/j.jtice.2016.08.032
Chiang, Y.-C., & Juang, R.-S. (2017). Surface modifications of carbonaceous materials for carbon dioxide adsorption: A review. *Journal of the Taiwan Institute of Chemical Engineers, 71*, 214-234. doi:https://doi.org/10.1016/j.jtice.2016.12.014
Cho, D. W., Cho, S. H., Song, H., & Kwon, E. E. (2015). Carbon dioxide assisted sustainability enhancement of pyrolysis of waste biomass: A case study with

spent coffee ground. *Bioresour Technol, 189*, 1-6. doi:10.1016/j.biortech.2015.04.002

Chong, T. Y., Cheah, S. A., Ong, C. T., Wong, L. Y., Goh, C. R., Tan, I. S., . . . Lim, S. (2020). Techno-economic evaluation of third-generation bioethanol production utilizing the macroalgae waste: A case study in Malaysia. *Energy, 210*, 118491. doi:https://doi.org/10.1016/j.energy.2020.118491

Creamer, A. E., Gao, B., & Wang, S. (2016). Carbon dioxide capture using various metal oxyhydroxide–biochar composites. *Chemical Engineering Journal, 283*, 826-832. doi:https://doi.org/10.1016/j.cej.2015.08.037

Creamer, A. E., Gao, B., Zimmerman, A., & Harris, W. (2018). Biomass-facilitated production of activated magnesium oxide nanoparticles with extraordinary CO2 capture capacity. *Chemical Engineering Journal, 334*, 81-88. doi:https://doi.org/10.1016/j.cej.2017.10.035

Crone, M., & Türk, M. (2022). Thermodynamics of adsorption of carbon dioxide on different metal oxides at temperatures from 313 to 353 K and pressures up to 25 MPa. *The Journal of Supercritical Fluids, 182*, 105461. doi:https://doi.org/10.1016/j.supflu.2021.105461

Dai, Z., Noble, R. D., Gin, D. L., Zhang, X., & Deng, L. (2016). Combination of ionic liquids with membrane technology: A new approach for CO2 separation. *Journal of Membrane Science, 497*, 1-20. doi:https://doi.org/10.1016/j.memsci.2015.08.060

Danish, M., Parthasarthy, V., & Al Mesfer, M. K. (2021). Comparative Study of CO2 Capture by Adsorption in Sustainable Date Pits-Derived Porous Activated Carbon and Molecular Sieve. *Int J Environ Res Public Health, 18*(16). doi:10.3390/ijerph18168497

Darabi, J., Ghiasvand, A., & Haddad, P. R. (2021). Biomass-derived carbon nanospheres decorated by manganese oxide nanosheets, intercalated into polypyrrole, as an inside-needle capillary adsorption trap sorbent for the analysis of linear alkylbenzenes. *Talanta, 233*, 122583. doi:10.1016/j.talanta.2021.122583

Daub, C., Patey, G., Jack, D., & Sallabi, A. (2006). Monte Carlo simulations of the adsorption of CO2 on the MgO(100) surface. *The Journal of chemical physics, 124*, 114706. doi:10.1063/1.2171277

de Lorena Diniz Chaves, G., Siman, R. R., Ribeiro, G. M., & Chang, N.-B. (2021). Synergizing environmental, social, and economic sustainability factors for refuse derived fuel use in cement industry: A case study in Espirito Santo, Brazil. *Journal of Environmental Management, 288*, 112401. doi:https://doi.org/10.1016/j.jenvman.2021.112401

Dhiman, N., & Sharma, N. (2019). Removal of pharmaceutical drugs from binary mixtures by use of ZnO nanoparticles: (Competitive adsorption of drugs). *Environmental Technology & Innovation, 15*, 100392. doi:https://doi.org/10.1016/j.eti.2019.100392

Dissanayake, P. D., You, S., Igalavithana, A. D., Xia, Y., Bhatnagar, A., Gupta, S., . . . Ok, Y. S. (2020). Biochar-based adsorbents for carbon dioxide capture: A critical review. *Renewable and Sustainable Energy Reviews, 119*, 109582. doi:https://doi.org/10.1016/j.rser.2019.109582

Duan, X., Zhang, C., Srinivasakannan, C., & Wang, X. (2017). Waste walnut shell valorization to iron loaded biochar and its application to arsenic removal. *Resource-Efficient Technologies, 3*(1), 29-36. doi:https://doi.org/10.1016/j.reffit.2017.01.001

Duran-Jimenez, G., Kostas, E. T., Stevens, L. A., Meredith, W., Erans, M., Hernandez-Montoya, V., . . . Binner, E. (2021). Green and simple approach for low-cost bioproducts preparation and CO2 capture. *Chemosphere, 279*, 130512. doi:10.1016/j.chemosphere.2021.130512

Ekanayake, U. G. M., Rahmati, S., Zhou, R., Zhou, R., Cullen, P. J., O'Mullane, A. P., . . . Ostrikov, K. (2021). Power-to-decarbonization: Mesoporous carbon-MgO nanohybrid derived from plasma-activated seawater salt-loaded biomass for efficient CO2 capture. *Journal of CO2 Utilization, 53*, 101711. doi:https://doi.org/10.1016/j.jcou.2021.101711

Ello, A. S., de Souza, L. K. C., Trokourey, A., & Jaroniec, M. (2013a). Coconut shell-based microporous carbons for CO2 capture. *Microporous and Mesoporous Materials, 180*, 280-283. doi:https://doi.org/10.1016/j.micromeso.2013.07.008

Ello, A. S., de Souza, L. K. C., Trokourey, A., & Jaroniec, M. (2013b). Development of microporous carbons for CO2 capture by KOH activation of African palm shells. *Journal of CO2 Utilization, 2*, 35-38. doi:https://doi.org/10.1016/j.jcou.2013.07.003

Fallah, Z., Zare, E. N., Ghomi, M., Ahmadijokani, F., Amini, M., Tajbakhsh, M., . . . Varma, R. S. (2021). Toxicity and remediation of pharmaceuticals and pesticides using metal oxides and carbon nanomaterials. *Chemosphere, 275*, 130055. doi:https://doi.org/10.1016/j.chemosphere.2021.130055

Fodah, A. E. M., Ghosal, M. K., & Behera, D. (2021). Microwave-assisted pyrolysis of agricultural residues: current scenario, challenges, and future direction. *International Journal of Environmental Science and Technology*. doi:10.1007/s13762-020-03099-9

Galinsky, N., Huang, Y., Shafiefarhood, A., & Li, F. (2013). Iron Oxide with Facilitated O2– Transport for Facile Fuel Oxidation and CO2 Capture in a Chemical Looping Scheme. *ACS Sustainable Chemistry & Engineering, 1*, 364–373. doi:10.1021/sc300177j

Gan, F., Wang, B., Jin, Z., Xie, L., Dai, Z., Zhou, T., & Jiang, X. (2021). From typical silicon-rich biomass to porous carbon-zeolite composite: A sustainable approach for efficient adsorption of CO2. *Sci Total Environ, 768*, 144529. doi:10.1016/j.scitotenv.2020.144529

Gao, L., Li, Z., Yi, W., Li, Y., Zhang, P., Zhang, A., & Wang, L. (2021). Impacts of pyrolysis temperature on lead adsorption by cotton stalk-derived biochar and related mechanisms. *Journal of Environmental Chemical Engineering*, 105602. doi:https://doi.org/10.1016/j.jece.2021.105602

Gao, Q., Ni, L., He, Y., Hou, Y., Hu, W., & Liu, Z. (2022). Effect of hydrothermal pretreatment on deashing and pyrolysis characteristics of bamboo shoot shells. *Energy, 247*, 123510. doi:https://doi.org/10.1016/j.energy.2022.123510

Gao, W., Zhou, T., & Wang, Q. (2018). Controlled synthesis of MgO with diverse basic sites and its CO2 capture mechanism under different adsorption conditions. *Chemical Engineering Journal, 336*, 710-720. doi:https://doi.org/10.1016/j.cej.2017.12.025

Gao, Y., Yue, Q., Gao, B., & Li, A. (2020). Insight into activated carbon from different kinds of chemical activating agents: A review. *Science of The Total Environment, 746*, 141094. doi:https://doi.org/10.1016/j.scitotenv.2020.141094

Gayathiri, M., Pulingam, T., Lee, K. T., & Sudesh, K. (2022). Activated carbon from biomass waste precursors: Factors affecting production and adsorption mechanism. *Chemosphere, 294*, 133764. doi:https://doi.org/10.1016/j.chemosphere.2022.133764

Ghodake, G. S., Shinde, S. K., Kadam, A. A., Saratale, R. G., Saratale, G. D., Kumar, M., . . . Kim, D.-Y. (2021). Review on biomass feedstocks, pyrolysis mechanism and physicochemical properties of biochar: State-of-the-art framework to speed up vision of circular bioeconomy. *Journal of Cleaner Production, 297*, 126645. doi:https://doi.org/10.1016/j.jclepro.2021.126645

Ghosh, S., Sarathi, R., & Ramaprabhu, S. (2019). Magnesium oxide modified nitrogen-doped porous carbon composite as an efficient candidate for high pressure carbon dioxide capture and methane storage. *Journal of Colloid and Interface Science, 539*, 245-256. doi:https://doi.org/10.1016/j.jcis.2018.12.063

Gil, A., & Grange, P. (1996). Application of the Dubinin-Radushkevich and Dubinin-Astakhov equations in the characterization of microporous solids. *Colloids and Surfaces A: Physicochemical and Engineering Aspects, 113*(1), 39-50. doi:https://doi.org/10.1016/0927-7757(96)81455-5

Goel, C., Mohan, S., & Dinesha, P. (2021). CO2 capture by adsorption on biomass-derived activated char: A review. *Sci Total Environ, 798*, 149296. doi:10.1016/j.scitotenv.2021.149296

González, A. S., Plaza, M. G., Rubiera, F., & Pevida, C. (2013). Sustainable biomass-based carbon adsorbents for post-combustion CO2 capture. *Chemical Engineering Journal, 230*, 456-465. doi:https://doi.org/10.1016/j.cej.2013.06.118

Gosu, V., Dhakar, A., Sikarwar, P., Kumar, U. K. A., Subbaramaiah, V., & Zhang, T. C. (2018). Wet peroxidation of resorcinol catalyzed by copper impregnated granular activated carbon. *Journal of Environmental Management, 223*, 825-833. doi:https://doi.org/10.1016/j.jenvman.2018.06.093

Grande, C. A., Kvamsdal, H., Mondino, G., & Blom, R. (2017). Development of Moving Bed Temperature Swing Adsorption (MBTSA) Process for Post-combustion CO2 Capture: Initial Benchmarking in a NGCC Context. *Energy Procedia, 114*, 2203-2210. doi:https://doi.org/10.1016/j.egypro.2017.03.1357

Guo, Y., Tan, C., Wang, P., Sun, J., Li, W., Zhao, C., & Lu, P. (2019). Magnesium-based basic mixtures derived from earth-abundant natural minerals for CO2 capture in simulated flue gas. *Fuel, 243*, 298-305. doi:https://doi.org/10.1016/j.fuel.2019.01.108

Guo, Y., Zhao, C., Chen, X., & Li, C. (2015). CO2 capture and sorbent regeneration performances of some wood ash materials. *Applied Energy, 137*, 26-36. doi:https://doi.org/10.1016/j.apenergy.2014.09.086

Guo, Z., Xiong, J., Sohail, M. I., & Yang, D. (2021). Investigating phosphorus release from lignite-based activated rock phosphate through TG-FTIR analysis. *Environmental Technology & Innovation, 23*, 101787. doi:https://doi.org/10.1016/j.eti.2021.101787

Han, W., Fang, J., Liu, Z., & Tang, J. (2016). Techno-economic evaluation of a combined bioprocess for fermentative hydrogen production from food waste. *Bioresource Technology, 202*, 107-112. doi:https://doi.org/10.1016/j.biortech.2015.11.072

Handayani, H., Ningsih, Y., & Meriansyah, M. (2019). Effects of carbonization duration on the characteristics of bio-coal briquettes (coal and cane waste). *IOP Conference Series: Materials Science and Engineering, 478*, 012027. doi:10.1088/1757-899X/478/1/012027

He, J., Mei, J., Bao, Z., & Wilcox, J. (2014). Facile Synthesis of Nitrogen-doped Porous Carbon for Selective CO2 Capture. *Energy Procedia, 63*. doi:10.1016/j.egypro.2014.11.233

Hidayu, A. R., & Muda, N. (2016). Preparation and Characterization of Impregnated Activated Carbon from Palm Kernel Shell and Coconut Shell for CO2 Capture. *Procedia Engineering, 148*, 106-113. doi:https://doi.org/10.1016/j.proeng.2016.06.463

Ho, K., Jin, S., Zhong, M., Vu, A.-T., & Lee, C.-H. (2017). Sorption capacity and stability of mesoporous magnesium oxide in post-combustion CO2 capture. *Materials Chemistry and Physics, 198*, 154-161. doi:https://doi.org/10.1016/j.matchemphys.2017.06.002

Ho, P. H., Lofty, V., Basta, A., & Trens, P. (2021). Designing microporous activated carbons from biomass for carbon dioxide adsorption at ambient temperature. A comparison between bagasse and rice by-products. *Journal of Cleaner Production, 294*, 126260. doi:https://doi.org/10.1016/j.jclepro.2021.126260

Hong, S.-M., Jang, E., Dysart, A., Pol, V., & Lee, K. (2016). CO2 Capture in the Sustainable Wheat-Derived Activated Microporous Carbon Compartments. *Scientific Reports, 6*, 34590. doi:10.1038/srep34590

Hongbo, D., Deng, F., Kommalapati, R. R., & Amarasekara, A. S. (2020). Iron based catalysts in biomass processing. *Renewable and Sustainable Energy Reviews, 134*, 110292. doi:https://doi.org/10.1016/j.rser.2020.110292

Hosseini, S., Bayesti, I., Marahel, E., Eghbali Babadi, F., Chuah Abdullah, L., & Choong, T. S. Y. (2015). Adsorption of carbon dioxide using activated carbon impregnated with Cu promoted by zinc. *Journal of the Taiwan Institute of Chemical Engineers, 52*, 109-117. doi:https://doi.org/10.1016/j.jtice.2015.02.015

Hou, Z.-q., Luo, M.-y., Yang, Y.-t., Zhou, J.-c., Liu, L.-c., & Cai, J.-j. (2021). Algae-based carbons: Design, preparation and recent advances in their use in energy storage, catalysis and adsorption. *New Carbon Materials, 36*(2), 278-303. doi:https://doi.org/10.1016/S1872-5805(21)60020-3

Hu, Y., Sun, B., Wu, S., Feng, H., Gao, M., Zhang, B., & Liu, Y. (2021). After-effects of straw and straw-derived biochar application on crop growth, yield, and soil properties in wheat (Triticum aestivum L.) -maize (Zea mays L.) rotations: A four-year field experiment. *Science of The Total Environment, 780*, 146560. doi:https://doi.org/10.1016/j.scitotenv.2021.146560

Huang, F., Li, D., Wang, L., Zhang, K., Fu, L., Guo, Z., . . . Li, B. (2021). Rational introduction of nitridizing agent to hydrothermal carbonization for enhancing CO2 capture performance of tobacco stalk-based porous carbons. *Journal of Analytical and Applied Pyrolysis*, 105047. doi:https://doi.org/10.1016/j.jaap.2021.105047

Huang, G.-g., Liu, Y.-f., Wu, X.-x., & Cai, J.-j. (2019). Activated carbons prepared by the KOH activation of a hydrochar from garlic peel and their CO2 adsorption performance. *New Carbon Materials, 34*(3), 247-257. doi:https://doi.org/10.1016/S1872-5805(19)60014-4

Huang, J., & Korzeniewski, C. (1999). A temperature controlled cell for in situ infrared spectroelectrochemical measurements and its use in the study of CO isothermal desorption. *Journal of Electroanalytical Chemistry, 471*(2), 146-150. doi:https://doi.org/10.1016/S0022-0728(99)00270-3

Huang, W.-H., Lee, D.-J., & Huang, C. (2021). Modification on biochars for applications: A research update. *Bioresource Technology, 319*, 124100. doi:https://doi.org/10.1016/j.biortech.2020.124100

Hurley, S., Li, H., & Xu, C. (2010). Effects of impregnated metal ions on air/CO2-gasification of woody biomass. *Bioresource Technology, 101*(23), 9301-9307. doi:https://doi.org/10.1016/j.biortech.2010.06.123

Iberahim, N., Sethupathi, S., Bashir, M. J. K., Kanthasamy, R., & Ahmad, T. (2022). Evaluation of oil palm fiber biochar and activated biochar for sulphur dioxide adsorption. *Sci Total Environ, 805*, 150421. doi:10.1016/j.scitotenv.2021.150421

Inagaki, M., Toyoda, M., Soneda, Y., & Morishita, T. (2018). Nitrogen-doped carbon materials. *Carbon, 132*, 104-140. doi:https://doi.org/10.1016/j.carbon.2018.02.024

Ismail, I. S., Rashidi, N. A., & Yusup, S. (2022). Production and characterization of bamboo-based activated carbon through single-step H3PO4 activation for CO2 capture. *Environ Sci Pollut Res Int, 29*(9), 12434-12440. doi:10.1007/s11356-021-15030-x

Jagodzińska, K., Zaini, I. N., Svanberg, R., Yang, W., & Jönsson, P. G. (2021). Pyrolysis of excavated waste from landfill mining: Characterisation of the process products. *Journal of Cleaner Production, 279*, 123541. doi:https://doi.org/10.1016/j.jclepro.2020.123541

Januszewicz, K., Kazimierski, P., Klein, M., Kardas, D., & Luczak, J. (2020). Activated Carbon Produced by Pyrolysis of Waste Wood and Straw for Potential Wastewater Adsorption. *Materials (Basel), 13*(9). doi:10.3390/ma13092047

Jasri, K., Abdulhameed, A. S., Jawad, A. H., Alothman, Z. A., Yousef, T. A., & Al Duaij, O. K. (2023). Mesoporous activated carbon produced from mixed wastes of oil palm frond and palm kernel shell using microwave radiation-assisted K2CO3 activation for methylene blue dye removal: Optimization by response surface methodology. *Diamond and Related Materials, 131*, 109581. doi:https://doi.org/10.1016/j.diamond.2022.109581

Jeguirim, M., Belhachemi, M., Limousy, L., & Bennici, S. (2018). Adsorption/reduction of nitrogen dioxide on activated carbons: Textural properties versus surface chemistry – A review. *Chemical Engineering Journal, 347*, 493-504. doi:https://doi.org/10.1016/j.cej.2018.04.063

Jhung, S. H., Khan, N. A., & Hasan, Z. (2012). Analogous porous metal–organic frameworks: synthesis, stability and application in adsorption. *CrystEngComm, 14*(21), 7099-7109. doi:10.1039/C2CE25760B

Ji, G., Yang, H., Memon, M. Z., Gao, Y., Qu, B., Fu, W., . . . Li, A. (2020). Recent advances on kinetics of carbon dioxide capture using solid sorbents at elevated temperatures. *Applied Energy, 267*, 114874. doi:https://doi.org/10.1016/j.apenergy.2020.114874

Jjagwe, J., Olupot, P. W., Menya, E., & Kalibbala, H. M. (2021). Synthesis and Application of Granular Activated Carbon from Biomass Waste Materials for Water Treatment: A Review. *Journal of Bioresources and Bioproducts, 6*(4), 292-322. doi:https://doi.org/10.1016/j.jobab.2021.03.003

Jung, S., Kim, J.-H., Lee, D.-J., Lin, K.-Y. A., Tsang, Y. F., Yoon, M.-H., & Kwon, E. E. (2021). Virtuous utilization of biochar and carbon dioxide in the thermochemical process of dairy cattle manure. *Chemical Engineering Journal, 416*, 129110. doi:https://doi.org/10.1016/j.cej.2021.129110

Kalaimurugan, D., Durairaj, K., Kumar, A. J., Senthilkumar, P., & Venkatesan, S. (2020). Novel preparation of fungal conidiophores biomass as adsorbent for removal of phosphorus from aqueous solution. *Environ Sci Pollut Res Int, 27*(17), 20757-20769. doi:10.1007/s11356-020-08307-0

Kandiah, M., Nilsen, M. H., Usseglio, S., Jakobsen, S., Olsbye, U., Tilset, M., . . . Lillerud, K. P. (2010). Synthesis and Stability of Tagged UiO-66 Zr-MOFs. *Chemistry of Materials, 22*(24), 6632-6640. doi:10.1021/cm102601v

Kang, I. J., Khan, N. A., Haque, E., & Jhung, S. H. (2011). Chemical and Thermal Stability of Isotypic Metal–Organic Frameworks: Effect of Metal Ions. *17*(23), 6437-6442. doi:https://doi.org/10.1002/chem.201100316

Kantarli, I. C., & Yanik, J. (2010). Activated carbon from leather shaving wastes and its application in removal of toxic materials. *J Hazard Mater, 179*(1-3), 348-356. doi:10.1016/j.jhazmat.2010.03.012

Karimi, M., Shirzad, M., Silva, J. A. C., & Rodrigues, A. E. (2022). Biomass/Biochar carbon materials for CO2 capture and sequestration by cyclic adsorption processes: A review and prospects for future directions. *Journal of CO2 Utilization, 57*, 101890. doi:https://doi.org/10.1016/j.jcou.2022.101890

Kasera, N., Kolar, P., & Hall, S. G. (2022). Nitrogen-doped biochars as adsorbents for mitigation of heavy metals and organics from water: a review. *Biochar, 4*(1), 17. doi:10.1007/s42773-022-00145-2

Kim, M. I., Seo, S. W., Kwak, C. H., Cho, J. H., & Im, J. S. (2021). The effect of oxidation on the physical activation of pitch: Crystal structure of carbonized pitch and textural properties of activated carbon after pitch oxidation. *Materials Chemistry and Physics, 267*, 124591. doi:https://doi.org/10.1016/j.matchemphys.2021.124591

Klusácek, K., Hudgins, R. R., & Silveston, P. L. (1989). Multiple steady states of an isothermal catalytic reaction with Elovich adsorption. *Chemical Engineering Science, 44*(10), 2377-2381. doi:https://doi.org/10.1016/0009-2509(89)85171-1

Kwak, J.-H., Islam, M. S., Wang, S., Messele, S. A., Naeth, M. A., El-Din, M. G., & Chang, S. X. (2019). Biochar properties and lead(II) adsorption capacity depend on feedstock type, pyrolysis temperature, and steam activation. *Chemosphere, 231*, 393-404. doi:https://doi.org/10.1016/j.chemosphere.2019.05.128

Kwiatkowski, M., Serafin, J., Booth, A. M., & Michalkiewicz, B. (2021). Computer Analysis of the Effect of Activation Temperature on the Microporous Structure Development of Activated Carbon Derived from Common Polypody. *Materials (Basel), 14*(11). doi:10.3390/ma14112951

Lahijani, P., Mohammadi, M., & Mohamed, A. R. (2018). Metal incorporated biochar as a potential adsorbent for high capacity CO2 capture at ambient condition. *Journal of CO2 Utilization, 26*, 281-293. doi:https://doi.org/10.1016/j.jcou.2018.05.018

Lee, T., Jung, S., Hong, J., Wang, C. H., Alessi, D. S., Lee, S. S., . . . Kwon, E. E. (2020). Using CO2 as an Oxidant in the Catalytic Pyrolysis of Peat Moss from the North Polar Region. *Environ Sci Technol, 54*(10), 6329-6343. doi:10.1021/acs.est.0c01862

Lemus, J., Martin-Martinez, M., Palomar, J., Gomez-Sainero, L., Gilarranz, M. A., & Rodriguez, J. J. (2012). Removal of chlorinated organic volatile compounds by gas phase adsorption with activated carbon. *Chemical Engineering Journal, 211-212*, 246-254. doi:https://doi.org/10.1016/j.cej.2012.09.021

Leus, K., Bogaerts, T., De Decker, J., Depauw, H., Hendrickx, K., Vrielinck, H., . . . Van Der Voort, P. (2016). Systematic study of the chemical and hydrothermal stability of selected “stable” Metal Organic Frameworks. *Microporous and Mesoporous Materials, 226*, 110-116. doi:https://doi.org/10.1016/j.micromeso.2015.11.055

Li, D., Ma, T., Zhang, R., Tian, Y., & Qiao, Y. (2015). Preparation of porous carbons with high low-pressure CO2 uptake by KOH activation of rice husk char. *Fuel, 139*, 68-70. doi:https://doi.org/10.1016/j.fuel.2014.08.027

Li, D., Tian, Y., Li, L., Li, J., & Zhang, H. (2015). Production of highly microporous carbons with large CO2 uptakes at atmospheric pressure by KOH activation of

peanut shell char. *Journal of Porous Materials, 22*(6), 1581-1588. doi:10.1007/s10934-015-0041-7

Li, F., Yi, H., Tang, X., Ning, P., Yu, Q., & Kang, D. (2010). Adsorption of carbon dioxide by coconut activated carbon modified with Cu/Ce. *Journal of Rare Earths, 28*, 334-337. doi:https://doi.org/10.1016/S1002-0721(10)60375-4

Li, L., Wang, J., Zhang, Z., Yang, Q., Yang, Y., Su, B., . . . Ren, Q. (2019). Inverse Adsorption Separation of CO2/C2H2 Mixture in Cyclodextrin-Based Metal-Organic Frameworks. *ACS Appl Mater Interfaces, 11*(2), 2543-2550. doi:10.1021/acsami.8b19590

Li, Q., Liu, S., Peng, W., Zhu, W., Wang, L., Chen, F., . . . Hu, X. (2020). Preparation of biomass-derived porous carbons by a facile method and application to CO2 adsorption. *Journal of the Taiwan Institute of Chemical Engineers, 116*, 128-136. doi:https://doi.org/10.1016/j.jtice.2020.11.001

Li, W., Huang, Y., Xie, J., Lang, L., Bu, W., Jiang, Y., . . . Yin, X. (2021). Assessment of Flammulina velutipes residue as potential fuels for co-combustion with pine sawdust from characteristics of combustion process, flue gases and ashes. *Journal of Analytical and Applied Pyrolysis*, 105156. doi:https://doi.org/10.1016/j.jaap.2021.105156

Li, Y., Han, K., Lin, W., Wan, M., Wang, Y., & Zhu, J. (2013). Fabrication of a new MgO/C sorbent for CO2 capture at elevated temperature. *J. Mater. Chem. A, 1*. doi:10.1039/C3TA12261A

Liao, T., Li, T., Su, X., Yu, X., Song, H., Zhu, Y., & Zhang, Y. (2018). La(OH)3-modified magnetic pineapple biochar as novel adsorbents for efficient phosphate removal. *Bioresource Technology, 263*, 207-213. doi:https://doi.org/10.1016/j.biortech.2018.04.108

Lin, Y.-L., & Zheng, N.-Y. (2021). Biowaste-to-biochar through microwave-assisted wet co-torrefaction of blending mango seed and passion shell with optoelectronic sludge. *Energy, 225*, 120213. doi:https://doi.org/10.1016/j.energy.2021.120213

Liu, C., Fu, C., Li, T., Zhang, P., Xia, Y., Wu, Y., . . . Gui, J. (2023). CO2 capture using biochar derived from conditioned sludge via pyrolysis. *Separation and Purification Technology, 314*, 123624. doi:https://doi.org/10.1016/j.seppur.2023.123624

Liu, H., Cheng, M., Liu, Y., Zhang, G., Li, L., Du, L., . . . Yang, X. (2022). Modified UiO-66 as photocatalysts for boosting the carbon-neutral energy cycle and solving environmental remediation issues. *Coordination Chemistry Reviews, 458*, 214428. doi:https://doi.org/10.1016/j.ccr.2022.214428

Liu, H., Liang, Z., Wang, S., Ma, N., & Chen, S. (2021). Synthesis and characterization of a thermosensitive solid amine biomass adsorbent for carbon dioxide adsorption. *J Environ Manage, 292*, 112722. doi:10.1016/j.jenvman.2021.112722

Liu, J., Jiang, J., Meng, Y., Aihemaiti, A., Xu, Y., Xiang, H., . . . Chen, X. (2020). Preparation, environmental application and prospect of biochar-supported metal nanoparticles: A review. *Journal of Hazardous Materials, 388*, 122026. doi:https://doi.org/10.1016/j.jhazmat.2020.122026

Liu, Q., Ning, L., Zheng, S., Tao, M., Shi, Y., & He, Y. (2013). Adsorption of carbon dioxide by MIL-101(Cr): regeneration conditions and influence of flue gas contaminants. *Sci Rep, 3*, 2916. doi:10.1038/srep02916

Liu, S., Ge, L., Gao, S., Zhuang, L., Zhu, Z., & Wang, H. (2017). Activated carbon derived from bio-waste hemp hurd and retted hemp hurd for CO2 adsorption.

Composites Communications, 5, 27-30. doi:https://doi.org/10.1016/j.coco.2017.06.002

Liu, W.-J., Jiang, H., Tian, K., Ding, Y.-W., & Yu, H.-Q. (2013). Mesoporous Carbon Stabilized MgO Nanoparticles Synthesized by Pyrolysis of MgCl2 Preloaded Waste Biomass for Highly Efficient CO2 Capture. *Environmental Science & Technology, 47*(16), 9397-9403. doi:10.1021/es401286p

Liu, W.-J., Jiang, H., & Yu, H.-Q. (2015). Development of Biochar-Based Functional Materials: Toward a Sustainable Platform Carbon Material. *Chemical Reviews, 115*(22), 12251-12285. doi:10.1021/acs.chemrev.5b00195

Luo, J.-P., Zhang, J., Yin, N., Wang, T.-P., Tan, Z.-C., Han, W., & Shi, Q. (2022). An experimental strategy for evaluating the energy performance of metal–organic framework-based carbon dioxide adsorbents. *Chemical Engineering Journal, 442*, 136210. doi:https://doi.org/10.1016/j.cej.2022.136210

Ma, M., Ying, H., Cao, F., Wang, Q., & Ai, N. (2020). Adsorption of congo red on mesoporous activated carbon prepared by CO2 physical activation. *Chinese Journal of Chemical Engineering, 28*(4), 1069-1076. doi:https://doi.org/10.1016/j.cjche.2020.01.016

Machado, L. M. M., Lütke, S. F., Perondi, D., Godinho, M., Oliveira, M. L. S., Collazzo, G. C., & Dotto, G. L. (2020). Treatment of effluents containing 2-chlorophenol by adsorption onto chemically and physically activated biochars. *Journal of Environmental Chemical Engineering, 8*(6), 104473. doi:https://doi.org/10.1016/j.jece.2020.104473

Maciá-Agulló, J. A., Moore, B. C., Cazorla-Amorós, D., & Linares-Solano, A. (2004). Activation of coal tar pitch carbon fibres: Physical activation vs. chemical activation. *Carbon, 42*(7), 1367-1370. doi:https://doi.org/10.1016/j.carbon.2004.01.013

Mallesh, D., Anbarasan, J., Mahesh Kumar, P., Upendar, K., Chandrashekar, P., Rao, B. V. S. K., & Lingaiah, N. (2020). Synthesis, characterization of carbon adsorbents derived from waste biomass and its application to CO2 capture. *Applied Surface Science, 530*, 147226. doi:https://doi.org/10.1016/j.apsusc.2020.147226

Maring, B. J., & Webley, P. A. (2013). A new simplified pressure/vacuum swing adsorption model for rapid adsorbent screening for CO2 capture applications. *International Journal of Greenhouse Gas Control, 15*, 16-31. doi:https://doi.org/10.1016/j.ijggc.2013.01.009

Matos, J., Nahas, C., Rojas, L., & Rosales, M. (2011). Synthesis and characterization of activated carbon from sawdust of Algarroba wood. 1. Physical activation and pyrolysis. *J Hazard Mater, 196*, 360-369. doi:10.1016/j.jhazmat.2011.09.046

Minani, J. M., Foppen, J. W., & Lens, P. N. (2014). Sorption of cadmium in columns of sand-supported hydrothermally carbonized particles. *Water Sci Technol, 69*(12), 2504-2509. doi:10.2166/wst.2014.175

Mishra, R. K., kumar, V., Kumar, P., & Mohanty, K. (2022). Hydrothermal liquefaction of biomass for bio-crude production: A review on feedstocks, chemical compositions, operating parameters, reaction kinetics, techno-economic study, and life cycle assessment. *Fuel, 316*, 123377. doi:https://doi.org/10.1016/j.fuel.2022.123377

Mohd Azmi, N. Z., Buthiyappan, A., Abdul Raman, A. A., Abdul Patah, M. F., & Sufian, S. (2022). Recent advances in biomass based activated carbon for carbon dioxide capture – A review. *Journal of Industrial and Engineering Chemistry, 116*, 1-20. doi:https://doi.org/10.1016/j.jiec.2022.08.021

Mong, G. R., Chong, C. T., Ng, J.-H., Chong, W. W. F., Lam, S. S., Ong, H. C., & Ani, F. N. (2020). Microwave pyrolysis for valorisation of horse manure biowaste. *Energy Conversion and Management, 220*, 113074. doi:https://doi.org/10.1016/j.enconman.2020.113074

Murakami, K., Watanabe, S., Kato, T., & Sugawara, K. (2013). Transition temperature control of adsorption–desorption property of PNIPAM / mesoporous silica composite by addition of crosslinking agent. *Colloids and Surfaces A: Physicochemical and Engineering Aspects, 419*, 223-227. doi:https://doi.org/10.1016/j.colsurfa.2012.11.074

Nasri, N. S., Hamza, U. D., Ismail, S. N., Ahmed, M. M., & Mohsin, R. (2014). Assessment of porous carbons derived from sustainable palm solid waste for carbon dioxide capture. *Journal of Cleaner Production, 71*, 148-157. doi:https://doi.org/10.1016/j.jclepro.2013.11.053

Nayak, A., Bhushan, B., Gupta, V., & Kotnala, S. (2021). Fabrication of microwave assisted biogenic magnetite-biochar nanocomposite: A green adsorbent from jackfruit peel for removal and recovery of nutrients in water sample. *Journal of Industrial and Engineering Chemistry, 100*, 134-148. doi:https://doi.org/10.1016/j.jiec.2021.05.028

Nelson, K. M., Mahurin, S. M., Mayes, R. T., Williamson, B., Teague, C. M., Binder, A. J., . . . Dai, S. (2016). Preparation and CO2 adsorption properties of soft-templated mesoporous carbons derived from chestnut tannin precursors. *Microporous and Mesoporous Materials, 222*, 94-103. doi:https://doi.org/10.1016/j.micromeso.2015.09.050

Nowrouzi, M., Younesi, H., & Bahramifar, N. (2017). High efficient carbon dioxide capture onto as-synthesized activated carbon by chemical activation of Persian Ironwood biomass and the economic pre-feasibility study for scale-up. *Journal of Cleaner Production, 168*, 499-509. doi:https://doi.org/10.1016/j.jclepro.2017.09.080

Nowrouzi, M., Younesi, H., & Bahramifar, N. (2018). Superior CO2 capture performance on biomass-derived carbon/metal oxides nanocomposites from Persian ironwood by H3PO4 activation. *Fuel, 223*, 99-114. doi:https://doi.org/10.1016/j.fuel.2018.03.035

Nugent, P., Belmabkhout, Y., Burd, S. D., Cairns, A. J., Luebke, R., Forrest, K., . . . Zaworotko, M. J. (2013). Porous materials with optimal adsorption thermodynamics and kinetics for CO2 separation. *Nature, 495*(7439), 80-84. doi:10.1038/nature11893

Ogungbenro, A. E., Quang, D. V., Al-Ali, K. A., Vega, L. F., & Abu-Zahra, M. R. M. (2020). Synthesis and characterization of activated carbon from biomass date seeds for carbon dioxide adsorption. *Journal of Environmental Chemical Engineering, 8*(5), 104257. doi:https://doi.org/10.1016/j.jece.2020.104257

Ormsby, R., Kastner, J. R., & Miller, J. (2012). Hemicellulose hydrolysis using solid acid catalysts generated from biochar. *Catalysis Today, 190*(1), 89-97. doi:https://doi.org/10.1016/j.cattod.2012.02.050

Otieno, A. O., Home, P. G., Raude, J. M., Murunga, S. I., Ngumba, E., Ojwang, D. O., & Tuhkanen, T. (2021). Pineapple peel biochar and lateritic soil as adsorbents for recovery of ammonium nitrogen from human urine. *Journal of Environmental Management, 293*, 112794. doi:https://doi.org/10.1016/j.jenvman.2021.112794

Pallarés, J., González-Cencerrado, A., & Arauzo, I. (2018). Production and characterization of activated carbon from barley straw by physical activation

with carbon dioxide and steam. *Biomass and Bioenergy, 115*, 64-73. doi:https://doi.org/10.1016/j.biombioe.2018.04.015

Parshetti, G. K., Chowdhury, S., & Balasubramanian, R. (2015). Biomass derived low-cost microporous adsorbents for efficient CO2 capture. *Fuel, 148*, 246-254. doi:https://doi.org/10.1016/j.fuel.2015.01.032

Peng, Y., Sun, Y., Sun, R., Zhou, Y., Tsang, D. C. W., & Chen, Q. (2019). Optimizing the synthesis of Fe/Al (Hydr)oxides-Biochars to maximize phosphate removal via response surface model. *Journal of Cleaner Production, 237*, 117770. doi:https://doi.org/10.1016/j.jclepro.2019.117770

Pierre-Louis, A.-M., Hausner, D. B., Bhandari, N., Li, W., Kim, J., Kubicki, J. D., & Strongin, D. (2013). Adsorption of carbon dioxide on Al/Fe oxyhydroxide. *Journal of Colloid and Interface Science, 400*, 1-10. doi:https://doi.org/10.1016/j.jcis.2013.01.047

Promraksa, A., & Rakmak, N. (2020). Biochar production from palm oil mill residues and application of the biochar to adsorb carbon dioxide. *Heliyon, 6*(5), e04019. doi:10.1016/j.heliyon.2020.e04019

Pu, Q., Wang, Y., Wang, X., Shao, Z., Wen, S., Wang, J., . . . Wang, Q. (2021). Biomass-derived carbon/MgO-Al2O3 composite with superior dynamic CO2 uptake for post combustion capture application. *Journal of CO2 Utilization, 54*, 101756. doi:https://doi.org/10.1016/j.jcou.2021.101756

Qin, C., Wang, H., Yuan, X., Xiong, T., Zhang, J., & Zhang, J. (2020). Understanding structure-performance correlation of biochar materials in environmental remediation and electrochemical devices. *Chemical Engineering Journal, 382*, 122977. doi:https://doi.org/10.1016/j.cej.2019.122977

Raganati, F., Miccio, F., & Ammendola, P. (2021). Adsorption of Carbon Dioxide for Post-combustion Capture: A Review. *Energy & Fuels, 35*(16), 12845-12868. doi:10.1021/acs.energyfuels.1c01618

Ranguin, R., Jean-Marius, C., Yacou, C., Gaspard, S., Feidt, C., Rychen, G., & Delannoy, M. (2020). Reduction of chlordecone environmental availability by soil amendment of biochars and activated carbons from lignocellulosic biomass. *Environ Sci Pollut Res Int, 27*(33), 41093-41104. doi:10.1007/s11356-019-07366-2

Rashidi, N. A., & Yusup, S. (2019). Production of palm kernel shell-based activated carbon by direct physical activation for carbon dioxide adsorption. *Environ Sci Pollut Res Int, 26*(33), 33732-33746. doi:10.1007/s11356-018-1903-8

Rashidi, N. A., & Yusup, S. (2020). Biochar as potential precursors for activated carbon production: parametric analysis and multi-response optimization. *Environ Sci Pollut Res Int, 27*(22), 27480-27490. doi:10.1007/s11356-019-07448-1

Rashidi, N. A., Yusup, S., Borhan, A., & Loong, L. H. (2014). Experimental and modelling studies of carbon dioxide adsorption by porous biomass derived activated carbon. *Clean Technologies and Environmental Policy, 16*(7), 1353-1361. doi:10.1007/s10098-014-0788-6

Rattanaphan, S., Rungrotmongkol, T., & Kongsune, P. (2020). Biogas improving by adsorption of CO2 on modified waste tea activated carbon. *Renewable Energy, 145*, 622-631. doi:https://doi.org/10.1016/j.renene.2019.05.104

Rehman, A. u., Baek, J. W., Rene, E. R., Sergienko, N., Behera, S. K., & Park, H.-S. (2018). Effect of process parameters influencing the chemical modification of activated carbon fiber for carbon dioxide removal. *Process Safety and Environmental Protection, 118*, 384-396. doi:https://doi.org/10.1016/j.psep.2018.07.004

Rodgers, M., Healy, M. G., & Mulqueen, J. (2005). Organic carbon removal and nitrification of high strength wastewaters using stratified sand filters. *Water Res, 39*(14), 3279-3286. doi:10.1016/j.watres.2005.05.035

Rouzitalab, Z., Maklavany, D. M., Jafarinejad, S., & Rashidi, A. (2020). Lignocellulose-based adsorbents: A spotlight review of the effective parameters on carbon dioxide capture process. *Chemosphere, 246*, 125756. doi:https://doi.org/10.1016/j.chemosphere.2019.125756

Rufford, T., Hulicova-Jurcakova, D., Zhu, Z., & Lu, M. (2010). A comparative study of chemical treatment by FeCl3, MgCl2, and ZnCl2 on microstructure, surface chemistry, and double-layercapacitance of carbons from waste biomass. *Journal of Materials Research, 25*. doi:10.1557/JMR.2010.0186

Ruhaimi, A. H., & Ab Aziz, M. A. (2021). High-performance flake-like mesoporous magnesium oxide prepared by eggshell membrane template for carbon dioxide capture. *Journal of Solid State Chemistry, 300*, 122242. doi:https://doi.org/10.1016/j.jssc.2021.122242

Ruhaimi, A. H., Aziz, M. A. A., & Jalil, A. A. (2021). Magnesium oxide-based adsorbents for carbon dioxide capture: Current progress and future opportunities. *Journal of CO2 Utilization, 43*, 101357. doi:https://doi.org/10.1016/j.jcou.2020.101357

Sabri, N. H., Rani, N. H. A., Mohamad, N. F., Mohd Muhsen, N. A. S., & Md Zaini, M. S. (2023). Simulation of CO2 capture for amine impregnated activated carbon - palm kernel shell (AC-PKS) adsorbent in pressure swing adsorption (PSA) using Aspen Adsorption. *Materials Today: Proceedings*. doi:https://doi.org/10.1016/j.matpr.2022.12.206

Sayğılı, H., Güzel, F., & Önal, Y. (2015). Conversion of grape industrial processing waste to activated carbon sorbent and its performance in cationic and anionic dyes adsorption. *Journal of Cleaner Production, 93*, 84-93. doi:https://doi.org/10.1016/j.jclepro.2015.01.009

Selimin, M. A., Latif, A. F. A., Er, Y. C., Muhamad, M. S., Basri, H., & Lee, T. C. (2021). Adsorption efficiency of banana blossom peels (musa acuminata colla) adsorbent for chromium (VI) removal. *Materials Today: Proceedings*. doi:https://doi.org/10.1016/j.matpr.2021.10.502

Serafin, J., Narkiewicz, U., Morawski, A. W., Wróbel, R. J., & Michalkiewicz, B. (2017). Highly microporous activated carbons from biomass for CO2 capture and effective micropores at different conditions. *Journal of CO2 Utilization, 18*, 73-79. doi:https://doi.org/10.1016/j.jcou.2017.01.006

Serafin, J., Ouzzine, M., Cruz Junior, O. F., & Sreńscek-Nazzal, J. (2021). Preparation of low-cost activated carbons from amazonian nutshells for CO2 storage. *Biomass and Bioenergy, 144*, 105925. doi:https://doi.org/10.1016/j.biombioe.2020.105925

Sevilla, M., & Fuertes, A. B. (2011). Sustainable porous carbons with a superior performance for CO2 capture. *Energy & Environmental Science, 4*(5), 1765-1771. doi:10.1039/C0EE00784F

Shabbani, H. J. K., Khairunnisa Shamsudin, I., Dezaini, N. N., Abd, A. A., & Othman, M. R. (2022). Effect of adsorption–desorption on hydrogen purity and recovery in non-adiabatic pressure swing mediated by microporous palm kernel shell adsorbent. *Fuel, 311*, 122550. doi:https://doi.org/10.1016/j.fuel.2021.122550

Shang, J., Pi, J., Zong, M., Wang, Y., Li, W., & Liao, Q. (2016). Chromium removal using magnetic biochar derived from herb-residue. *Journal of the Taiwan Institute of Chemical Engineers, 68*, 289-294. doi:https://doi.org/10.1016/j.jtice.2016.09.012

Shi, S., & Liu, Y. (2021). Nitrogen-doped activated carbons derived from microalgae pyrolysis by-products by microwave/KOH activation for CO2 adsorption. *Fuel, 306*, 121762. doi:https://doi.org/10.1016/j.fuel.2021.121762

Shukla, N., Sahoo, D., & Remya, N. (2019). Biochar from microwave pyrolysis of rice husk for tertiary wastewater treatment and soil nourishment. *Journal of Cleaner Production, 235*, 1073-1079. doi:https://doi.org/10.1016/j.jclepro.2019.07.042

Singh, G., Ismail, I. S., Bilen, C., Shanbhag, D., Sathish, C. I., Ramadass, K., & Vinu, A. (2019). A facile synthesis of activated porous carbon spheres from d-glucose using a non-corrosive activating agent for efficient carbon dioxide capture. *Applied Energy, 255*, 113831. doi:https://doi.org/10.1016/j.apenergy.2019.113831

Singh, G., Kim, I. Y., Lakhi, K. S., Joseph, S., Srivastava, P., Naidu, R., & Vinu, A. (2017). Heteroatom functionalized activated porous biocarbons and their excellent performance for CO2 capture at high pressure. *Journal of Materials Chemistry A, 5*(40), 21196-21204. doi:10.1039/C7TA07186H

Singh, G., Kim, I. Y., Lakhi, K. S., Srivastava, P., Naidu, R., & Vinu, A. (2017). Single step synthesis of activated bio-carbons with a high surface area and their excellent CO2 adsorption capacity. *Carbon, 116*, 448-455. doi:https://doi.org/10.1016/j.carbon.2017.02.015

Singh, G., Lakhi, K. S., Kim, I. Y., Kim, S., Srivastava, P., Naidu, R., & Vinu, A. (2017). Highly Efficient Method for the Synthesis of Activated Mesoporous Biocarbons with Extremely High Surface Area for High-Pressure CO2 Adsorption. *ACS Applied Materials & Interfaces, 9*(35), 29782-29793. doi:10.1021/acsami.7b08797

Singh, G., Lakhi, K. S., Ramadass, K., Kim, S., Stockdale, D., & Vinu, A. (2018). A combined strategy of acid-assisted polymerization and solid state activation to synthesize functionalized nanoporous activated biocarbons from biomass for CO2 capture. *Microporous and Mesoporous Materials, 271*, 23-32. doi:https://doi.org/10.1016/j.micromeso.2018.05.035

Singh, M. G., Lakhi, K. S., Park, D. H., Srivastava, P., Naidu, R., & Vinu, A. J. C. (2018). Facile One-Pot Synthesis of Activated Porous Biocarbons with a High Nitrogen Content for CO2 Capture. *4*(3), 281-290.

Siriwardane, I. W., Udangawa, R., de Silva, R. M., Kumarasinghe, A. R., Acres, R. G., Hettiarachchi, A., . . . de Silva, K. M. N. (2017). Synthesis and characterization of nano magnesium oxide impregnated granular activated carbon composite for H2S removal applications. *Materials & Design, 136*, 127-136. doi:https://doi.org/10.1016/j.matdes.2017.09.034

Somy, A., Mehrnia, M. R., Amrei, H. D., Ghanizadeh, A., & Safari, M. (2009). Adsorption of carbon dioxide using impregnated activated carbon promoted by Zinc. *International Journal of Greenhouse Gas Control, 3*(3), 249-254. doi:https://doi.org/10.1016/j.ijggc.2008.10.003

Song, G., Zhu, X., Chen, R., Liao, Q., Ding, Y.-D., & Chen, L. (2016a). An investigation of CO2 adsorption kinetics on porous magnesium oxide. *Chemical Engineering Journal, 283*, 175-183. doi:https://doi.org/10.1016/j.cej.2015.07.055

Song, G., Zhu, X., Chen, R., Liao, Q., Ding, Y., & Chen, L. (2016b). Influence of the precursor on the porous structure and CO 2 adsorption characteristics of MgO. *RSC Adv., 6*. doi:10.1039/C5RA26595A

Sreńscek-Nazzal, J., & Kiełbasa, K. (2019). Advances in modification of commercial activated carbon for enhancement of CO2 capture. *Applied Surface Science, 494*, 137-151. doi:https://doi.org/10.1016/j.apsusc.2019.07.108

Sruthi, T., Ashok, J., Monica Nissy, S., Koteshwara rao, C., & Vangalapati, M. (2019). Extraction and removal of Nickel from battery waste, using Nano sized activated carbon of Coconut shell and Tamarind seed powders in a column. *Materials Today: Proceedings, 18*, 5240-5246. doi:https://doi.org/10.1016/j.matpr.2019.07.524

Su, Y., Liu, L., Zhang, S., Xu, D., Du, H., Cheng, Y., . . . Xiong, Y. (2020). A green route for pyrolysis poly-generation of typical high ash biomass, rice husk: Effects on simultaneous production of carbonic oxide-rich syngas, phenol-abundant bio-oil, high-adsorption porous carbon and amorphous silicon dioxide. *Bioresour Technol, 295*, 122243. doi:10.1016/j.biortech.2019.122243

Sun, H., Yang, B., & Li, A. (2019). Biomass derived porous carbon for efficient capture of carbon dioxide, organic contaminants and volatile iodine with exceptionally high uptake. *Chemical Engineering Journal, 372*, 65-73. doi:https://doi.org/10.1016/j.cej.2019.04.061

Tahir, M. Y., Sillanpaa, M., Almutairi, T. M., Mohammed, A. A. A., & Ali, S. (2023). Excellent photocatalytic and antibacterial activities of bio-activated carbon decorated magnesium oxide nanoparticles. *Chemosphere, 312*, 137327. doi:https://doi.org/10.1016/j.chemosphere.2022.137327

Tan, B., Cheng, G., Zhu, X., & Yang, X. (2020). Experimental Study on the Physisorption Characteristics of O(2) in Coal Powder are Effected by Coal Nanopore Structure. *Sci Rep, 10*(1), 6946. doi:10.1038/s41598-020-63988-4

Tan, J. C., & Cheetham, A. K. (2011). Mechanical properties of hybrid inorganic–organic framework materials: establishing fundamental structure–property relationships. *Chemical Society Reviews, 40*(2), 1059-1080. doi:10.1039/C0CS00163E

Tan, Y. L., Hameed, B. H., & Abdullah, A. Z. (2020). Deoxygenation of pyrolysis vapour derived from durian shell using catalysts prepared from industrial wastes rich in Ca, Fe, Si and Al. *Science of The Total Environment, 703*, 134902. doi:https://doi.org/10.1016/j.scitotenv.2019.134902

Tuan, V. A., & Lee, C. H. (2018). Preparation of rod-like MgO by simple precipitation method for CO2 capture at ambient temperature. *Vietnam Journal of Chemistry, 56*(2), 197-202. doi:https://doi.org/10.1002/vjch.201800013

V.R.Myneni, punugoti, T., Kala, N. S., N.R.Kanidarapu, & Vangalapati, M. (2019). Modelling and Optimization of Methylene Blue Adsorption onto Magnesium Oxide Nanoparticles loaded onto Activated Carbon (MgONP-AC): Response Surface Methodology and Artificial Neural Networks. *Materials Today: Proceedings, 18*, 4932-4941. doi:https://doi.org/10.1016/j.matpr.2019.07.485

Vall, M., Hultberg, J., Strømme, M., & Cheung, O. (2019). Carbon dioxide adsorption on mesoporous magnesium carbonate. *Energy Procedia, 158*, 4671-4676. doi:https://doi.org/10.1016/j.egypro.2019.01.738

Van de Voorde, B., Stassen, I., Bueken, B., Vermoortele, F., De Vos, D., Ameloot, R., . . . Bennett, T. D. (2015). Improving the mechanical stability of zirconium-based metal–organic frameworks by incorporation of acidic modulators. *Journal of Materials Chemistry A, 3*(4), 1737-1742. doi:10.1039/C4TA06396A

Wang, B., Li, Y.-n., & Wang, L. (2019). Metal-free activation of persulfates by corn stalk biochar for the degradation of antibiotic norfloxacin: Activation factors and degradation mechanism. *Chemosphere, 237*, 124454. doi:https://doi.org/10.1016/j.chemosphere.2019.124454

Wang, F., Jin, L., Guo, C., Min, L., Zhang, P., Sun, H., . . . Zhang, C. (2021). Enhanced heavy metals sorption by modified biochars derived from pig manure. *Science of*

The Total Environment, 147595. doi:https://doi.org/10.1016/j.scitotenv.2021.147595

Wang, H., Wang, H., Liu, G., & Yan, Q. (2021). In-situ pyrolysis of Taihu blue algae biomass as appealing porous carbon adsorbent for CO2 capture: Role of the intrinsic N. *Science of The Total Environment, 771*, 145424. doi:https://doi.org/10.1016/j.scitotenv.2021.145424

Wang, Q., Luo, J., Zhong, Z., & Borgna, A. (2011). CO2 Capture by Solid-Adsorbents and Their Applications: Current Status and New Trends. *Energy & Environmental Sciences, 4*, 2011.

Wang, R.-Z., Huang, D.-L., Liu, Y.-G., Zhang, C., Lai, C., Wang, X., . . . Xu, P. (2020). Synergistic removal of copper and tetracycline from aqueous solution by steam-activated bamboo-derived biochar. *Journal of Hazardous Materials, 384*, 121470. doi:https://doi.org/10.1016/j.jhazmat.2019.121470

Wang, R., Wang, P., Yan, X., Lang, J., Peng, C., & Xue, Q. (2012). Promising Porous Carbon Derived from Celtuce Leaves with Outstanding Supercapacitance and CO2 Capture Performance. *ACS Applied Materials & Interfaces, 4*(11), 5800-5806. doi:10.1021/am302077c

Wang, R., Wang, P., Yan, X., Lang, J., Peng, C., & Xue, Q. (2012). Promising porous carbon derived from celtuce leaves with outstanding supercapacitance and CO(2) capture performance. *ACS Appl Mater Interfaces, 4*(11), 5800-5806. doi:10.1021/am302077c

Wang, Y., Jia, H., Chen, P., Fang, X., & Du, T. (2020). Synthesis of La and Ce modified X zeolite from rice husk ash for carbon dioxide capture. *Journal of Materials Research and Technology, 9*(3), 4368-4378. doi:10.1016/j.jmrt.2020.02.061

Wang, Z., Shi, M., Li, J., & Zheng, Z. (2014). Influence of moderate pre-oxidation treatment on the physical, chemical and phosphate adsorption properties of iron-containing activated carbon. *Journal of Environmental Sciences, 26*(3), 519-528. doi:https://doi.org/10.1016/S1001-0742(13)60440-4

Wei, H., Deng, S., Hu, B., Chen, Z., Wang, B., Huang, J., & Yu, G. (2012). Granular Bamboo-Derived Activated Carbon for High CO2 Adsorption: The Dominant Role of Narrow Micropores. *5*(12), 2354-2360. doi:https://doi.org/10.1002/cssc.201200570

Wibawa, P. J., Nur, M., Asy'ari, M., & Nur, H. (2020). SEM, XRD and FTIR analyses of both ultrasonic and heat generated activated carbon black microstructures. *Heliyon, 6*(3), e03546. doi:https://doi.org/10.1016/j.heliyon.2020.e03546

Wu, C., Song, M., Jin, B., Wu, Y., & Huang, Y. (2013). Effect of biomass addition on the surface and adsorption characterization of carbon-based adsorbents from sewage sludge. *J Environ Sci (China), 25*(2), 405-412. doi:10.1016/s1001-0742(12)60028-x

Wu, H., Yildirim, T., & Zhou, W. (2013). Exceptional Mechanical Stability of Highly Porous Zirconium Metal–Organic Framework UiO-66 and Its Important Implications. *The Journal of Physical Chemistry Letters, 4*(6), 925-930. doi:10.1021/jz4002345

Wu, Y., Xu, J., Mumford, K., Stevens, G. W., Fei, W., & Wang, Y. (2020). Recent advances in carbon dioxide capture and utilization with amines and ionic liquids. *Green Chemical Engineering, 1*(1), 16-32. doi:https://doi.org/10.1016/j.gce.2020.09.005

Xing, W., Liu, C., Zhou, Z., Zhang, L., Zhou, J., Zhuo, S., . . . Qiao, S. (2012). Superior CO2 uptake of N-doped activated carbon through hydrogen-bonding interaction. *Energy Environ. Sci., 5*, 7323-7327. doi:10.1039/C2EE21653A

Xu, X., Kan, Y., Zhao, L., & Cao, X. (2016). Chemical transformation of CO2 during its capture by waste biomass derived biochars. *Environ Pollut, 213*, 533-540. doi:10.1016/j.envpol.2016.03.013

Xu, X., Xu, Z., Gao, B., Zhao, L., Zheng, Y., Huang, J., . . . Cao, X. (2020). New insights into CO2 sorption on biochar/Fe oxyhydroxide composites: Kinetics, mechanisms, and in situ characterization. *Chemical Engineering Journal, 384*. doi:10.1016/j.cej.2019.123289

Yadavalli, G., Lei, H., Wei, Y., Zhu, L., Zhang, X., Liu, Y., & Yan, D. (2017). Carbon dioxide capture using ammonium sulfate surface modified activated biomass carbon. *Biomass and Bioenergy, 98*, 53-60. doi:https://doi.org/10.1016/j.biombioe.2017.01.015

Yan, X., Zhai, Z., Xu, J., Song, Z., Shang, S., & Rao, X. (2018). CO2-Responsive Pickering Emulsions Stabilized by a Bio-based Rigid Surfactant with Nanosilica. *J Agric Food Chem, 66*(41), 10769-10776. doi:10.1021/acs.jafc.8b03458

Yang, F., Zhang, S., Cho, D.-W., Du, Q., Song, J., & Tsang, D. C. W. (2019). Porous biochar composite assembled with ternary needle-like iron-manganese-sulphur hybrids for high-efficiency lead removal. *Bioresource Technology, 272*, 415-420. doi:https://doi.org/10.1016/j.biortech.2018.10.068

Yang, F., Zhang, S., Sun, Y., Cheng, K., Li, J., & Tsang, D. C. W. (2018). Fabrication and characterization of hydrophilic corn stalk biochar-supported nanoscale zero-valent iron composites for efficient metal removal. *Bioresource Technology, 265*, 490-497. doi:https://doi.org/10.1016/j.biortech.2018.06.029

Yao, Q., Borjihan, Q., Qu, H., Guo, Y., Zhao, Z., Qiao, L., . . . Liu, Y. (2021). Cow dung-derived biochars engineered as antibacterial agents for bacterial decontamination. *Journal of Environmental Sciences, 105*, 33-43. doi:https://doi.org/10.1016/j.jes.2020.12.022

Yao, Y., Gao, B., Chen, J., Zhang, M., Inyang, M., Li, Y., . . . Yang, L. (2013). Engineered carbon (biochar) prepared by direct pyrolysis of Mg-accumulated tomato tissues: Characterization and phosphate removal potential. *Bioresource Technology, 138*, 8-13. doi:https://doi.org/10.1016/j.biortech.2013.03.057

Yargicoglu, E. N., Sadasivam, B. Y., Reddy, K. R., & Spokas, K. (2015). Physical and chemical characterization of waste wood derived biochars. *Waste Management, 36*, 256-268. doi:https://doi.org/10.1016/j.wasman.2014.10.029

Yek, P. N. Y., Peng, W., Wong, C. C., Liew, R. K., Ho, Y. L., Wan Mahari, W. A., . . . Lam, S. S. (2020). Engineered biochar via microwave CO2 and steam pyrolysis to treat carcinogenic Congo red dye. *J Hazard Mater, 395*, 122636. doi:10.1016/j.jhazmat.2020.122636

Yin, Z., Zhu, L., Mo, F., Li, S., Hu, D., Chu, R., . . . Hu, C. (2021). Preparation of biochar grafted with amino-riched dendrimer by carbonization, magnetization and functional modification for enhanced copper removal. *Journal of the Taiwan Institute of Chemical Engineers, 121*, 349-359. doi:https://doi.org/10.1016/j.jtice.2021.04.014

Younas, M., Rezakazemi, M., Daud, M., Wazir, M. B., Ahmad, S., Ullah, N., . . . Ramakrishna, S. (2020). Recent progress and remaining challenges in post-combustion CO2 capture using metal-organic frameworks (MOFs). *Progress in Energy and Combustion Science, 80*, 100849. doi:https://doi.org/10.1016/j.pecs.2020.100849

Yuan, X., Suvarna, M., Low, S., Dissanayake, P. D., Lee, K. B., Li, J., . . . Ok, Y. S. (2021). Applied Machine Learning for Prediction of CO2 Adsorption on

Biomass Waste-Derived Porous Carbons. *Environ Sci Technol, 55*(17), 11925-11936. doi:10.1021/acs.est.1c01849

Yunus, Z. M., Al-Gheethi, A., Othman, N., Hamdan, R., & Ruslan, N. N. (2020). Removal of heavy metals from mining effluents in tile and electroplating industries using honeydew peel activated carbon: A microstructure and techno-economic analysis. *Journal of Cleaner Production, 251*, 119738. doi:https://doi.org/10.1016/j.jclepro.2019.119738

Yusof, S. M., Othaman, R., Setiabudi, H. D., & Teh, L. P. (2021). Modified fibrous silica for enhanced carbon dioxide adsorption: Role of metal oxides on physicochemical properties and adsorption performance. *Journal of Solid State Chemistry, 294*, 121845. doi:https://doi.org/10.1016/j.jssc.2020.121845

Zabaniotou, A., Stavropoulos, G., & Skoulou, V. (2008). Activated carbon from olive kernels in a two-stage process: industrial improvement. *Bioresour Technol, 99*(2), 320-326. doi:10.1016/j.biortech.2006.12.020

Zaini, M. S. M., Arshad, M., & Syed-Hassan, S. S. A. (2023). Adsorption Isotherm and Kinetic Study of Methane on Palm Kernel Shell-Derived Activated Carbon. *Journal of Bioresources and Bioproducts, 8*(1), 66-77. doi:https://doi.org/10.1016/j.jobab.2022.11.002

Zamboni, I., Debal, M., Matt, M., Girods, P., Kiennemann, A., Rogaume, Y., & Courson, C. (2016). Catalytic gasification of biomass (Miscanthus) enhanced by CO2 sorption. *Environ Sci Pollut Res Int, 23*(22), 22253-22266. doi:10.1007/s11356-016-6444-4

Zhang, C., Geng, Z., Cai, M., Zhang, J., Liu, X., Xin, H., & Ma, J. (2013). Microstructure regulation of super activated carbon from biomass source corncob with enhanced hydrogen uptake. *International Journal of Hydrogen Energy, 38*(22), 9243-9250. doi:https://doi.org/10.1016/j.ijhydene.2013.04.163

Zhang, X., Elsayed, I., Song, X., Shmulsky, R., & Hassan, E. B. (2020). Microporous carbon nanoflakes derived from biomass cork waste for CO2 capture. *Science of The Total Environment, 748*, 142465. doi:https://doi.org/10.1016/j.scitotenv.2020.142465

Zhao, L., Bacsik, Z., Hedin, N., Wei, W., Sun, Y., Antonietti, M., & Titirici, M. M. (2010). Carbon dioxide capture on amine-rich carbonaceous materials derived from glucose. *ChemSusChem, 3*(7), 840-845. doi:10.1002/cssc.201000044

Zhao, Y., Dong, Y., Guo, Y., Huo, F., Yan, F., & He, H. (2021). Recent progress of green sorbents-based technologies for low concentration CO2 capture. *Chinese Journal of Chemical Engineering, 31*, 113-125. doi:https://doi.org/10.1016/j.cjche.2020.11.005

Zhao, Z., Nie, T., & Zhou, W. (2019). Enhanced biochar stabilities and adsorption properties for tetracycline by synthesizing silica-composited biochar. *Environ Pollut, 254*(Pt A), 113015. doi:10.1016/j.envpol.2019.113015

Zheng, N.-Y., Lee, M., Lin, Y.-L., & Samannan, B. (2020). Microwave-assisted wet co-torrefaction of food sludge and lignocellulose biowaste for biochar production and nutrient recovery. *Process Safety and Environmental Protection, 144*, 273-283. doi:https://doi.org/10.1016/j.psep.2020.07.032

Zhu, B., Shang, C., & Guo, Z. (2016). Naturally Nitrogen and Calcium-Doped Nanoporous Carbon from Pine Cone with Superior CO2 Capture Capacities. *ACS Sustainable Chemistry & Engineering, 4*(3), 1050-1057. doi:10.1021/acssuschemeng.5b01113

Zhu, S., Zhao, B., Zhang, H., & Su, Y. (2023). Biomass-based adsorbents for post-combustion CO2 capture: Preparation, performances, modeling, and assessment.

Journal of Environmental Management, 328, 117020. doi:https://doi.org/10.1016/j.jenvman.2022.117020

Zong, Y., Xiao, Q., Malik, Z., Su, Y., Wang, Y., & Lu, S. (2021). Crop straw-derived biochar alleviated cadmium and copper phytotoxicity by reducing bioavailability and accumulation in a field experiment of rice-rape-corn rotation system. *Chemosphere, 280*, 130830. doi:https://doi.org/10.1016/j.chemosphere.2021.130830